

THESIS FOR THE DEGREE OF DOCTOR OF PHILOSOPHY

Nanostructured Model Electrodes for Studies of Fuel Cell Reactions

Björn Wickman



CHALMERS

Department of Applied Physics
CHALMERS UNIVERSITY OF TECHNOLOGY
Göteborg, Sweden 2010

Nanostructured Model Electrodes for Studies of Fuel Cell Reactions
Björn Wickman
ISBN 978-91-7385-437-5

© BJÖRN WICKMAN, 2010

Doktorsavhandlingar vid Chalmers tekniska högskola
Ny serie nr 3118
ISSN 0346-718X

Department of Applied Physics
Chalmers University of Technology
SE-412 96 Göteborg
Sweden
Telephone + 46 (0)31-772 1000

Cover: SEM images of evaporated Pt on a gas diffusion layer (left) and Pt nanodisks prepared by hole-mask colloidal lithography on a Au support (right). The blue and red curves are cyclic voltammetry responses for the evaporated and nanostructured Pt, respectively. To the left, the larger darker structures are the carbon support and the smaller brighter spots are Pt nanoparticles of 3–5 nm in diameter. The Pt nanodisks to the right have a diameter of about 190 nm.

Chalmers Reproservice
Göteborg, Sweden 2010

Nanostructured Model Electrodes for Studies of Fuel Cell Reactions
BJÖRN WICKMAN
Department of Applied Physics
Chalmers University of Technology

Abstract

There is currently a general need for alternative and sustainable energy systems. As part of such a system, the polymer electrolyte fuel cell (PEMFC) offers efficient and emission free energy conversion. Although fuel cells have advantages over conventional technologies, several factors are currently preventing a large scale practical and commercial break through. At a system level, the hurdles are connected with high cost and limited life-time. For the system components, a major part of the problems is related to the electrodes. PEMFC electrodes are porous structures that consist of nanometer sized platinum particles supported on carbon structures, which are mixed with an ionomer. In order to optimize the fuel cell performance, it is essential to understand the processes that occur on the electrode surfaces. The structural complexity of real electrodes renders, however, fundamental studies of their function difficult. One possibility to overcome this issue is to use well-defined nanostructured model electrodes.

In this thesis, a series of different model systems have been designed, fabricated, characterized, and evaluated. The model electrodes range from two dimensional structures, manufactured by lithography techniques, to more realistic systems prepared on conventional fuel cell materials. Several new methods for the preparation of controlled model electrodes were developed and demonstrated. The performance of these nanofabricated catalysts were evaluated in half-cell setups or in single cell fuel cells. The different model systems enable specific and selected aspects of the real system to be analyzed. Questions that were addressed include reduction and optimization of platinum use, mechanistic investigations of specific reactions, and electrode degradation.

Single cell fuel cell experiments were employed to characterize the activity and stability of platinum upon introduction of a second material. With the use of model electrodes it was possible to determine the mechanism and kinetic parameters for the hydrogen oxidation reaction, which have been difficult to deduce with traditional methods. Arrays of platinum nanodisks measured in half-cell were used to illustrate and characterize the importance of mass transport and reactant intermediates for several fuel cell relevant reactions. It was, for example, proven that the oxygen reduction reaction proceeds via a serial pathway with hydrogen peroxide as an intermediate species. Electrode degradation was analyzed with thin-film model electrodes using electrochemical quartz crystal microbalance. This methodology enabled direct measurements of mass changes caused by platinum dissolution and platinum catalyzed carbon oxidation.

Keywords: Fuel Cell, PEMFC, Model System, Electrode, Catalyst, Oxygen Reduction, Hydrogen Oxidation, Degradation, Nanofabrication

List of Appended Papers

This thesis is based on the work presented in the following papers

- I. **Nanometer-thick Films of Titanium Oxide Acting as Electrolyte in the Polymer Electrolyte Fuel Cell**
Henrik Ekström, Björn Wickman, Marie Gustavsson, Per Hanarp, Lisa Eurenus, Eva Olsson, Göran Lindbergh
Electrochimica Acta **52**, (2007) 4239-4245
- II. **Transport Effects in the Oxygen Reduction Reaction on Nanostructured, Planar Glassy Carbon Supported Pt/GC Model Electrodes**
Anja Schneider, Luis Colmenares, Yvonne E. Seidel, Zenonas Jusys, Björn Wickman, Bengt Kasemo, R. Jürgen Behm
Physical Chemistry Chemical Physics **10**, (2008) 1931-1943
- III. **Electrochemical Performance and Stability of Thin Film Electrodes with Metal Oxides in Polymer Electrolyte Fuel Cells**
Maria Wesselmark, Björn Wickman, Carina Lagergren, Göran Lindbergh
Electrochimica Acta, *In Press Corrected Proof*
- IV. **Corrosion Induced Degradation of Pt/C Model Electrodes Measured with Electrochemical Quartz Crystal Microbalance**
Björn Wickman, Henrik Grönbeck, Per Hanarp, Bengt Kasemo
Journal of The Electrochemical Society **157**, (2010) B592-B598
- V. **Hydrogen Oxidation Reaction on Thin Platinum Electrodes in the Polymer Electrolyte Fuel Cell**
Maria Wesselmark, Björn Wickman, Carina Lagergren, Göran Lindbergh
Electrochemistry Communications, *Accepted for Publication*
- VI. **Fabrication of Poly and Single Crystalline Platinum Nanostructures Using Hole-Mask Colloidal Lithography, Electrodeposition, Evaporation, and Annealing**
Björn Wickman, Hans Fredriksson, Stefan Gustafsson, Eva Olsson, Bengt Kasemo
Submitted
- VII. **Fabrication of Pt/Ru Nanoparticle Pair Arrays With Controlled Separation and their Electrocatalytic Properties**
Björn Wickman, Yvonne E. Seidel, Zenonas Jusys, Bengt Kasemo, R. Jürgen Behm
Submitted
- VIII. **On The Role of Tungsten Oxide in Polymer Electrolyte Fuel Cell Electrodes — A Thin-Film Model Electrode Study**
Björn Wickman, Maria Wesselmark, Carina Lagergren, Göran Lindbergh
Manuscript

Related papers not included in this thesis

- IX. Mesoscopic Mass Transport Effects in Electrocatalytic Processes**
Yvonne E. Seidel, Anja Schneider, Zenonas Jusys, Björn Wickman, Bengt Kasemo, R. Jürgen Behm
Faraday Discussions **140**, (2008) 167-184
- X. Nanostructured, Glassy-Carbon-Supported Pt/GC Electrodes: The Presence of Secondary Pt Nanostructures and How to Avoid Them**
Yvonne E. Seidel, Matthias Müller, Zenonas Jusys, Björn Wickman, Per Hanarp, Bengt Kasemo, Ute Hörmann, Ute Kaiser, R. Jürgen Behm
Journal of The Electrochemical Society **155**, (2008) K171-K179
- XI. Electrocatalysis and Transport Effects on Nanostructured Pt/GC Electrodes**
Rakel W. Lindström, Yvonne E. Seidel, Zenonas Jusys, Marie Gustavsson, Björn Wickman, Bengt Kasemo, R. Jürgen Behm
Journal of Electroanalytical Chemistry **644**, (2010) 90-102
- XII. Transport Effects in the Electrooxidation of Methanol Studied on Nanostructured Pt/Glassy Carbon Electrodes**
Yvonne E. Seidel, Anja Schneider, Zenonas Jusys, Björn Wickman, Bengt Kasemo, R. Jürgen Behm
Langmuir **26**, (2010) 3569-3578
- XIII. Mesoscopic Transport Effects in Electrocatalytic Reactions**
Yvonne E. Seidel, Zenonas Jusys, Björn Wickman, Bengt Kasemo, R. Jürgen Behm
ECS Transactions **25**, (2010) 91-102
- XIV. Mass Transport Effects in CO Adsorption and Continuous Oxidation Over Regular Arrays of Pt Nanostructures on Planar Glassy Carbon Supports**
Halina Schwechten, Martin Heinen, Yvonne E. Seidel, Zenonas Jusys, Björn Wickman, Bengt Kasemo, R. Jürgen Behm
Submitted

My contributions to the appended papers

- I.** Prepared a majority of the samples and performed most of the physical characterization. Participated in the electrochemical measurements and interpretation. Contributed to the writing.
- II.** Prepared all samples and performed parts of the physical characterization. Contributed to the writing.
- III.** Prepared all samples and performed the physical characterization. Participated in the planning and interpretation. Contributed to the writing.
- IV.** Prepared all samples and performed most of the physical characterization. Performed the electrochemical measurements. Participated in the planning and interpretation. Wrote the first draft of the paper.
- V.** Prepared all samples and performed the physical characterization. Participated in the interpretation. Contributed to the writing.
- VI.** Prepared the majority of the samples and performed the physical characterization. Participated in the planning and interpretation. Wrote the first draft of the paper.
- VII.** Prepared all samples and performed the physical characterization. Participated in the planning, electrochemical measurements, and interpretation. Wrote the first draft of the paper.
- VIII.** Prepared all samples and performed the physical characterization. Participated in the planning and interpretation. Wrote the first draft of the paper.

Table of Contents

Abstract	iii
List of Appended Papers	iv
1 Introduction	1
1.1 Fuel Cells in Energy Systems	2
1.2 Fuel Cells Studied by Model Systems	3
1.3 This Thesis	5
2 Fuel Cells	7
2.1 History	7
2.2 Principle	7
2.3 Fuel Cell Types	8
2.4 The Polymer Electrolyte Fuel Cell	10
2.4.1 Fundamentals and Components	10
2.5 Electrocatalysis	13
2.5.1 Electrochemistry	14
2.5.2 Heterogeneous Catalysis	15
2.5.3 Fuel Cell Electrocatalysis	16
2.6 PEMFC Performance	17
2.6.1 Thermodynamics	17
2.6.2 Kinetics	18
2.6.3 Transport	20
2.6.4 Losses	21
2.6.5 Efficiency	22
2.6.6 Stability	22
2.7 Present PEMFC Research	23
2.7.1 Fundamental Electrocatalytic Reactions	23
2.7.2 Electrode Structure	26
2.7.3 Electrode Degradation	27
3 Model Systems for PEM Fuel Cell Electrodes	29
3.1 Nanofabrication of Model Electrodes	29
3.2 Electrochemical Measurement Systems	32

3.2.1	Liquid Half-Cell	32
3.2.2	Single Cell Fuel Cell	33
3.3	Electrochemical Measurement Techniques	34
3.4	Physical Characterization	35
3.4.1	Microscopy	35
3.4.2	Spectroscopy	36
4	Model Electrode Fabrication and Physical Characterization	37
4.1	Thin-Film Catalysts	37
4.1.1	Thin-Film Catalysts on Nafion	37
4.1.2	Thin-Film Catalysts on GDL	39
4.1.3	Evaporated Carbon	41
4.1.4	Metal Oxides	43
4.2	Nanostructured Electrodes	44
4.2.1	Colloidal Lithography	44
4.2.2	Hole-Mask Colloidal Lithography	46
4.2.3	Modified HCL	47
4.2.4	Annealing of Pt Nanostructures	49
5	PEM Fuel Cell Reactions	51
5.1	Electrochemical Measurement Setups	51
5.1.1	Liquid Half-Cells	51
5.1.2	Single Cell Fuel Cell	53
5.2	Fundamental Electrochemical Reactions	53
5.2.1	Oxygen Reduction Reaction	54
5.2.2	Hydrogen Oxidation Reaction	56
5.2.3	Carbon Monoxide Oxidation	58
5.2.4	Proton Conduction	59
5.3	Degradation	60
5.3.1	Pt Dissolution	60
5.3.2	Carbon Corrosion	62
6	Summary of Appended Papers	63
7	Conclusions and Outlook	69
	Acknowledgements	71
	Bibliography	73

Introduction

The energy systems that our society depends on will face large changes during the upcoming decades. The present system is mainly based on non-renewable fossil fuels which are converted to useful forms of energies, such as electricity or motion, by combustion in large-scale power plants or engines. As the population of the world, as well as the global living standard increase, the energy demand will continue to grow. It has been predicted that the total energy consumption will be doubled by 2050 unless substantial changes in energy use is implemented [1, 2]. In order for the developing countries to reach the same standards of living as the western world, the energy production has to increase and the use has to become more efficient and distributed.

Fossil fuels, such as oil, coal and natural gas presently constitute the major energy sources and although there are uncertainties regarding how much of these fuels that are available and at what rate they can be harnessed, it is clear that we will not be able to rely on these energy sources to the same extent in the future. In addition to being finite resources, the production is localized and the combustion leads to emissions of harmful substances, such as nitrous oxides (NO_x), sulfur oxides (SO_x), hydrocarbons (HC) and particulate matter (PM). Moreover, the use of fossil fuels leads to emissions of carbon dioxide (CO_2) that increases the atmospheric concentration of CO_2 , which is identified as the main reason for global warming [3].

In order to meet the growing demand of energy, new types of energy systems have to be employed. Most of the present losses in efficiency are associated with the energy conversion step (i.e. going from stored energy to useful energy). A general drawback of energy converters that employ combustion is that they cannot exceed the Carnot efficiency limit. The theoretical efficiency of a typical internal combustion engine powered automobile is around 50 %, however, in practice it rarely exceeds 30 % [4]. Thus, 70 % of the fuel energy is lost. Another common energy converter, which has applications in a sustainable energy system, is the battery. The battery has a much higher efficiency than the combustion engine, but has physical limitations in the amount of energy that is possible to store. The relatively low energy density becomes a problem when weight and volume are important issues, as in transport applications. A third alternative for energy conversion is fuel cells, which constitute the underlying theme of this thesis. As will be shown, fuel

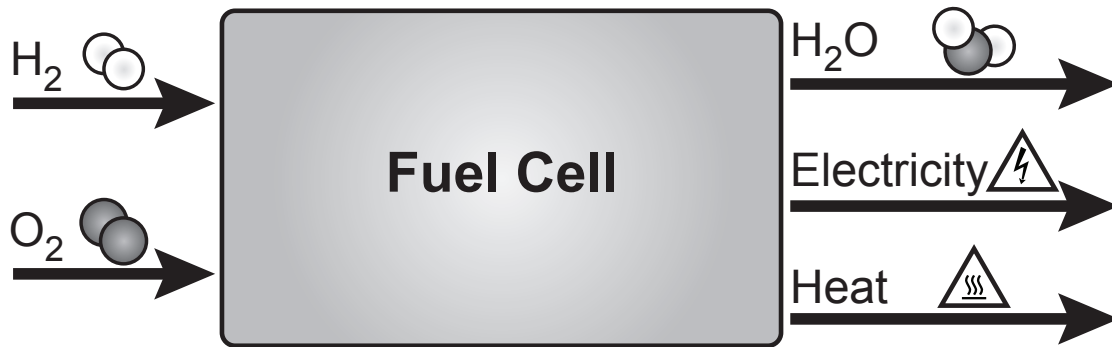


Figure 1.1: The general concept of the $\text{H}_2\text{--O}_2$ fuel cell.

cells present several advantages over conventional technology and have the potential to influence new energy systems.

Fuel cells are, moreover, advantageous with respect to sustainability. In a sustainable energy system, the energy source is renewable and the processes involved should not release any harmful substances or in other ways interfere with the environment. Furthermore, it is preferable if the energy production is performed at low cost and is not dependent on local resources. These points may favor the implementation of fuel cells.

1.1 Fuel Cells in Energy Systems

Fuel cell technology is a promising technique to convert chemical energy into electricity with potential to aid several of the problems associated with present energy converters. Figure 1.1 schematically illustrates the fuel cell concept for the simplest fuel cell, the hydrogen (H_2) – oxygen (O_2) fuel cell. H_2 and O_2 are fed to the system where they are converted to water (H_2O) in a process that produces electricity and heat. In a fuel cell, electricity is generated directly from the chemical reactions, which means that the efficiency is not restricted by the Carnot limit. The theoretical efficiency is usually above 80 % and, thus, even with conventional fuels, it is possible to decrease the overall energy consumption. As there is no combustion occurring in the fuel cell, there is no production of harmful substances such as SO_x , NO_x or PM during operation. A fuel cell can be regarded as a mixture of a combustion engine and a battery, utilizing the advantages of both while circumventing most of the disadvantages. The fuel of choice in most fuel cells is H_2 , which, in principle, can be generated from water — the most abundant chemical compound on the planet. H_2 is in this case an energy carrier whereas the primary energy source is used to split water. If the primary energy comes from renewable sources, such as wind or solar power, the energy system is truly sustainable with net zero emissions.

Fuel cells of different types are considered for a wide range of applications, from mobile phones to power plants. Most of the technologies have good scaling possibilities, which enable coverage of a large power range. However, the different fuel

cell types have large intrinsic differences in operating conditions, fuel requirements and surrounding equipment. For automotive and portable applications, the most viable fuel cell option is the polymer electrolyte membrane fuel cell (PEMFC). It typically uses H_2 as fuel and O_2 from the atmosphere. The PEMFC can be used in products with power consumption below 1 W as well as in applications requiring up to 1 MW. As one fuel cell can be made thin, several cells can be stacked close together to achieve power densities comparable to combustion engines [5].

The PEMFC was invented in the 1960s and the technology is continuously improving. During the past two decades, research and development has put the PEMFC on the verge of large-scale commercialization. Today, there are systems available for applications such as back-up power, portable electronics, and demonstration fleets of cars and busses. The current use of fuel cells is, however, still limited to niche markets and low volumes. Before PEMFCs can truly make an impact on alternative energy systems there are several issues that have to be resolved. These are mainly concerned with improving the life-time and reliability together with reducing the cost associated with fabrication and operation. For fuel cell powered light transport vehicles, the U.S. department of energy (DOE) has identified key targets for 2015 of: \$30 per kW, more than 5000 hours of operation, and practical efficiency above 60 % [6]. In order to meet these targets and to allow for further improvement, it is vital to increase the understanding of the often complex processes in the fuel cell. The objective is that increased understanding will enable new, improved fuel cells, which could become the preferred choice for energy conversion in a variety of applications. Many of the issues that prevent a large breakthrough for fuel cell technology are related to the PEMFC electrodes. The electrodes are typically loaded with the precious metal platinum (Pt) to catalyze the reactions. However, the reaction kinetics are still limiting the performance. As Pt is a scarce resource, the high price might become a hinder for large-scale commercialization [7]. It would be beneficial if the amount of Pt could be reduced, or if Pt could be replaced by cheaper and more abundant materials. Furthermore, both the Pt catalyst and the carbon support material are subjected to different types of degradation that results from the harsh environment in the fuel cell and the varying operating conditions. In order to solve these problems, systematic studies of the electrode processes and the influence of new materials and structures are desirable. A viable route for this is to use model systems.

1.2 Fuel Cells Studied by Model Systems

The term model system is a wide concept. A model system is a modified, often structurally simplified and well-defined system with which it is possible to isolate phenomena which are important for the real system. If parameters such as amount of materials, composition, structure, pressure, temperature, and rates of reactants can be controlled while the processes occurring can be quantified, then a model system can provide new and valuable information. This can in turn enable a deeper understanding of fundamental phenomena and be used to improve and optimize the

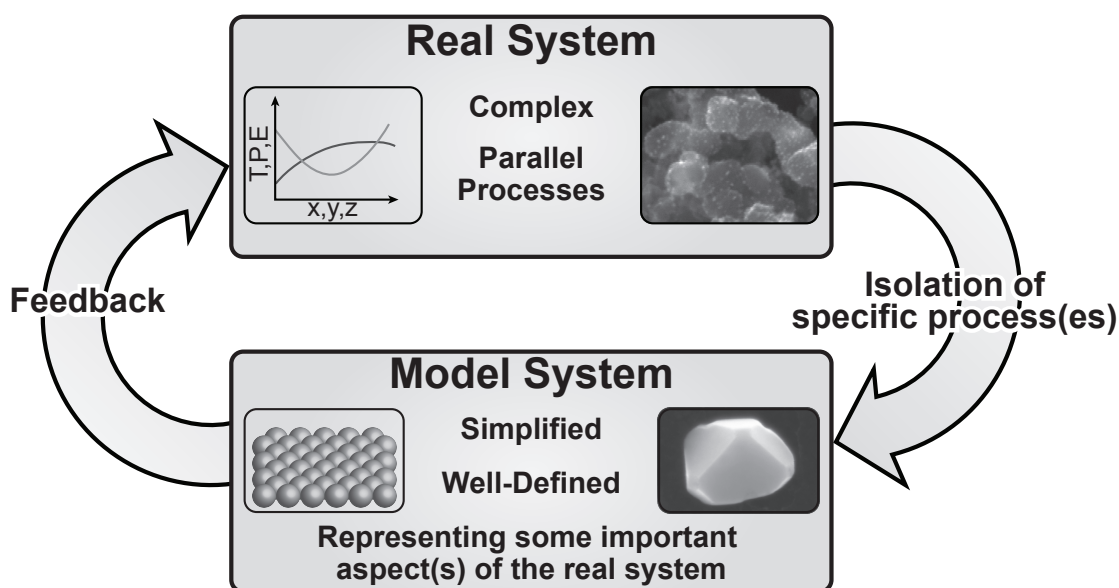


Figure 1.2: The basic structure of the model system approach.

practical system in a systematic way. This methodology is opposed to a “trial and error” approach. The basic working scheme with model systems is schematically illustrated in figure 1.2.

Single crystal studies are examples of traditional model systems that have been employed within heterogeneous catalysis to unravel surface reactions. These are often evaluated at ultra high vacuum (UHV) conditions and although they have contributed substantially to the understanding of elemental mechanisms and development of new and improved catalysts, it has been demonstrated that a straight forward extrapolation to the real systems is usually non-trivial. This is often referred to as the pressure and structure (or materials) gaps [8]. With the development of powerful analytical techniques for operation at elevated pressures, combination of UHV and higher pressure systems, and advances in the field of nanotechnology (fabrication and characterization of model systems), these gaps are now being bridged. Nevertheless, the gaps exemplify that model systems are different from the real systems and processes important for the real application might be lost or changed and new phenomena might be introduced. Consequently, it is important to have feedback between the model and the real system. One advantage with model systems is that they can be used at different levels of complexity and simplification, ranging from UHV experiments on well-defined surfaces to measurements at high pressures and with more realistic catalyst structures.

For fuel cells, model systems that comprise a simplified electrode may be referred to as a model electrode. Usually, model electrodes are evaluated in setups that are fundamentally different from real fuel cells, although they may be fuel cell like. These measurements can be called model experiments. A model system includes either or both a model electrode and a model experiment. There is a large number of electrochemical model systems available for fuel cell studies. The

most frequently used model electrodes are single crystals, extended flat films and other types of simplified surfaces, often measured in liquid half-cells, to study fundamental electrochemical reactions. However, there is a gap in structure and/or materials from these traditional model systems to real fuel cells. The advances in nanotechnology that enable fabrication of more complex structures are now bridging also these gaps.

1.3 This Thesis

In this thesis, the tools of nanotechnology have been used to fabricate model electrodes. The electrodes have been utilized to study fuel cell related phenomena with the aim to increase the understanding and improve fuel cells. A major part of the work has been devoted to development and fabrication of new types of model systems that give the possibility to explore phenomena that are difficult to study with standard techniques. The model systems span a large structural interval and can be used to bridge the structure and materials gap in electrochemistry. Another part of the work has been focused on using the model electrodes to study fundamental processes, which can lead to both increased life-time and more efficient catalysts. Two experimental setups to measure model or standard electrodes have been constructed at Chalmers, while most of the electrochemical measurements have been carried out, through collaboration, at the Royal Institute of Technology (KTH) in Stockholm and University of Ulm in Germany.

Fuel Cells

2.1 History

The discovery of the principle for fuel cells is attributed to the English physicist Sir William Grove in 1839^a [10]. In Grove's setup, two glass tubes, one filled with H₂ and the other with O₂, were placed in a beaker with acid electrolyte. In each tube there was a Pt electrode in contact with both the gas and the electrolyte and Grove was able to show a current flowing between the electrodes upon connection to a galvanometer. Over 24 hours, the reaction had consumed a substantial part of the H₂ and O₂. A few years later, Grove revisited his discovery and connected 50 pairs of tubes in series to what he called "a gaseous voltaic battery" [11]. The setup was able to generate a potential high enough to split water into O₂ and H₂, or produce a shock "which when taken by a single person was painful" [11].

Obviously, Grove's discovery was able to generate electricity, but it took more than one hundred years before any attempts were made to use fuel cells in applications. Around 1950, the first larger fuel cells, able to generate powers in the kW range was developed and starting in the early 1960s, NASA used fuel cells in their space programs for electricity and water production [9, 12]. In the years around 1970, the first fuel cell propelled cars were demonstrated.

2.2 Principle

In ordinary combustion, the molecules of the fuel collide with the molecules of the oxidant and react. The reaction takes place in fractions of ps and involves breaking of bonds in the fuel and formation of bonds between the fuel and the oxidant by redistribution of electronic charge. The simplest example is burning of hydrogen

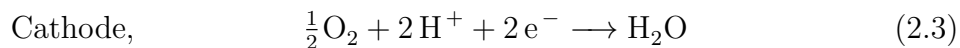


As the reaction occurs, H–H and O–O bonds are broken, whereas H–O bonds are formed. The enthalpy of the product is lower than the combined enthalpy of the

^aIt has been suggested that the German–Swiss chemist Christian F. Schönbein independently made a similar finding about the same time [9].

reactants, thus, the reaction is exothermic. In combustion, this energy difference is released as heat. The heat can subsequently be converted into mechanical energy, which in turn can be used for propulsion, or be further converted into electric energy.

The principle of the fuel cell is quite different. Here, the electrons are harnessed as they move from the reductant (fuel) and are utilized to perform work before they react with the oxidant and form the product [12–14]. Thus, electricity is generated directly from the chemical reaction. To realize this in practice, the reactants must be spatially separated and the electrons must be guided through an external circuit. An electron traveling in a circuit is equivalent to an electric current, or electricity. A key element for achieving the spatial separation is the electrolyte, a material that allows ion but not electron conduction. On both sides of the electrolyte there has to be electrodes in direct contact with the electrolyte and connected through a circuit. The electrodes will collect electrons from the fuel on one side (anode) and distribute them to the oxidant on the other side (cathode). Thus, the oxidation of the fuel is split into two electrochemical half-cell reactions. For burning of H_2



The anode and cathode reactions are termed hydrogen oxidation reaction (HOR) and oxygen reduction reaction (ORR), respectively. The overall reaction is still the same as in the ordinary combustion case (reaction 2.1), but the spatial separation allows the fuel cell to generate electricity directly from the chemical reaction. The reversed reactions, hydrogen evolution reaction (HER) and oxygen evolution reaction (OER) can be utilized to generate H_2 (and O_2).

2.3 Fuel Cell Types

The simple H_2 – O_2 fuel cell uses gaseous H_2 as fuel and protons as charge carriers (i.e. protons diffuse through the electrolyte). This is the principle used in the polymer electrolyte membrane fuel cell (PEMFC), which is the specific fuel cell type elaborated on in this thesis (although the basic approach is quite generic). There are a number of other fuel cell types categorized and termed, mainly, according to the electrolyte used. Table 2.1 presents the most common types of fuel cells with typical applications and their main advantages and weaknesses [13–15]. There are several fuel cell types that are not mentioned in table 2.1 as well as other names and classifications used. They can be termed, for example, after the fuel, the operating condition, or the charge carrier employed.

The high temperature fuel cells (to which the molten carbonate fuel cell (MCFC) and the solid oxide fuel cell (SOFC) belongs) are mainly considered for use in stationary power units where it is possible to utilize the high quality waste heat together with the produced electricity in a combined heat and power (CHP) system.

Table 2.1: Key parameters for selected fuel cell types [13–15].

Fuel cell type	PEMFC	PAFC	AFC	MCFC	SOFC
Electrolyte	Solid polymer	H ₃ PO ₄ (aq)	KOH (aq)	Molten carbonate	Ceramic
Charge carrier	H ⁺	H ⁺	OH ⁻	CO ₃ ²⁻	O ²⁻
Fuel	H ₂ , CH ₃ OH	H ₂	H ₂	H ₂ , CH ₄	H ₂ , CH ₄ , CO
Operating temperature (°C)	20–220 [†]	170–220	60–220	600–1000	600–1000
Power range (W)	10 ⁻¹ –10 ⁶	10 ³ –10 ⁶	10 ² –10 ⁴	10 ⁵ –10 ⁷	10 ³ –10 ⁷
Catalyst	Pt	Pt	Pt	Ni	Ni
Advantages	High power density, short startup times, low temperature	Low cost electrolyte, reliable, long time performance	Low cost materials, high performance	High efficiency, fuel flexibility, high quality waste heat	High efficiency, fuel flexibility, high quality waste heat
Weaknesses	Expensive catalyst, sensitive to poisoning, water management	Expensive catalyst, corrosive electrolyte, electrolyte management	Expensive catalyst, sensitive to poisoning, water management	Expensive materials, corrosive electrolyte, degradation	Expensive materials, degradation
Applications	Electrical equipment, portable devices, transportation	Electrical equipment, transportation, stationary	Space, military	Stationary	Stationary, transportation

[†]Standard perfluorosulfonic acid (PFSA) type membranes requires liquid water in order to possess sufficient proton conduction and system based on these have a maximum operating temperature of 100 °C (or slightly higher if the system is pressurized). The value of 220 °C refers to H₃PO₄ doped polybenzimidazole (PBI) type membranes that do not require liquid water (can be seen as a mixture of PAFC and PEMFC).

At high temperatures, high reaction rates can be achieved without the use of expensive catalysts and the system is less sensitive to poisoning and can operate with a large variety of fuels. However, the high temperature increases the demands on the materials in the system and requires long startup times (up to hours), largely preventing their use in applications like cars, where rapidly changing power requirements are at hand.

The phosphoric acid fuel cell (PAFC) and the alkaline fuel cell (AFC) operate in the medium temperature range and have shown very good performance and high

durability [16–18]. However, they both use a liquid electrolyte, which makes the fuel cell handling and manufacturing more difficult and the cost of these systems will in most areas not be compatible with other fuel cell technologies.

Low temperature solid electrolyte fuel cells (PEMFC and subtypes such as the direct methanol fuel cell (DMFC) and the direct ethanol fuel cell (DEFC)) are especially scalable and cover a large power range [12]. The use of liquid fuel in the DMFC and DEFC makes the fuel handling relatively easy but to date, they have a considerably lower efficiency than the PEMFC. Each cell can be made thin, which allows for high energy densities. Commercial PEMFC stacks have shown gravimetric and volumetric energy densities around 1.5 kW kg^{-1} and 1.8 kW L^{-1} , respectively, which is comparable to typical combustion engines [5]. The low operating temperatures give short startup times (seconds or minutes). These fuel cells are currently the best candidates for use in automotive, portable electric devices, and small scale backup power [12].

There is also a rather new family of fuel cells termed biological fuel cells (BFC), which include microbial fuel cell (MFC) and enzymatic fuel cells (EFC). These fuel cells use organic molecules such as sugars, alcohols and other hydrocarbons as fuel, and the reactions are carried out by microbes or enzymes. Possible applications for BFCs range from in vivo devices that supply electricity to implants (such as pacemakers and insulin pumps) using hydrocarbons from the blood stream as fuel, to larger setups that can clean waste water while generating electricity [19].

2.4 The Polymer Electrolyte Fuel Cell

The polymer electrolyte membrane fuel cell (PEMFC), also termed proton exchange membrane fuel cell (PEMFC), polymer electrolyte fuel cell (PEFC), or solid polymer fuel cell (SPFC), was developed by General Electric in the early 1960s. The principle of the PEMFC is shown schematically in figure 2.1 and discussed in the following sections.

2.4.1 Fundamentals and Components

The heart of the PEMFC is the membrane electrode assembly (MEA), which is a three-layer structure consisting of the polymer electrolyte and two catalytically active electrodes that form anode and cathode, respectively, as indicated in figure 2.1. The electrodes facilitate transport of: *i*) ions to and from the membrane, *ii*) electrons to and from the current collectors, and *iii*) product and reactants. A complete MEA is about $200\text{--}500 \mu\text{m}$ thick and by the use of bipolar plates they can be stacked tightly to form a fuel cell stack. In the stack, the individual MEAs or cells are connected in series and thus the total voltage from a stack is the voltage of each cell (usually about 0.7 V) multiplied by the number of cells. The current is determined by the area of the individual cells in the stack and can be increased by connecting cells or stacks in parallel [13].

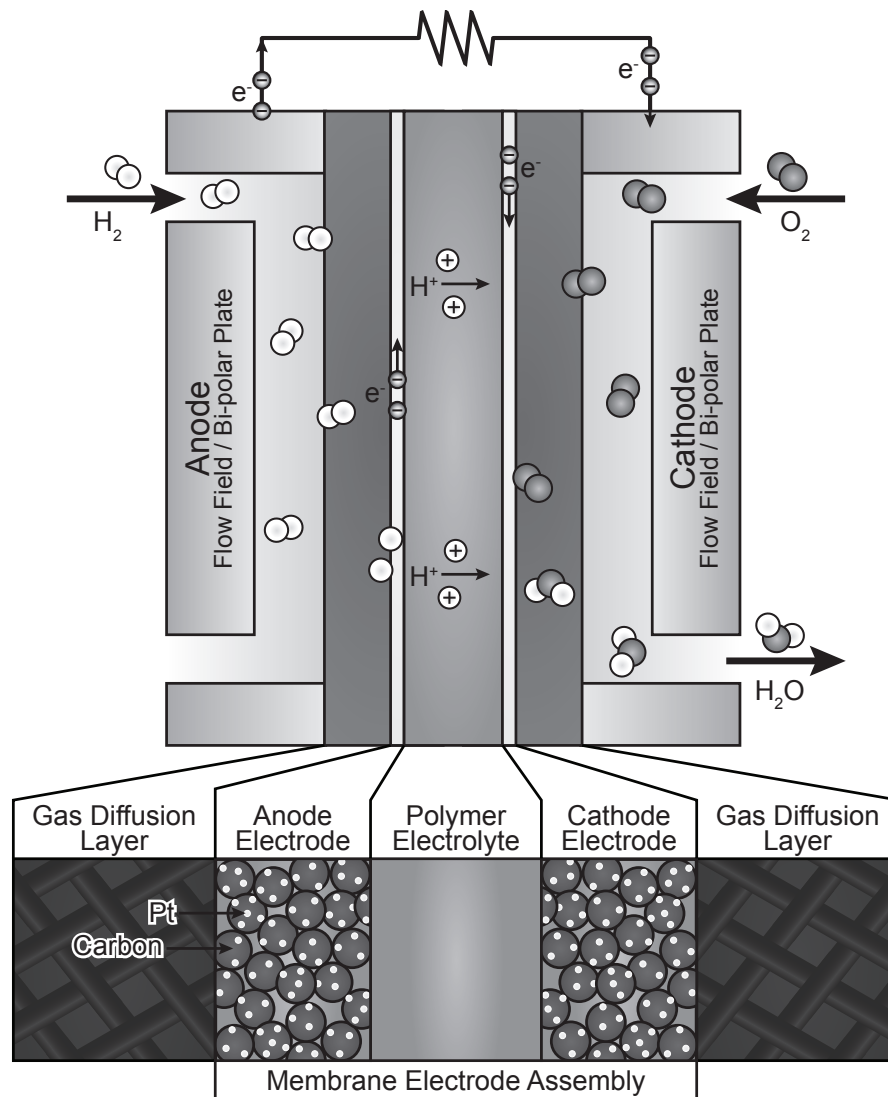


Figure 2.1: Schematic illustration of an operating PEMFC.

Proton Conducting Membrane and Ionomer

The proton conducting membrane, shown in the middle of figure 2.1, is a solid electrolyte that conducts protons from the anode to the cathode while it works as an insulator for electrons. It consists of a material called ionomer, which is a polymer that contains ionized repeating units. The thickness should be as small as possible in order to reduce the resistance of proton transport but must provide enough mechanical strength to keep the MEA together and be a seal between the reactant gases on either side. Typically, the thickness is 25–200 μm . Today, the most common ionomer in PEMFCs are perfluorinated sulfonic acid polymers such as Nafion[®]. Nafion consists of a polytetrafluoroethylene (PTFE, also known as Teflon) backbone grafted with fluorinated side chains terminated by sulfonic acid groups, HSO_3 [20]. The PTFE backbone is strongly hydrophobic whereas the sulfonic acid groups are strongly hydrophilic. This situation causes the sulfonic

acid groups to cluster within the material and upon hydration, networks of water filled channels are formed. In the hydrated regions, H^+ are loosely attracted to the SO_3^- and able to move inside the local water domain and be transported through the ionomer membrane [21, 22]. The proton conductivity of Nafion type ionomers is proportional to the degree of hydration and usually the gases entering the fuel cell need to be humidified, which requires water management to be added to the surrounding equipment. It also limits the operation temperature to be below 100 °C (at atmospheric pressure). The ionomer is also present in the electrode where it assures proton transport to and from the catalyst particles and acts as a binder to increase the mechanical stability. The ionomer development is aimed at new and improved materials with reduced manufacturing costs, improved stability and proton conduction, which can operate at higher temperatures and with low or no external humidification [23–25].

Electrode and Catalyst

A key function of the electrode is represented by the catalyst layer, shown at each side of the membrane in figure 2.1. The electrode consists of active catalyst particles and a support and must be an electric conductor and should facilitate transport of ions, gases and water to and from the catalyst sites [26]. The catalyst layer is typically based on a carbon black support onto which finely dispersed Pt nanoparticles, 3–6 nm in size, are deposited and a thin layer of ionomer is added to insure proton conduction. Carbon blacks, such as Ketjen Black or Vulcan XC72 have almost spherical primary particles around 25–100 nm in size. These primary particles are built up of small crystallites consisting of graphite patches of a few layers in a turbostratic arrangement. When crystallites stick together they can induce a microporosity ($\varnothing < 2$ nm) in the particles. As the primary particles cluster to form aggregates, mesopores ($2 < \varnothing < 50$ nm) and macropores ($\varnothing > 50$ nm) are formed. This gives the electrode a very high surface area, typically several hundred $m^2 g^{-1}$ [27]. Carbon black is often termed amorphous carbon, which is somewhat confusing as most of the carbon atoms are positioned in crystallites. The crystallites, however, are arranged more or less amorphously.

Anode and cathode electrodes can, in principle, be identical. However, in applications they differ in structure and composition in order to optimize the different processes occurring on the anode and cathode. The reaction rate of the ORR is several orders of magnitude slower than the HOR. Thus, the cathode side usually has a higher catalyst loading than the anode [28]. The hydrodynamic properties of the cathode electrode should be optimized to handle the fact that water is produced and needs to be transported out of the cell. Electrodes are generally fabricated by printing, spraying or brushing an electrode ink, which is a suspension of catalyst powder in dilute ionomer solution and a solvent. The thickness of an electrode layer is usually 5–20 μm .

Gas Diffusion Layer

The gas diffusion layer (GDL) acts as a current collector, it distributes gases and prevents flooding of the electrodes. It is located between the electrodes and the gas channels of the end-plate (for a single cell) or the bipolar plate (for a stack), as indicated in figure 2.1. Usually, it consists of a porous carbon fiber paper or woven cloth and often also a microporous layer (MPL) of carbon black. The hydrophilic properties can be controlled by impregnation with, e.g. PTFE. A complete GDL has a thickness between 100–500 μm [26, 27].

Gas Distribution and the Bipolar Plate

A gas distribution system is needed to supply H_2 and O_2 evenly over the active area of the MEA in order to assure a homogeneous operation of the fuel cell. This is usually realized by pressing a solid material with machined gas channels onto the GDL, as indicated in figure 2.1. For single cells, the gas channels are incorporated in the end-plate or in a separate current collector that also enables the cell to be compressed evenly. In a fuel cell stack, gases need to be distributed to all cells. In the latter case, the so-called bipolar plate is employed. The bipolar plate is usually made from graphite or coated stainless steel and act as cathode on one side in one cell and anode on the other side in the next cell. It gives mechanical stability to the stack, compresses and seals the cells and has gas channels to distribute gases. It is important that the plates have high electric and heat conductivity, are chemically stable, and gas tight [29]. Ideally, the bipolar plate should be as thin as possible to reduce electrical resistance and make the stack small and light weight. However, this makes the gas channels narrow and increases the pressure drop over the stack. The compromise is that the bipolar plates, typically, comprise most of the stack volume and as much as 80 % of the weight. Issues in designing bipolar plates include contact resistance, corrosion protection, flow field patterns, material and manufacturing routines and cost [30, 31].

Sealings and Gaskets

In order to make the fuel cell gas tight, the contacts between different components must be properly sealed. Popular gasket materials include silicone rubbers and hydrocarbon, or fluorocarbon elastomers. It is important that the gaskets are stable in the fuel cell environment and do not release harmful substances that can poison the catalyst or the electrolyte. Degrading gaskets may lose their sealing properties and failing gaskets are fatal to the fuel cell and can lead to leakage of H_2 [32].

2.5 Electrocatalysis

Electrocatalysis refers to electrochemical systems in which catalysts are employed, such as fuel cells. To examine these systems, both electrochemistry and catalysis need to be understood; on their own, and how they interact.

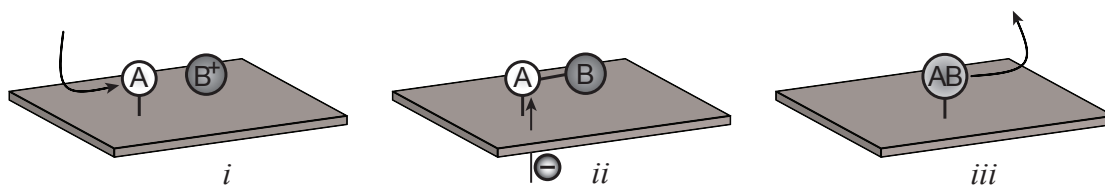


Figure 2.2: The fundamental steps of an electrode reaction. In this case, electron transfer is from the electrode to an adsorbed species on the surface — a reduction reaction.

2.5.1 Electrochemistry

Electrochemical reactions are a class of chemical reactions, which involve the transfer of charge across the interface between a solid and an adjacent solution face. The process when electrons are passed between the electrode surface and an atom or molecule adsorbed on the surface are termed electrode processes or electrode reactions [33–35]. In the simplest case, an electrochemical reaction proceeds in three steps, as illustrated in figure 2.2: *i*) adsorption of reactants at the liquid–solid interface, *ii*) electron transfer between the reactant and the electrode, and finally *iii*) desorption of the products from the electrode surface. During electrochemical reactions, the electrodes are charged, which gives rise to an electric double layer, a separation of negative and positive charges (ions) close to the electrodes [35]. This means that a positively charged surface will have a layer of predominantly negatively charged ions in the electrolyte close to it and vice versa.

A thermodynamically favorable process ($\Delta G < 0$) is used to generate an electric current and the power produced is dependent on the rate of the reaction and the energy difference between the reactants and products involved in the reaction. Electrochemistry can also be used to drive thermodynamically unfavorable processes ($\Delta G > 0$), for example electrolyzing water, charging of batteries, or electroplating. In this case, a current is supplied to the system and to, some extent, the rate of the reaction can be controlled by the applied current/voltage.

Pt electrochemistry is one of the most thoroughly investigated electrochemical systems [35]. In the voltage window of an operating fuel cell, Pt is not inert and interactions with the surrounding media (usually water) induce chemical reactions on the metal surface. This is readily seen in cyclic voltammetry (CV) measurements in inert environment. Figure 2.3 shows a CV for a polycrystalline Pt foil measured in N_2 -bubbled 0.5 M H_2SO_4 in a standard three-electrode half-cell configuration. At potentials below 0.4 V vs. the reversible hydrogen electrode (RHE) hydrogen adsorption and desorption peaks are seen and the peak shapes and positions are somewhat depending on the exposed crystal planes of Pt [34]. The integrated peak charges may be used to evaluate the electrochemical active surface area and for polycrystalline Pt, a fully covering monolayer of (underpotential deposited (UPD)) H is assumed to correspond to a charge of $210 \mu\text{C cm}^{-2}$ [36]. In the forward scan, above 0.8 V, Pt is oxidized and depending on scan conditions, several different oxides may be produced [37]. On the reverse scan, Pt oxides are reduced to metallic Pt.

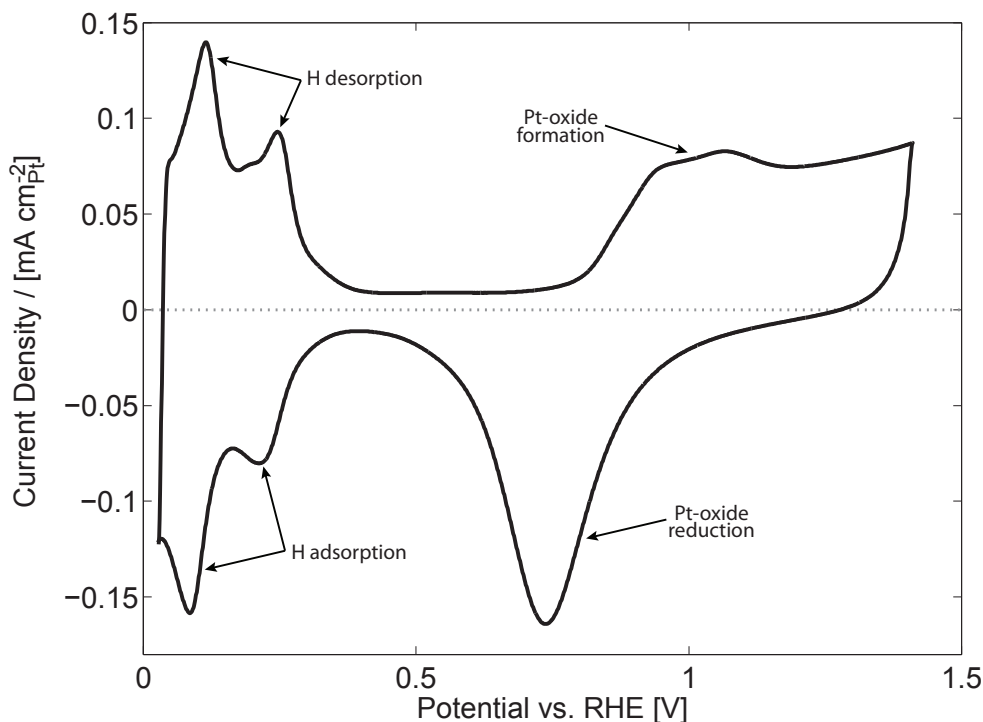


Figure 2.3: Cyclic voltammogram of polycrystalline Pt measured in 0.5 M H_2SO_4 .

CV on single crystal Pt electrodes displays voltammograms that are very different from the polycrystalline case and are unique for each crystal plane [38]. This also suggests that reactions taking place on different crystal facets may proceed through different mechanisms or at different rates. This has been shown both theoretically and experimentally, mainly for the ORR but also for the HOR on Pt [38–40].

2.5.2 Heterogeneous Catalysis

A catalyst accelerates a chemical reaction without being consumed. In standard heterogeneous catalysis, the process proceeds by adsorption of molecules from a gas or liquid phase onto the catalyst surface where they react, often in several successive steps, and subsequently the products desorb. A catalyst increases the rate of a reaction by introducing new reaction paths or lowers the activation energy of a rate-limiting step, i.e. it changes the kinetics, but not the thermodynamics of the reaction. This fundamental aspect of catalysis is illustrated schematically in figure 2.4. The rate of the reaction is essentially determined by the highest activation along the reaction coordinate — the lower the barrier the higher the rate, and the dependence is exponential.

Similarly to an electrochemical reaction, catalysis involves three basic steps, as indicated in figure 2.5: *i*) bonding of molecules to the catalyst surface, *ii*) reaction on the surface, and *iii*) separation of the formed product from the surface. If the second step is reaction between adsorbed species on the surface, it is called

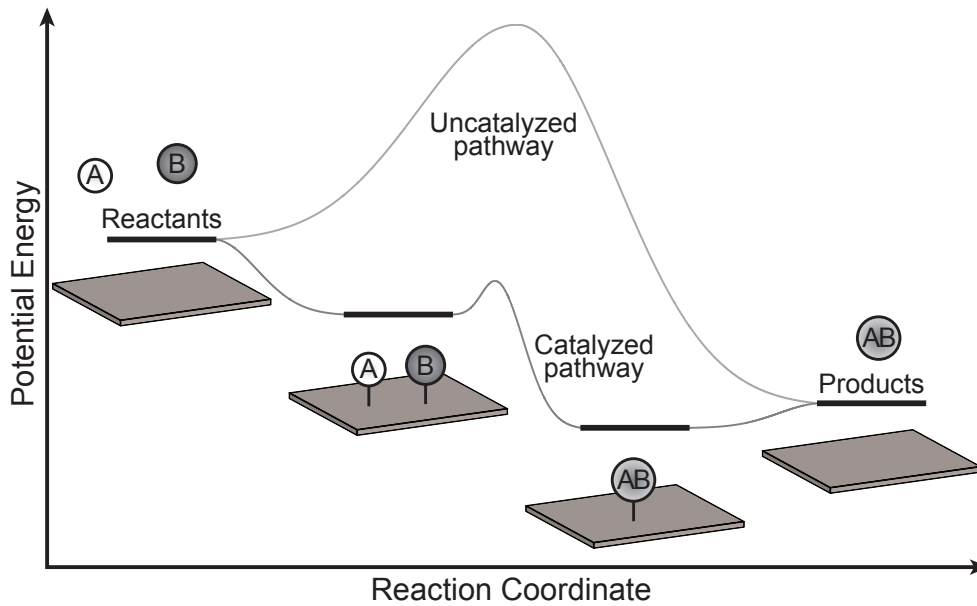


Figure 2.4: Schematic illustration of catalyzed and uncatalyzed reaction pathways.

a Langmuir–Hinshelwood mechanism whereas if one of the reactants is taken directly from the gas or liquid face, the mechanism is termed Eley–Rideal [41]. Most practical catalysts and especially fuel cell catalysts consist of active catalyst particles with sizes on the nanoscale, deposited on a support. In such systems, the support can influence the catalyst in several ways, e.g. electronic modifications [42] and spill-over of active species [43]. The rate of the overall reaction is limited by the rate-limiting step and a good catalyst must have a balance between binding energies of reactants, intermediate complexes and products with activation barriers as low as possible.

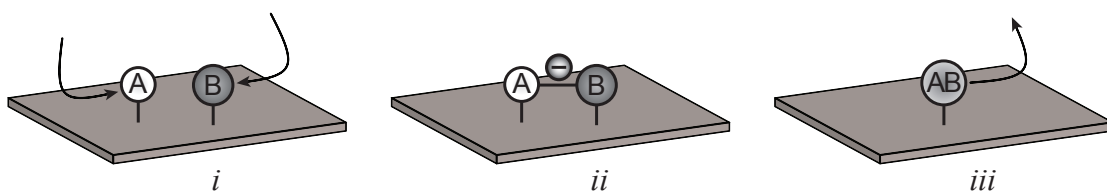


Figure 2.5: The fundamental steps of a catalytic surface reaction.

2.5.3 Fuel Cell Electrocatalysis

For the fuel cell to deliver a high amount of energy, the chemical reactions have to occur at a high rate and, typically, a Pt catalyst is employed. However, unlike traditional heterogeneous catalysis, the processes take place in the presence of an electrical potential, which influences the catalyst in several ways. A change in potential can be similar to a temperature or pressure change in regular catalysis, which is evident from the definition of change in Gibbs free energy, G

$$dG = -SdT + Vdp - dW_{elec} \quad (2.4)$$

which is derived from the first and second laws of thermodynamics [14]. S is the entropy, T is the temperature, V is the volume, and P is the pressure. The term W_{elec} is the electric work, defined as the work done by moving a charge Q_c through an electric potential, E

$$W_{elec} = Q_c E \quad (2.5)$$

and if the charge is carried by electrons

$$Q_c = nF \quad (2.6)$$

where n is the number of moles of electrons transferred and F is Faraday's constant. Thus, the driving force of chemical reactions, dG is changed when the potential is changed. This implies that reactions can be increased (or suppressed) by a change in potential. Moreover, the state of Pt (as seen in figure 2.3), the environment close to the Pt, and also the support material will change with applied potential, which implies that the system will be different at different potentials. In an operational fuel cell, the potential will change due to the applied load and in turn affect the chemical reactions and the performance of the cell.

2.6 PEMFC Performance

From basic thermodynamic and kinetic theory, a number of fundamental relationships that dictate the theoretical fuel cell performance can be derived.

2.6.1 Thermodynamics

The thermodynamic theory rests on a few basic laws that are used to describe and track properties of a system in terms of energy and entropy. The first law of thermodynamics states the conservation of energy; energy cannot be created nor destroyed. The second law states that the entropy of a system and its surroundings must increase or at least remain zero for all processes [14].

$$1^{st} \text{ law, } \quad dU = dQ - dW \quad (2.7)$$

$$2^{nd} \text{ law, } \quad dS_{univ} \geq 0 \quad (2.8)$$

where U is the internal energy of a closed system, Q is heat, and W is work. When considering chemical reactions, enthalpy, H and Gibbs free energy are more

practical than U since they can be measured. H and G are in turn related to the internal energy

$$G = U + pV - TS = H - TS \quad (2.9)$$

Equation 2.4 relates the change in Gibbs free energy to changes in temperature, pressure and electric potential. For a constant temperature, constant pressure process and using molar quantities for a reaction, this reduces to

$$\Delta\hat{g}_{rxn} = -nFE \quad (2.10)$$

The overall PEMFC reaction, i.e. H_2 and O_2 forming water (reaction 2.1) has $\Delta\hat{g}_{rxn}^0 = -237.17 \text{ kJ mol}^{-1}$ at standard state conditions ($T = 25 \text{ }^\circ\text{C}$ and $P = 1 \text{ bar}$). Thus, the reversible voltage for a $\text{H}_2\text{-O}_2$ fuel cell operating at standard conditions is

$$E^0 = \frac{\Delta\hat{g}_{rxn}^0}{nF} = 1.23 \text{ V} \quad (2.11)$$

which is the theoretical, upper limit of the reversible potential in a PEMFC at standard state conditions. The term reversible means that the system is at equilibrium. When current is drawn from the system, this equation is not valid.

Thermodynamics can also be used to determine the reversible fuel cell efficiency. Efficiency, ε , can be defined as the amount of useful energy that can be extracted, divided by the total amount of energy released in the system. Equation 2.4 states that the maximum amount of energy available to do electric work is the change in Gibbs free energy of the reaction. The total amount of energy released in the reaction is the change in enthalpy. The fuel cell efficiency is then simply

$$\varepsilon_{FC} = \frac{\Delta\hat{g}}{\Delta\hat{h}} = \left\{ \begin{array}{c} \text{Standard} \\ \text{State} \end{array} \right\} = \frac{\Delta\hat{g}^0}{\Delta\hat{h}^0} = 0.83 \quad (2.12)$$

Thus, the maximum electrical efficiency at room temperature is 83 %.

2.6.2 Kinetics

In ordinary chemical reactions, electrons are transferred between the reacting species directly, whereas for electrochemical reactions, electrons are transferred between the reacting species and the electrodes. Thus, there is always a current present when reactions take place and it is related to the rate of the reactions. For the overall PEMFC reaction



k_f and k_b are the rate constants for the forward and backward reactions, respectively.

From classical kinetic theory, the reaction rate depends on reactant concentration, C , the rate constant, k , the activation barrier, ΔG^\ddagger , and temperature. The net reaction rate may be written as

$$\nu = \nu_f - \nu_b = k_f C_R^* e^{\left(-\frac{\Delta G_f^\ddagger}{RT}\right)} - k_b C_P^* e^{\left(-\frac{\Delta G_b^\ddagger}{RT}\right)} \quad (2.14)$$

where R is the gas constant, subscripts R and P represents reactants and products respectively. Superscripts (*) are used to highlight the fact that the products and reactants are absorbed on the catalyst surface. As current is nothing more than a rate of electrons, the reaction rate can be related to the measurable current, i , which is the rate at which electrons are released in the net reaction

$$i = i_f - i_b = nF(\nu_f - \nu_b) \quad (2.15)$$

At thermodynamic equilibrium, there is no net reaction and the current is zero. From this relation the exchange current density, i_0 , is defined

$$i_0 = i_f = i_b \quad (2.16)$$

When current is drawn from the system, the operating potential, E , will be lower than the equilibrium potential, E^0 . The potential difference ($E^0 - E$) is defined as the overpotential, η , and represents the losses in the system. As the potential is changed from equilibrium, the activation barriers are changed. To relate the change in activation barrier with potential, a term called transfer coefficient, α , is introduced. The value of α represents the symmetry of the activation barrier and for a symmetric reaction the value is 0.5. A change in potential to a more positive value lowers the energy of the reactant electrons. The activation barrier of the oxidation (backward reaction, ΔG_b^\ddagger) is lowered by a fraction of $(1 - \alpha)F\eta$, whereas the reduction reaction (forward reaction, ΔG_f^\ddagger) is increased by a fraction of $\alpha F\eta$. This makes it possible to express how the current density depends on the overpotential

$$i = i_f - i_b = i_0 \left(e^{\left(\frac{\alpha n F \eta}{RT}\right)} - e^{\left(-\frac{(1-\alpha)n F \eta}{RT}\right)} \right) \quad (2.17)$$

This relation is called the Butler–Volmer equation and in this form it assumes that the concentrations of reactant and products on the surface are unaffected by the net reaction. The current produced by the electrochemical reaction increases exponentially with overpotential and an increase in current results in a loss of voltage (activation loss, η_{act}). For large η , the second term becomes negligible and η becomes a linear function of the logarithm of the current and this is described by the Tafel equation

$$\eta = \left(\frac{RT}{\alpha nF} \right) \ln i - \left(\frac{RT}{\alpha nF} \right) \ln i_0 = b \ln \left(\frac{i}{i_0} \right) \quad (2.18)$$

where the constant b is called the Tafel slope. A fast reaction will have a low b and a high i_0 , which implies that the current will be high even at small η . The E^0 value calculated in equation 2.11 is the equilibrium potential at standard conditions and assumes 100 % H₂ and O₂. When the fuel cell is running at other conditions, the equilibrium potential is described by the Nernst equation

$$E_{eq} = E^0 + \frac{RT}{nF} \ln \frac{P_{H_2} P_{O_2}^{1/2}}{P_{H_2O}} \quad (2.19)$$

2.6.3 Transport

Two types of transport is required in order for the fuel cell reactions to occur, *i*) mass transport of reactants and products to and from the catalyst and *ii*) charge transport of electrons and protons between the electrodes.

Mass Transport

Mass transport occurs via diffusion and/or convection. Convection refers to transport of a species under the action of mechanical forces, such as motion of a fluid or gas, while diffusion refers to transport of species due to concentration gradients. Diffusion is restricted by the molecular motion and is dependent on temperature and the dimensions of the space where diffusion takes place. It is, thus, far less “effective” than convective transport.

In the fuel cell, reactant gases are supplied through the gas channels in the bipolar plates and diffuse through the GDL to the active catalyst sites. At sufficiently high current densities, the diffusion will not be able to supply reactants and/or remove products at high enough rates, which causes the performance to radically decrease with increasing current. This is termed mass transport losses (η_{trans}) or Nernstian losses.

Charge Transport

Charge is transported via electrons moving in the outer circuit and via protons moving through the electrolyte. The transfer of electrons is rarely an issue in single cell fuel cells as the electrode, the gas diffusion layer, and the current collectors are good electric conductors. In fuel cell stacks, however, contact resistance between the bipolar plate and GDL can create measurable losses. But in general, the losses associated with electron transfer are small. Proton transport, on the other hand, is an issue. Typically, the proton conductivity of solid materials is significantly below that of liquid electrolytes. However, for proton conducting polymers such as Nafion, where proton conduction is essentially carried by hydrated protons, e.g.

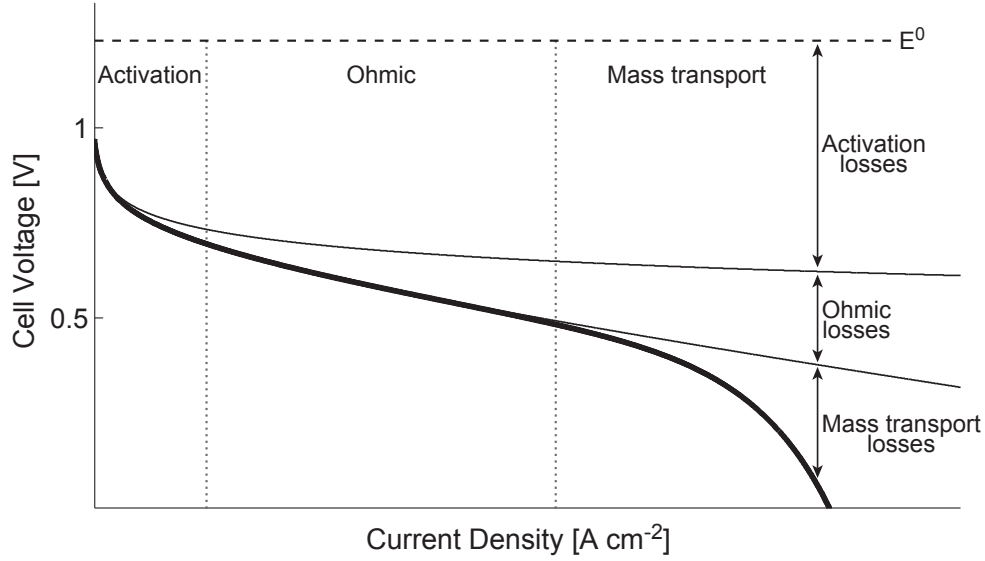


Figure 2.6: Schematic graph of the operating fuel cell potential curve and the impact of typical losses.

H_3O^+ , and governed by the diffusion coefficient of water, the conductivity can be close to that of liquid systems [44].

Charge transport resistance gives voltage losses, which are termed Ohmic or iR losses (η_{Ohm}). Ideally, the membrane should be gas tight and an electronic insulator. In practice, however, membranes will allow some H_2 and O_2 to pass through. These crossover gases will react chemically, without creating any electricity and represent lost fuel. Furthermore, a small amount of electrons may be transported through the membrane and energy is lost as the fuel cell is thereby partly short-circuited. These effects results in a voltage loss termed fuel crossover losses (η_{cross}) or internal current losses.

2.6.4 Losses

There are four types of irreversible kinetic and transport losses: *i*) activation-, *ii*) fuel crossover-, *iii*) Ohmic-, and *iv*) mass transport-. The sum of the losses represents the total overpotential, which will reduce the equilibrium potential

$$E = E_{eq} - \sum \eta = E_{eq} - \eta_{act} - \eta_{cross} - \eta_{Ohm} - \eta_{trans} \quad (2.20)$$

Figure 2.6 shows a schematic illustration of the resulting fuel cell operating potential curve where the contributions from the different potential losses are seen.

2.6.5 Efficiency

The reduced cell voltage, originating from the irreversible losses, implies that the efficiency is lower than the theoretical value. The potential varies with current and, consequently, the efficiency will vary with current. Fuel cells normally operate at about 0.7 V. As the ideal voltage is 1.23 V (at room temperature), the actual efficiency of the cell is

$$\varepsilon = \frac{E}{E^0} \frac{\Delta\hat{g}^0}{\Delta\hat{h}^0} = 0.47 \quad (2.21)$$

which is quite far from the theoretical limit of 83 %. As the potential decreases with increasing load, also the efficiency decreases, which implies that an oversized fuel cell has a higher efficiency. A combustion engine also has an efficiency that varies with the load. It can reach up to 40 % at some intermediate load [4], but in general, the combustion engine efficiency varies more with load than the fuel cell efficiency. It should also be mentioned that the possibilities of efficiency improvement are much larger for the fuel cell than for the combustion engine.

2.6.6 Stability

In applications it is important that the performance of the fuel cell does not decrease significantly over time and that the life-time is comparable with competing technology. All parts of the fuel cell are subject to different types of degradation, which may cause slow deterioration or fatal damage to the fuel cell. The degradation depends strongly on the choice of materials and the operating conditions, such as temperature, cell voltage, load cycling, and relative humidity [45, 46].

The proton conductive membrane may be affected by chemical degradation of the sulfonic acid groups or the main chains or by poisoning from impurities in the gases, electrodes, bipolar plates, or the sealing materials [47]. Mechanical stress can cause fatigue or structural changes that decrease the membrane strength [48]. These effects reduce the proton conductivity and can increase gas crossover.

In the catalyst layer, both the active Pt catalyst and the carbon support are sensitive to degradation or corrosion. Depending on the operating environment and potential, Pt can be dissolved into the ionomer or be transported to other Pt particles where it can redeposit in an Ostwald ripening process which results in particle growth, to inactive parts of the electrode, into the electrolyte membrane, or out of the cell with the product water [49]. The carbon support can be oxidized, which changes the hydrodynamic properties in the electrode, induces Pt particle sintering, and a collapse of the electrode structure. Figure 2.7 illustrates the effects of Pt dissolution a) and carbon corrosion b) occurring in the electrode layer. Furthermore, impurities from the gases or degrading components in the fuel cell can adsorb and block active Pt sites. All of these processes result in loss of active Pt surface area, which is commonly observed in durability studies. The electrode degradation is addressed in more detail in the next section.

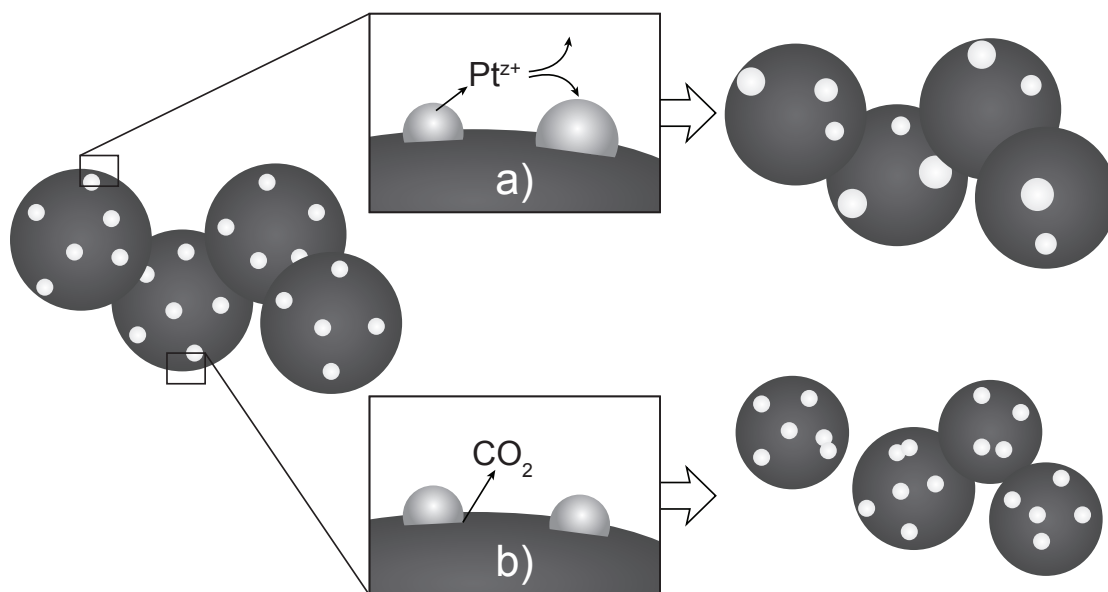


Figure 2.7: Schematic representation for the pathways of a) Pt dissolution and b) carbon corrosion.

The GDL often loses parts of the PTFE content during operation, which changes the hydrodynamic properties of the GDL and the water transport in the cell, which can lead to a decrease in performance [50]. The bipolar plates may corrode or oxidize, which can increase the contact resistance [51]. Gaskets may also release potentially harmful compounds in the MEA and they may degrade and lose their sealing properties [32, 52].

There are basically two methods to improve the fuel cell stability. One is to develop more stable and tolerant materials, another is to employ control systems to avoid operating conditions where degradation is pronounced. In order to choose which of the routes to take, or both, it is crucial to have fundamental knowledge about the processes involved. Understanding of the fundamental processes governing the degradation of fuel cells and strategies to improve the life-time has during the last decade received much attention in the fuel cell research.

2.7 Present PEMFC Research

The current fuel cell research includes all components and is conducted both from a scientific, curiosity driven approach as well as more applied research. In this section, the present PEMFC research is briefly reviewed.

2.7.1 Fundamental Electrocatalytic Reactions

The HOR and ORR on Pt are the most studied electrochemical reactions, but the reaction mechanism details are still controversial. The specific and changing conditions in the PEMFC influence the reactions and induce a variety of parallel

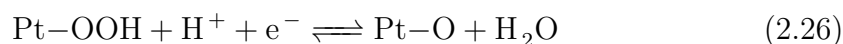
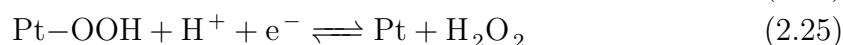
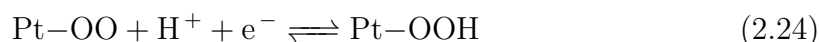
and competing processes. Model systems are the best tools to investigate the reaction fundamentals. The comprehensive review by Makovic and Ross [38] and a recent book, edited by Koper [53], highlights the strengths of model systems and shows how traditional surface physics can be utilized to study the electrocatalytic fuel cell reactions.

Oxygen Reduction Reaction

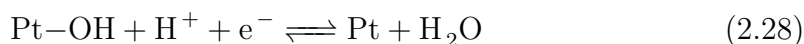
The complete ORR (reaction 2.3) is a four-electron reaction (for one O_2 molecule), including the transfer of four protons, the cleavage of an O–O bond and formation of two water molecules. The proposed reaction mechanisms for ORR on Pt are a dissociative and an associative adsorption of O_2 [54, 55]. The first step in the dissociative pathway is the dissociative adsorption of O_2



The associative pathway includes several initial steps



The final steps are common for the two mechanisms



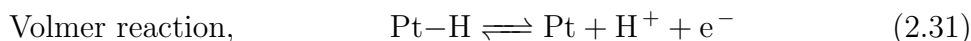
The associative mechanism includes the incomplete two-electron reaction producing H_2O_2 (reaction 2.25). H_2O_2 has been observed experimentally, which indicates that the associative mechanism is active, but the ratio between the dissociative and associative pathways or the individual reaction rates are difficult to determine since, for example, formed H_2O_2 can be re-adsorbed on Pt and be further reduced to water [56].

The research about this complex reaction network includes theoretical work [57], model system measurements [56, 58], as well as studies in fuel cells [59]. From density functional theory (DFT) it has been suggested that the binding energies of O and OH to the catalyst surface are key parameters for the ORR and that no one-component material has higher activity for the ORR than Pt, but that it should be possible to raise the activity by modifying the electronic properties of Pt, e.g. by alloying. Alloys of Pt and transition metals such as Co, Ni and Cr has

indeed shown an increased activity for the ORR [60, 61] which is likely related to changes in the electronic structure of Pt d-electrons [62]. The support material can also change the electronic structure and/or structure of Pt which also affects the ORR [63, 64]. Moreover, research is conducted on alternative catalyst materials for the ORR. Ideally, these should be non-precious metals with a low cost and a sufficiently high activity [65–67]. How different oxides used as supports affect the performance was examined in **papers I, III, and VIII** and a new type of model system to study the mechanisms of the ORR, specifically the H_2O_2 formation, was presented in **paper II**.

Hydrogen Oxidation Reaction

HOR on Pt in acidic electrolyte is one of the fastest known electrochemical reactions. It proceeds almost without activation and is assumed to follow the Tafel–Heyrovsky–Volmer mechanism [40, 68, 69]



This mechanism implies two reaction pathways, which might operate in parallel [70, 71]. Both pathways have the same final step, the one-electron oxidation of H ad-atoms, in the Volmer reaction (reaction 2.31). The initial step in the Tafel–Volmer pathway is the dissociative adsorption of hydrogen (reaction 2.29), which is followed by two separate Volmer reactions. In the Heyrovsky–Volmer pathway, a one-electron oxidation occurs simultaneously with chemisorption (reaction 2.30), before the reaction proceeds with a single Volmer reaction. The Tafel step is a pure chemical step, i.e. it does not involve electron transfer to the electrode and will not generate any current or have any direct potential dependence. In contrast, both the Heyrovsky and Volmer steps are electrochemical reactions possible to describe by the Butler–Volmer equation (equation 2.17).

The rapid kinetics makes it difficult to probe the reactions without mass transfer limitations, especially when the experiments are conducted in liquid electrolyte. Most of the HOR research has been carried out using model systems, such as rotating disc electrodes (RDE) [71], micro electrodes [69], grid electrodes [72], and low loaded electrodes in a H_2 pump setup [73]. The experimental difficulties surrounding the HOR has resulted in a wide spread of the reported kinetic parameters. The literature values for i_0 vary between 1 and 600 mA cm^{-2} [73]. Questions regarding the coverage and state of the intermediate adsorbed H atom and the reaction pathways have not yet reached consensus. New insights in the HOR kinetics, including a very high exchange current density was presented in **paper V**.

Oxidation of Small Organic Molecules

Today, the direct alcohol fuel cells (e.g. DMFC and DEFC) suffer from large overpotentials, which results in poor efficiency. The research connected to this deals with the complete reactions of oxidizing methanol and ethanol as well as studies of the intermediate compounds, such as CO, formic acid, and acetaldehyde [74].

Oxidation of CO is also of great importance for H₂ fueled fuel cells as the H₂ often is contaminated by traces of CO, which poisons Pt. Studies of electrocatalytic oxidation of CO is essentially carried out in either a “stripping” fashion where a pre-adsorbed monolayer of CO is oxidized in CO free electrolyte, or by continuous (bulk) CO oxidation [74]. Alloying Pt with, in particular, Ru changes the activity for CO oxidation, shifting the onset to lower potentials [75]. The mechanisms have been discussed in terms of a ligand effect, where the electronic structure of Pt is affected and the Pt–CO bond strength is reduced [76, 77] or a bifunctional mechanism where Ru supplies oxygenated surface species by dissociating water at lower potentials than Pt and these species diffuse to Pt sites [78–80]. Although the bifunctional mechanism has gained more or less general acceptance [81], the complete mechanism is still not clarified. In **paper VII**, a model system consisting of arrays of Pt/Ru nanoparticle pairs was demonstrated as a tool to study the reaction mechanism. CO oxidation was also performed for WO_x supported Pt in **paper VIII**.

2.7.2 Electrode Structure

Optimization of the electrode structure is a complex problem, which involves several tradeoffs between competing phenomena. The ultimate goal is to create as much of the three-face boundary as possible where all catalyst particles have the same environment and sufficiently high transport to and from them. Water transport is dependent on the electrode structure and will affect the fuel cell performance [82]. If too much liquid water is retained in the electrode it will become flooded and the transport of gases to the catalyst will be reduced while too little water will dry out the membrane and ionomer, which increase the proton transport resistance. The structure of the carbon support and the electrode preparation methods will influence the pore size distribution which affects the transport of water and gases in the electrode [83]. Studies have shown positive effects of introducing ordered structures in the electrode, such as carbon nanotubes (CNTs) or nanofibers (CNFs) [63, 84, 85]. There is also research aiming at designing extremely ordered electrode structures, for example by fabricating Pt covered nanowiskers [86, 87].

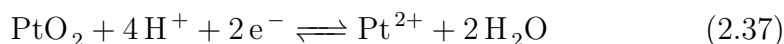
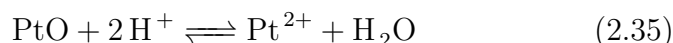
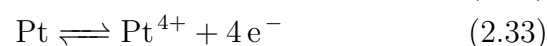
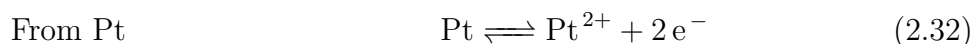
In order to increase the surface area of the active catalyst, the particle size should be as small as possible. However, for Pt, the (surface) specific activity increases with particle size and has its maximum for the surface of bulk Pt which leads to a maximum in the mass activity around 3.5 nm [88].

2.7.3 Electrode Degradation

The current research on electrode degradation has recently been summarized in the review articles by Borup et al. [45] and de Bruijn et al. [46] as well as in a book edited by Büchi et al. [89]. Degradation and durability of PEMFCs have inspired a broad research interest, basically during the last half-decade as a consequence of fuel cells approaching commercialization.

Pt Dissolution

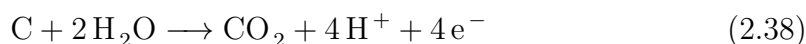
Pt dissolution has been identified as one of the main reasons for the limited life-time of PEMFCs. It is believed that repeated oxidation-reduction cycles increase the Pt dissolution and a two- and four-electron mechanism from Pt or Pt oxide has been proposed [90].



Pt dissolution and particle growth in operational fuel cells are only possible to detect indirectly from e.g. a decrease in active surface area, or by analysis after the electrochemical experiments [91]. Additionally, Pt dissolution has been studied in model systems by detection of Pt ions [92] and monitoring weight changes with electrochemical quartz crystal microbalance (EQCM) [93–96]. The dissolution has also been shown to accelerate in the presence of compounds that can form complexes with Pt, such as Cl [93, 94]. The Pt dissolution can be reduced by introduction of Au clusters [97] or by alloying with transition metals, in particular Co [98, 99]. However, the alloying compounds have a tendency to leach from the alloy [100, 101]. Pt dissolution was examined in **paper IV**.

Carbon Corrosion

Carbon is thermodynamically unstable at the higher potentials in the fuel cell environment, but owing to the slow kinetics, it is generally assumed that the corrosion rate can be maintained at low enough levels. However, this is often not the case. The overall electrochemical oxidation of carbon to CO_2 is



This reaction has several possible intermediate steps that might be active depending

on the operating parameters and composition of the electrolyte [102]. Carbon corrosion can be observed after fuel cell operation as a decrease of the electrode thickness and reduced hydrophobicity due to formation of oxidized surface species [103]. The formation of CO_2 has been shown in differential electrochemical mass spectrometry (DEMS) studies in model experiments [104, 105] as well as in regular mass spectrometry or infrared (IR) spectroscopy combined with fuel cells [106–108]. It has also been revealed that Pt can catalyze the carbon corrosion through several different pathways [104, 107, 109]. However, during potentiostatic measurements, Pt seems to have a negligible effect on the carbon corrosion [110]. Alternative support materials, such as graphitized carbon, CNT, metal oxides of, for example Ti and W, have been proposed in order to reduce the support corrosion problems [63]. In **paper IV**, the apparent activation energy of the Pt catalyzed carbon corrosion was determined together with the dissolution rate of Pt during cycling using EQCM and model electrodes. The stability of Pt supported on metal oxides in fuel cell experiments was addressed in **paper III**.

Catalyst Poisoning

Impurities can poison Pt, leading to a reduction of active sites. CO and S containing compounds that might be present in H_2 produced from reformation of diesel or CH_4 , binds strongly to Pt at low temperatures. While it usually is possible to regenerate the electrode from CO poisoning, it is very difficult to remove S, which accumulates in the electrode and permanently decreases the performance [111].

Model Systems for PEM Fuel Cell Electrodes

An intricate network of reactions and processes occur simultaneously on fuel cell electrodes. The different processes affect each other and rates and pathways are dependent on the operating conditions. In the study of real fuel cell electrodes, it is often difficult to separate different mechanisms influencing the results. One way to solve this “black box” problem is to make simplified experiments using model systems. However, it is important to keep in mind that a simplified system also implies that the system is changed. This can induce effects that do not occur in the real system and modify the conditions in such a way that the results are not relevant. In order to obtain detailed intrinsic information that account for combinatory effects, several different types of model systems can be employed. These systems can work on different levels and be classified by how close they are to the real system or how well they can isolate specific features. Figure 3.1 schematically illustrates the tradeoff between realistic and high control systems and a number of commonly used model systems are indicated. The range that the work presented in this thesis span is also illustrated.

3.1 Nanofabrication of Model Electrodes

Because the active catalyst particles in a real fuel cell are in the nanometer range, it is preferable to fabricate nanoscale model catalysts. Another important motivation for this type of fabrication is the fact that many of the processes in the fuel cell occur on length scales of nanometers and would change if the dimensions were increased.

Nanotechnology is the science and technology of materials where at least one dimensions is on the nanometer scale (larger than 1 nm, much smaller than 1 μm). Nanomaterials have different properties than their bulk counterparts, merely due to their small size [112]. There are two principal factors responsible for this, namely, an increased relative surface area and quantum effects. Pt is an FCC material with a lattice constant of 3.92 Å, corresponding to a nearest neighbor distance of 2.77 Å. A 1 nm film of Pt is equivalent to about 4 atomic layers and in such a film, every fourth atom is located on the surface. For nanomaterials that are restricted in $2D$

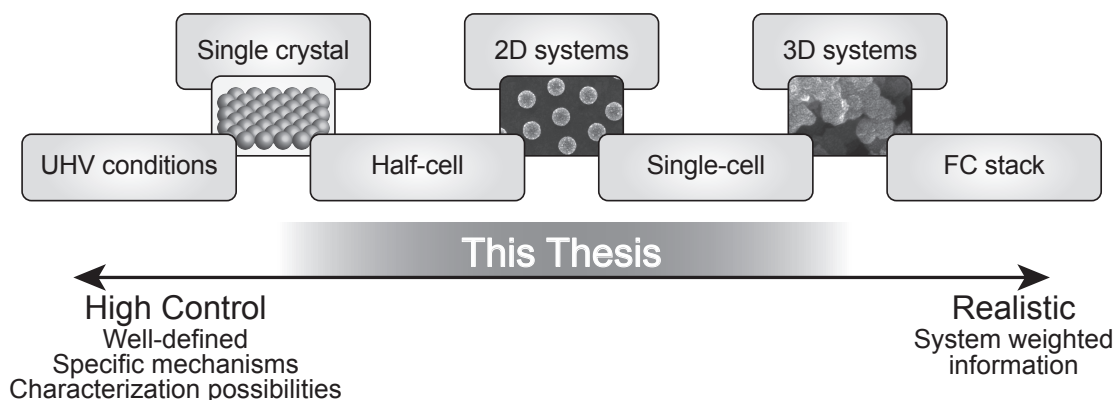


Figure 3.1: Schematic representation of the tradeoff between realistic and high control model systems. A few commonly used model systems as well as the range of this thesis work (shaded) are shown, approximately where they belong on this scale.

(wire) or 3D (particle), the ratio between surface and bulk atoms is even larger. For example, a 3 nm Pt particle has about 1000 atoms and about 40 % of them are located on the surface. Quantum effects originate from the spatial confinement of electrons in a small volume. For a metal, the electronic structure of nanomaterials show a rather smooth transition from the localized atomic orbitals in the isolated atoms to the band structure of bulk materials, with increasing number of atoms. A nanomaterial will typically have size dependent optical, electrical and magnetic properties.

Fabrication of nanomaterials, i.e. nanofabrication, can be carried out by a number of different techniques [113], often divided into three classes: *i*) pattern writing techniques, *ii*) pattern replication techniques, and *iii*) self-assembly techniques. The first two are “top-down” methods, while the latter is a “bottom-up” approach.

Pattern Writing Techniques

The pattern writing techniques include electron beam lithography (EBL), focused ion beam patterning (FIB), and scanning probe microscopy based lithography (SPML). These methods pattern the surface by “writing” virtually any 2D pattern within the resolution limit. They are serial processes, meaning that only one feature at a time is produced. Thus, they are not suited for fabrication of large areas and are both time consuming and expensive. The resolution limit of EBL and FIB are typically on the order of 10 nm while SPML techniques can position individual atoms. The main advantage of the pattern writing techniques is the extremely high control, which enables fabrication of defect free nanostructured samples.

Pattern transfer techniques

The transfer methods include photo-lithography (PL) and nano imprint lithography (NIL) and they use a patterned mask to define structures on the substrate. The

resolution is not as high as for the pattern writing techniques, but it is constantly improved and is today below 100 nm. Pattern transfer techniques are relatively cheap, fast, and well suited for fabrication of a large number of samples with the same pattern. However, a new mask must be fabricated for every pattern, e.g. a different nanostructure shape, size, or separation, which is normally done by EBL.

Self-assembly techniques

The most common self-assembly techniques include polymer self-assembly, colloidal lithography (CL), and various chemical methods, such as microemulsion, micellar, and dendrimer based fabrication. They utilize the inherent self organizing capabilities of the constituents (or building blocks, typically molecules or colloids) to define patterns on a surface and/or define the shape and size of the nanoparticles being fabricated. Control over the produced structures is obtained by using different molecules and/or changing the operational parameters. The practical limits in which structures can be controlled depend on the specific system, but are in general much smaller than that of the pattern writing techniques. On the other hand, the self-assembly techniques are parallel methods which enables patterning of large (several cm^2) samples. They are generally very fast and require relatively simple and low cost equipment. CL, also called nanosphere lithography, is based on the self-assembly of colloidal nanospheres on surfaces [114–116], where the colloidal particles functions either as an evaporation or an etch mask. In a recently developed version of CL, termed hole-mask colloidal lithography (HCL) [117], the colloids are used to define holes in a sacrificial deposition mask. By choosing the colloidal particle size and process conditions it is possible to control the size, coverage and the shape of the resulting nanostructures within a rather large domain [117–120].

Another technique, usually not mentioned among the self-assembly techniques but one that can be used to create self-assembled nanostructures, is deposition of non-continuous films. This can be achieved with physical vapor deposition (PVD) methods, such as evaporation or sputtering of material in vacuum. When the vaporized material lands on the substrate, the atoms have certain mobility on the surface. They will diffuse until they have lost their initial energy or reached a site with sufficiently high bonding strength to immobilize them, such as defects or step-edges, or other atoms already present on the surface. This leads to nucleation and island growth. Depending on the substrate material and temperature, evaporated material, and the impinging energy of the evaporated atoms, the growth process will follow different mechanisms (i.e. Volmer–Weber, Frank–van der Merwe, or Stranski–Krastanov growth) [121]. If the deposition is aborted before a fully covering film or large-scale island coalescence occurs, the deposited material will be in the form of separated nanosized particles. In general, large particles are formed when the interactions between the evaporated material and the substrate are low and the mobility of the evaporated material is high and vice versa. Deposition of a few (0.5–3) nm of Pt will result in individual Pt particles (about 3–10 nm in size) on most supports [122, 123]. The regime in which the structure can be controlled is typically much smaller than what can be achieved with the classic

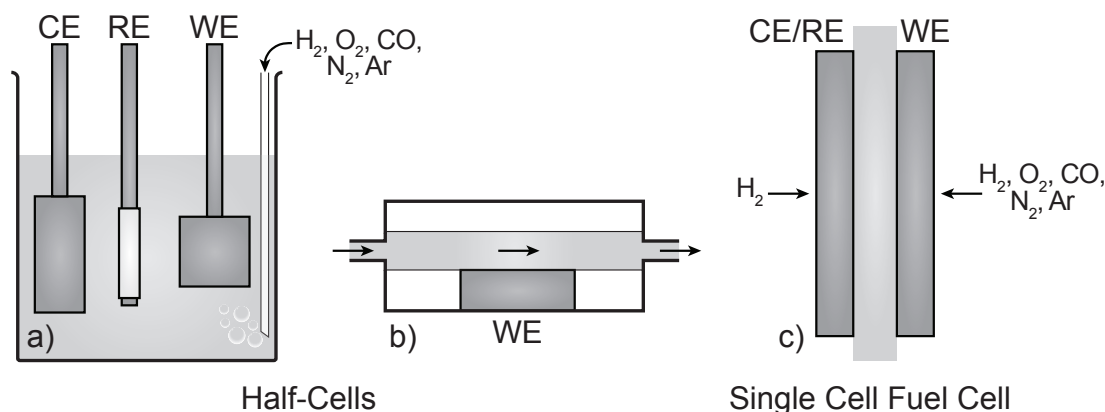


Figure 3.2: Schematic representation of common electrochemical measurement systems. a) and b) are examples of liquid half-cells and c) is a single cell fuel cell.

self-assembly techniques. The main advantages with thin-film deposition is that it is very fast, does not require any other materials (like polymers or surfactants) that might contaminate the catalyst, and that the particle size is roughly on the same order as realistic catalysts. The fact that the films are non-continuous allows catalyst-support interactions to be investigated.

Although, all of the techniques mentioned above are possible to use in electrochemical model systems, only the self-assembly techniques were employed in this work.

3.2 Electrochemical Measurement Systems

There are basically two types of electrochemical measurement systems in which fuel cell related model experiments can be performed; the liquid half-cell and the single cell fuel cell. The fundamental layout of the setups are illustrated in figure 3.2. These systems can be used to evaluate a variety of model electrodes, such as polycrystalline, single crystal, thin-film, nanostructured, or porous structures as well as standard materials. The setups can also be equipped with additional measurement devices to enable quantification of specific processes. These include detection of gas phase species with e.g. mass spectrometry (MS), liquid products with e.g. high performance liquid chromatography (HPLC), adsorbed species with e.g. IR techniques, electrode structure with e.g. scanning tunneling microscopy (STM), and electrode weight with quartz crystal microbalance (QCM).

3.2.1 Liquid Half-Cell

The liquid half-cell is the most commonly used electrochemical measurement setup and it can be found in a number of designs. In the simplest case, the system consists of a container filled with liquid electrolyte into which a reference electrode (RE), a counter electrode (CE), and the sample as working electrode (WE) are immersed,

as indicated in figure 3.2a. This is a three-electrode setup and the electrodes are typically connected to a potentiostat. The potential is measured between the WE and the RE while the current flows between the WE and the CE. It is possible to employ the simpler two-electrode setup where the CE and RE is the same electrode. However, in such a setup the actual potential of the working electrode is poorly defined and might change with current. Electrochemical reactions are studied by performing electrochemical measurements as different reactants, such as O_2 , H_2 , or CO are added to the electrolyte, or in reactant free electrolyte. In this type of half-cell, the electrode should be sufficiently small and the electrolyte volume sufficiently large so that the reactions that occur on the electrode surface do not change the electrolyte composition. To minimize concentration gradients around the sample, the electrolyte may be stirred or the sample may be rotated. The latter is employed in the rotating disk electrode (RDE) setup where the WE is a circular sample mounted in a rotating holder. The RDE setup can also be equipped with a second WE in the form of a ring, surrounding the sample in a rotating ring disk electrode (RRDE) setup where the ring can, for example, be used to detect products generated on the sample [35]. Virtually any type of electrode structure can be used in this type of half-cell, but the structure can affect the local mass transport, so thick and porous electrodes should be used with care. Polycrystalline and single crystal materials, thin-films of supported catalysts, and dispersed porous materials are the most used electrodes in this type of half-cell.

Another commonly used version of the liquid half-cell is the flow-through half-cell, also called thin-layer flow-cell, or simply, flow-cell (figure 3.2b). Here the volume of the measurement chamber is minimized, electrolyte is constantly flowing through the cell, and the WE is situated on a part of one of the walls in the chamber. As the liquid volume in the cell is small, it is possible to rapidly change the composition of the electrolyte, e.g. switching from inert to reactive electrolyte. It is also possible to analyze the products formed on the WE with very small time lags and negligible diffusion effects. For practical reasons, the CE and RE are often located outside of the measurement chamber but connected to it via the electrolyte inlet or outlet. The system can be combined with an MS in a differential electrochemical mass spectrometry (DEMS) setup to detect volatile products and/or intermediates from the WE [124]. It can also be equipped with a second WE to detect electrochemically active species formed on the sample [125].

3.2.2 Single Cell Fuel Cell

The single cell fuel cell, shown in figure 3.2c is, of course, the system which is closest to the real application. However, the results from this setup can be difficult to interpret as the performance of the fuel cell is not only governed by the intrinsic catalytic behavior of the active catalyst, but also depends on the transport of gases, water, protons, and electrons. Several of these processes are likely to be altered when, for example, an electrode with a new type of catalyst is to be synthesized, rendering it difficult to deconvolute the different effects. However, by designing model electrodes that have similar structures, these issues can be reduced. For

extremely low loaded catalysts, the transport processes in the electrode will barely be affected by the catalyst [73,126]. Evaporation or sputtering of catalysts material onto fuel cell membranes or electrodes can also be used as model electrodes [127–132]. Lithographically produced nanostructured electrodes can also be incorporated in single cell fuel cells [133]. Moreover, setups that are not true fuel cells, but operate in a fuel cell like manner have been presented [72,134]. By using model electrodes in single cell fuel cells it is, for example, possible to compare different catalyst materials and perform kinetic studies. Single cells can also be accompanied by additional equipment such as, MS and product water analysis to obtain further insights to the operation [107,108].

3.3 Electrochemical Measurement Techniques

A range of different electrochemical measurements can be performed to evaluate model systems. These can simulate real fuel cell performance, but also be used for characterization and fundamental exploration of the system. Electrochemical measurements are typically carried out using a potentiostat, which can control both the conditions in the system and perform measurements with very high sensitivity. A typical potentiostat can measure currents down to the pA or sometimes even fA level. 1 fA is equivalent to 6242 electrons passing every second and means that a one-electron reaction occurring at a rate of 10^{-20} mol s⁻¹ can be quantified.

During the measurements, the potentiostat will supply a potential while measuring the current, or vice versa. In voltammetry experiments, the potential is scanned at a certain rate and the generated current is recorded. Cyclic voltammetry (CV) is usually performed in the absence of reactive molecules to give information about the electrode materials, including electrochemical surface area (ECSA), presence of contaminants, and indications of resistance limitations [34].

Steady state polarization experiments are similar to voltammetry in that the current at given potentials is evaluated, but in this case the system is held at discrete potentials until steady state is reached (stationary measurements). This is done to remove pseudocapacitive currents, originating from variations in the surface coverage of adsorbed reaction intermediates and to assure that local temperature and concentration profiles are stable [14]. In lab-scale tests, however, it is for practical reasons common to scan the potential at a low scan rate (quasi-stationary measurements). Different scan rates may be used to determine a sufficiently low rate where the effects of potential change are negligible [35].

Other common electrochemical experiments include step change experiments, where the potential is stepped from one defined state to another while the current evolution is monitored in time. It is also possible to control the current, rather than the potential to evaluate the electrochemical reactions. Electrochemical impedance spectroscopy (EIS) is a technique where the impedance signature of the system is measured for a range of frequencies. It is often used together with an equivalent circuit describing the cell, which can be used to characterize the system [14,34,35]. The data can, for example, be used to deconvolute the potential drop caused by

charge transfer resistance, i.e. iR correction and enable determination of intrinsic kinetics parameters and other fundamental properties.

3.4 Physical Characterization

The main characterization of electrochemical model systems is, of course, the electrochemical evaluation. However, the measured quantities, e.g. the current, are non-specific and represent the sum of all reactions. For detailed understanding, additional measurements and characterizations are needed. To some extent, this can be achieved by complementary electrochemical measurements and/or by combining electrochemistry with other analysis techniques. However, it is also important to characterize the electrode structure and composition as these properties affect the electrochemical performance [14]. Physical characterization is also fundamental in the development of model electrodes. There is a large number of surface science tools and techniques available for this and this section presents the ones relevant to this thesis.

3.4.1 Microscopy

Microscopy refers to methods that image samples or objects that cannot be seen with the unaided eye. There are three basic branches of microscopy: *i*) optical microscopy, *ii*) electron microscopy, and *iii*) scanning probe microscopy.

Optical Microscopy

In ordinary optical microscopy, light is focused through a series of lenses that magnify the sample. When using visible light, the microscope has a spatial resolution around 200 nm. However, it can be possible to detect objects that are somewhat smaller than this. For example, Pt nanodisks of about 190 nm can be visualized.

Electron Microscopy

In an electron microscope, a beam of electrons is focused on the sample where they interact with the material. An image is generated by detecting the transmitted, scattered, or emitted electrons from the material. In the transmission electron microscope (TEM), the sample is made very thin (usually below 100 nm) and by detecting electrons that pass through it, high resolution (in some cases, atomic resolution) images can be obtained. As the electrons travel through the sample, they generate diffraction spectra that reveal the crystal structure of the sample.

In the scanning electron microscope (SEM), the electron beam is scanned over the surface of the sample and gives rise to a distribution of, mainly, backscattered (reflected, high energy) and secondary electrons (emitted from the sample, low energy). Different detectors are designed and positioned in such a way that they maximize detection of a specific type of electrons. The resolution is typically around 1 nm but the visualization of objects depends also on contrast differences. The

contrast (i.e. intensity variation) depends both on the topography and the type of material and it can sometimes be difficult to distinguish the two. In general, the secondary electrons are more suited for discriminating between different materials, whereas backscattered electrons provide a better topography view.

Scanning Probe Microscopy

The scanning probe microscope utilizes a physical probe that is scanned over the sample surface by the use of piezoelectric actuators. An image is generated by evaluating a specific type of interaction between the probe tip and the sample as the probe is scanned. These interactions include electric currents (STM), contact forces (AFM), as well as frequency variations when oscillating probes are employed.

3.4.2 Spectroscopy

Spectroscopy techniques, mainly, analyze the interactions or emissions of electromagnetic radiation (e.g. light) or particles (e.g. electrons) from a material. This can be done by shining light or electrons, sometimes ions, onto a sample and analyzing the absorption and/or emissions that follows. Matter can interact with incoming light or electrons and, depending on the electronic structure, dissipate or convert the energy through different channels. By analyzing the loss or generation of light or electrons, information about the structure of the material can be obtained.

In X-ray photoelectron spectroscopy (XPS), an X-ray beam illuminates the sample and gives rise to emissions of core level electrons. By detecting the kinetic energy of the emitted electrons, the binding energy of the electron is determined. The technique is elemental sensitive as the binding energy is well-defined for every element and electronic level. The chemical state of the material can be analyzed by detecting shifts in the binding energies. The penetration depth of the incoming X-rays can be as high as 1 mm, but as the electron mean free path is very short, the emitted electrons mainly originate from the topmost atomic layers. In most cases the sampling depth is < 10 nm and, thus, XPS is a very surface sensitive method.

Raman spectroscopy is based on inelastic scattering of photons by a molecule or solid through exchange of rotational or vibrational energy. By analyzing the shift in photon frequency and the intensity of the scattering events, information about the chemical bonding in the sample is obtained.

Energy dispersive X-ray spectroscopy (EDS or EDX) is a technique that often is incorporated in electron microscopes. The electron beam hitting the sample leads to emissions of secondary electrons (mainly K-electrons) and the process is accompanied by characteristic X-rays, as higher level electrons fill the empty states. By detecting these photons in a spectrometer, elemental analysis of the sample is possible.

In mass spectrometry, gases, evaporated material and other volatile species can be analyzed for elemental composition. In the setup, the components are ionized, accelerated in an electric field and then sorted and detected with respect to their mass to charge ratio (m/z).

Model Electrode Fabrication and Physical Characterization

This chapter describes the specific details of the fabrication and physical characterization of model electrodes carried out in this work. The results from the structure and composition analysis will be presented and discussed. From a fabrication point of view, two types of model electrodes were produced; thin-film and nanostructured catalysts. Thin-film catalysts were prepared by evaporating one or multiple materials onto flat or porous supports. Nanostructured electrodes were fabricated by lithographic methods on flat supports.

A number of characterization techniques were used to evaluate the structure and composition of the electrodes. Optical microscopy using visible light was used for rough analysis of fabrication steps for most of the samples. SEM analysis was used to characterize the morphology of almost all samples that were fabricated. In **paper VII**, EDX was performed together with SEM measurements. TEM was used in **papers I, IV, and VI**. Atomic force microscopy (AFM), in tapping mode, was used in the development of nanostructured model electrodes and in **paper IV** to characterize the surface of model electrodes. XPS was employed for elemental and chemical state analysis in **papers I, II, III, IV, VII, and VIII**. Raman spectroscopy was used to characterize carbon structures in **paper IV**.

4.1 Thin-Film Catalysts

All thin-film catalysts were prepared by thermal evaporation of metals using e-gun heating. Although the deposition technique was identical in all cases, the different supports used, yielded electrodes with specific features.

4.1.1 Thin-Film Catalysts on Nafion

Prior to evaporation of the catalyst, Nafion membranes (mainly the 117 type) were cut in appropriate pieces to fit in the fuel cell and cleaned by boiling in 3 % H_2O_2 for 1 h, in 0.1 M H_2SO_4 for 1 h, and finally in three successive baths of Milli-Q water for 1 h each before they were dried by pumping down in vacuum. Pt films of

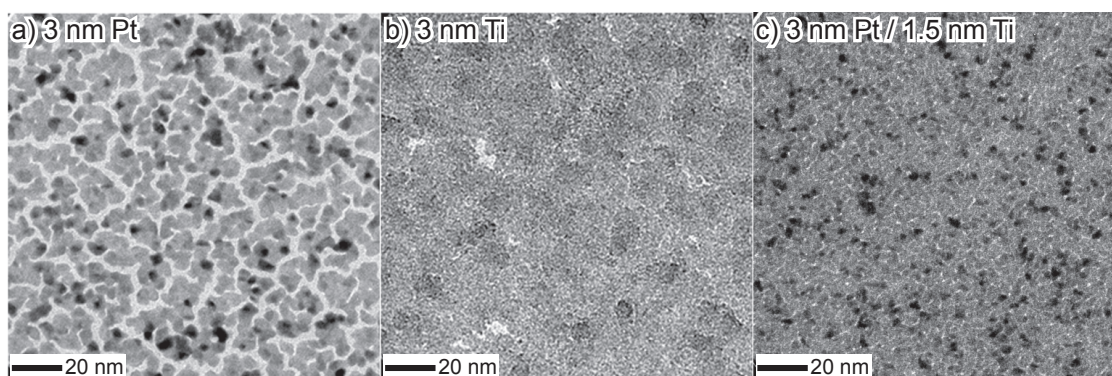


Figure 4.1: TEM images of thin-film catalysts deposited on TEM-windows. a) 3 nm Pt, b) 3 nm Ti, and c) 3 nm Pt on 1.5 nm Ti.

1–3 nm were deposited to obtain non-cohesive structures, whereas films of 1–10 nm or thicker were used for the reference and support materials.

As Nafion is a poor electric conductor, detailed SEM characterization of the catalyst structure could not be performed. The thickness of the membranes (Nafion 117 is about 180 μm) made TEM analysis impossible. To overcome this, TEM-windows [135] covered with a thin layer of Nafion were placed in the evaporation chamber with the membranes and used for TEM analysis. Figure 4.1 shows TEM images of three samples analyzed in **paper I**. Deposition of 3 nm Pt a) forms a non-coherent particle net-like structure while 3 nm of Ti b) fully covers the support. The structure of bi-metallic samples was found to be largely governed by the structure of the first material deposited. One example is given in c), where 3 nm Pt was deposited on 1.5 nm of Ti. It is difficult to separate the contrast originating from the Pt and the Ti and, thus, it is hard to determine the exact morphology of the respective materials. It is likely that Pt is more dispersed on the Ti than on Nafion since Ti interacts strongly with most materials (Ti is e.g. often used as adhesive layer for many metals). It was also seen in the electrochemical evaluation that Pt obtained an increased ECSA when deposited on Ti.

The Nafion membranes were in a dehydrated state during evaporation and when they were inserted into the fuel cell and subjected to humidified gases, they swelled, which caused the catalyst films to crack. For some samples, it was possible to separate the GDL from the membranes after the fuel cell measurements and the macrostructure could be characterized with SEM. The results revealed that the films cracked, but that the nature of the cracks (density and sizes) was similar, regardless of material.

One of the negative aspects of this type of model electrode is that three phase boundaries will only be created on a fraction of the deposited Pt. Good proton contact is assured as the Pt is in contact with the membrane and gas transport should not be any problem. However, to achieve electrical contact, the Pt has to be in contact with the GDL pressed on top. Because the GDL is highly porous, this contact is only possible for a small number of the isolated Pt particles. In the electrochemical evaluation, this was observed as a significantly smaller ECSA than

would be expected from the amount of material deposited. Approximately, only 10 % of the deposited Pt was available on the 3 nm Pt electrodes and an equally low mass specific ORR activity was observed (about $0.01 \text{ A mg}_{\text{Pt}}^{-1}$ [28]). The surface specific current densities on the other hand, were on the same level as what was expected. Moreover, it was found that electrodes with the catalyst deposited on Nafion degraded faster and in a different manner than ordinary electrodes. This was probably a result of the catalyst not being attached to the carbon electrode, but sitting on the non-static Nafion and when the membrane changed shape (due to swelling and drying) the catalyst moved into the membrane matrix and lost its contact with the GDL.

4.1.2 Thin-Film Catalysts on GDL

Carbel CL was the main type of GDL used and the material was cut in pieces of a few cm^2 and cleaned in flowing N_2 . This GDL has a microporous layer (MPL) and the subsequent evaporation was done on top on the MPL. As the MPL consist of spherical carbon black particles, there will always be carbon exposed in the structure after deposition of the catalyst. The MPL has essentially the same structure and composition as a regular fuel cell electrode layer, except that it does not contain any catalyst nor ionomer (but it has a small amount of PTFE to make it more hydrophobic). The exposed area where metal is deposited is significantly larger than the projected area, which means that the parts of the support where the surface normal and the path of the depositing material are parallel, will receive a relatively larger amount of deposition compared to the other parts [130]. Moreover, since most of the deposited material will land on curved surfaces, thicker layers can be deposited before large-scale island coalescence occurs, compared to flat supports.

Figure 4.2 shows SEM images of a) a bare Carbel CL GDL prior to thin-film deposition, b) 1.5, c) 3, and d) 6 nm of evaporated Pt. The three latter were used in **paper V** and the 3 nm Pt on GDL was also used as reference in **papers III and VII**. As can be seen for the 1.5 nm Pt sample, the Pt nanoparticles were about 2–3 nm in size and separated by a few particle diameters. On the samples with high loading, both the nanoparticle density and the size of the individual particles increased. On the 6 nm Pt sample, the nanoparticles started to form a network structure. As both the density and size of the nanoparticles increase with increasing amount of deposited Pt, also the surface area of the Pt increases with thickness (until a fully covering film is formed). This was also observed in electrochemical measurements of the Pt surface area in both liquid half-cell and fuel cell experiments.

The presence of isolated Pt particles was also confirmed by XPS measurements by analyzing the $\text{Pt}(4f_{7/2})$ core level electron peak position for samples with different amount of Pt. The position of the $\text{Pt}(4f_{7/2})$ peak should be about 71.2 eV for continuous and bulk-like Pt [136], and as can be seen in figure 4.3, this value is reached for the thickest films. For the thinner films, however, there is a shift in the binding energy to higher values. This has been reported as a local charging effect and does not reflect the native state of the Pt [137]. When small isolated particles

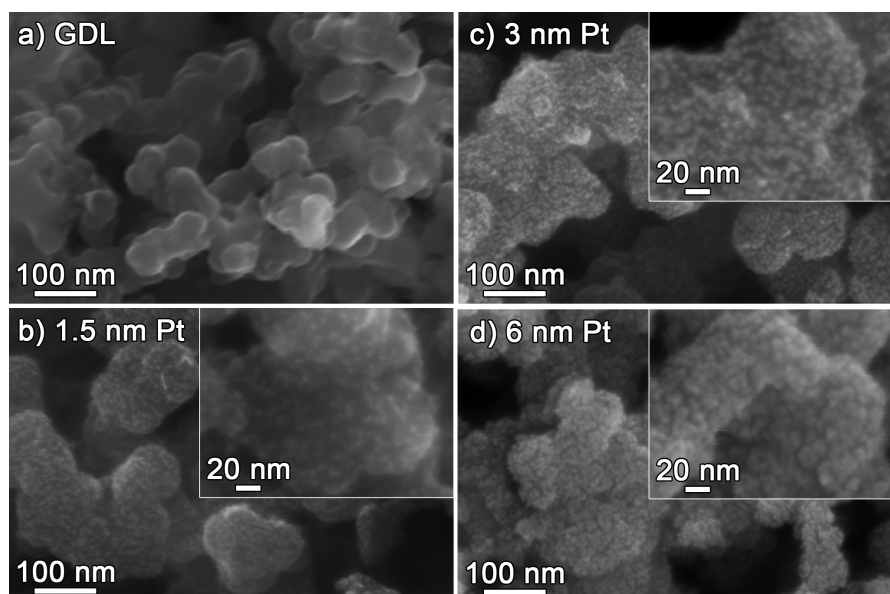


Figure 4.2: SEM images of evaporated Pt on Carbel CL GDL. a) bare GDL, b) 1.5, c) 3, and d) 6 nm Pt.

are excited and emit electrons, new electrons must be supplied via the support. This process is generally slower than the electron emission and gives the nanoparticles a net positive charge when the photo electron escapes from the particle. As the nanoparticles get larger, this effect gets smaller, because electron screening gets more effective. The trend in figure 4.3 is similar to that presented in [137], but as the GDL support is porous, the effect is extended to larger equivalent thicknesses. The interpretation of these results are also in good agreement with the SEM images shown in figure 4.2.

The structure of these model electrodes is fairly similar to that of real fuel cell electrodes, but the active catalyst is concentrated to just the top layer of the support. The overall catalyst loading is much lower (3 nm of Pt corresponds to about $6 \mu\text{g cm}^{-2}$), which results in low currents, low iR -losses, and limited water and heat production in the subsequent electrochemical evaluation. Compared to the electrodes where Pt was deposited on Nafion, these electrodes have a more realistic catalyst-carbon interaction. The GDL does not contain any ionomer, so proton contact must be achieved directly from the membrane during pressing. As the GDL is porous and the membrane is flat, only a fraction of the Pt particles will get this contact. Thus, in similarity with the case when Pt was deposited on Nafion, only about 10 % of the deposited Pt was active in the fuel cell. However, it was possible to increase the effective contact between Pt and the proton conducting electrolyte. From measurements in liquid electrolyte, where the electrolyte can penetrate the porous GDL, all deposited Pt was electrochemically active and the surface areas agreed with SEM images. The same high Pt utilization could be obtained also in fuel cell experiments by spraying the GDL with several layers of Nafion solution prior to pressing of the MEA. A few of these measurements were presented and

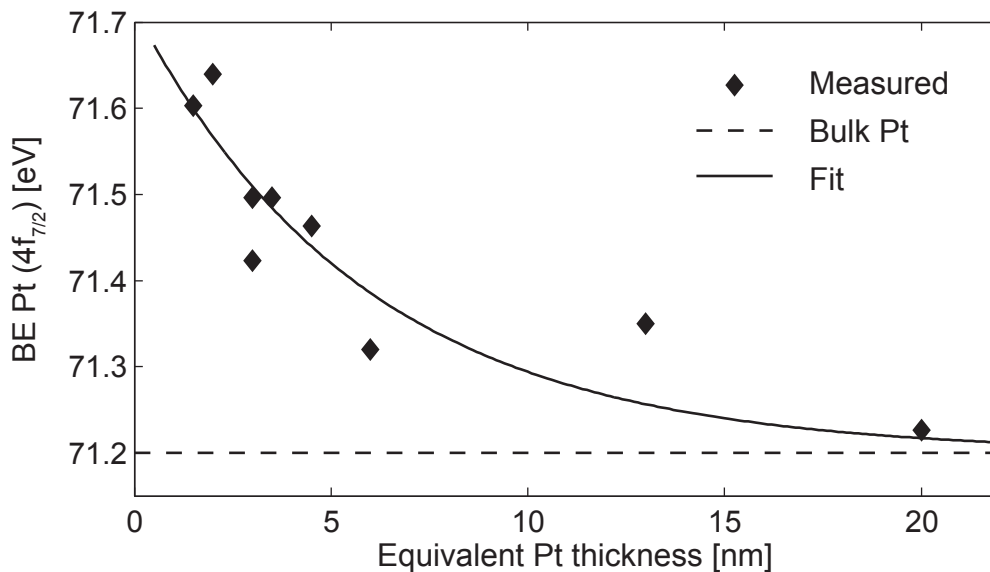


Figure 4.3: Apparent binding energies of Pt($4f_{7/2}$) electrons on evaporated Pt of varying thickness on GDL.

discussed in **paper VIII**.

Also on GDL it is possible to evaporate a support material and then deposit Pt on top to evaluate Pt–support interactions. This was done in **paper III** with metal oxides of Ti, Sn, Zr, W, and Ta and in **paper VIII** for additional W oxide samples. It was seen that most of the metal oxides formed smooth and fully covering films on the exposed surface of the carbon particles, but due to the small difference in contrast between the metal oxides and Pt in the SEM, it was difficult to analyze the Pt morphology.

4.1.3 Evaporated Carbon

Evaporated carbon was used as sample and support in **paper IV**. It was produced by thermal evaporation from a polycrystalline graphite source. This process is known to generate carbon black-like carbon [138], which should be a relevant model support for fuel cell related experiments. However, the amounts and sizes of nanocrystallites may be different to that of typical fuel cell carbons. Quartz crystals and Si-wafers were used as carriers for 50–100 nm carbon films. To analyze the carbon structure in more detail and compare it to standard carbon materials, Raman analysis was performed on the evaporated carbon, GC, and Vulcan XC72. Figure 4.4 shows the resulting Raman spectra after background subtraction between 800 and 1900 cm^{-1} where the first-order carbon features are expected. For polycrystalline graphite and amorphous carbon with some degree of crystallinity, two peaks, related to different vibrational modes are expected. The *D* peak, located around 1350 cm^{-1} is associated with the breathing mode of sixfold carbon rings and the *G* peak, which results from in-plane bond stretching motion of pairs of sp^2 C atoms

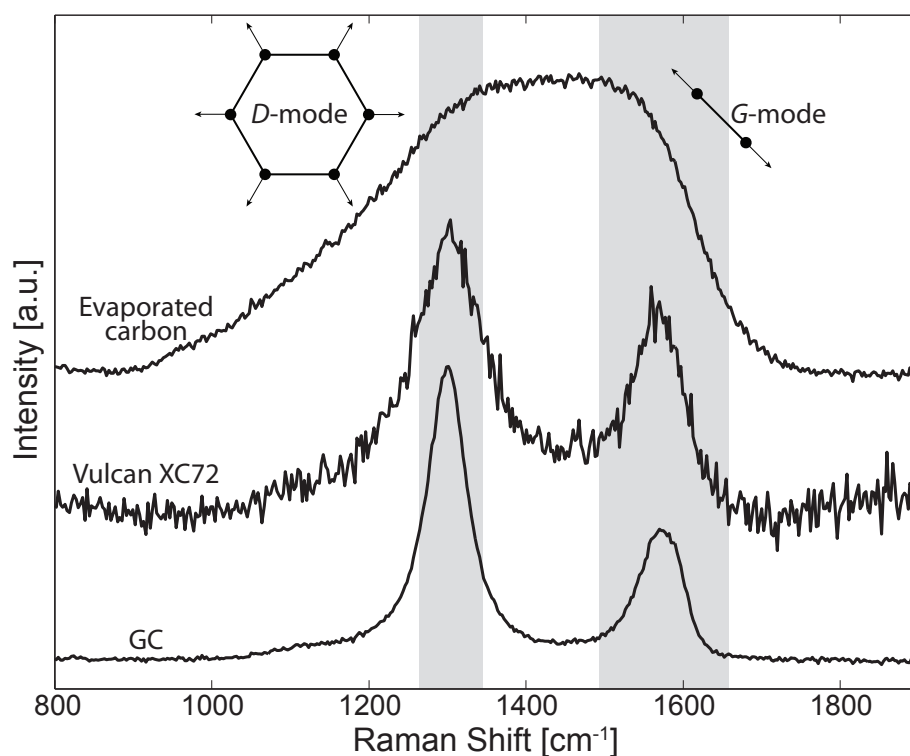


Figure 4.4: Raman spectra for a) evaporated carbon, b) Vulcan XC72 and c) glassy carbon. Shaded areas represent the intervals where the peak position for the *D* and *G* modes are usually found.

and is found in the range of $1500\text{--}1630\text{ cm}^{-1}$ [139]. In defect free and extended graphite or graphene, the *D* mode is forbidden, but it appears and grows with the number of defects. For completely amorphous carbon, there are no sixfold rings and consequently, no *D* peak is seen, but it appears and grows with the formation of nanocrystallites. Thus, the presence of a *D* peak indicates that the material has a nanocrystallinity [139]. By analyzing the relative intensities and peak positions of the *D* and *G* peaks it is possible to generate a “fingerprint” of the carbon structure. Generally, narrow and separated *D* and *G* peaks are associated with rather large crystallites, while more amorphous carbons with smaller crystallites display broader and often more or less overlapping peaks. In figure 4.4, two distinct and separated peaks at, 1310 and 1570 cm^{-1} are present for both GC and Vulcan. This indicates that these materials have relatively large crystallites and a small amount of truly amorphous carbon. On the evaporated carbon, the *D* and *G* peaks are largely overlapping. The spectrum could be fitted relatively well by two Gaussians, a larger peak at 1347 cm^{-1} and a smaller at 1536 cm^{-1} . This indicates that the crystallites in this material are smaller than those in Vulcan carbon. However, the fact that there is a large *D* peak indicates that the material has a substantial amount of sixfold crystalline carbon and should be a relatively good model material.

Table 4.1: Binding energies of evaporated material on GDL prior to fuel cell measurements with reference values for metallic form and likely oxides.

Material(core level electrons)	Peak position, binding energy [eV]			
	Measured	Reference values from [136]		
		Metallic	Oxide(s)	Compound
Pt(4f _{7/2})	71.2–71.7	71.0–71.2	73.8–74.2 74.6–75.0	PtO PtO ₂
Sn(3d _{5/2})	486.9	484.9–485.1	486.0–486.9 486.7	SnO SnO ₂
Ti(2p _{3/2})	458.6	453.7–454.1	455.1 458.7–459.2	TiO TiO ₂
Zr(3d _{5/2})	182.5	178.3–178.9	182.2	ZrO ₂
W(4f _{7/2})	35.8–36.0	31.4	32.8 35.8	WO ₂ WO ₃
Ta(4f _{7/2})	26.1	21.6–21.9	26.7	Ta ₂ O ₅

4.1.4 Metal Oxides

Most of the catalyst and support materials were evaporated from the elements in metallic form. However, the majority of non-noble metals will, to some extent, oxidize when exposed to air. Usually, the thickness of these native oxides is a few nm, which is around the dimensions used in this work. The evaporation chamber has a base pressure on the order of 10^{-6} mbar, with a small amount of oxygen and water vapor present, which can react with the materials already during deposition. Furthermore, even if the films are not completely oxidized after fabrication, it is likely that they become fully oxidized during the electrochemical measurements as the electric potential and presence of OH groups can efficiently oxidize metals.

XPS was the main tool for analyzing the chemical state of samples. As most of the XPS signal originates from the topmost layers, material below this will not be analyzed and might be in a different state. The state of the surface is the most important factor when considering interactions between the support and the Pt on top. On the other hand, the electrochemical measurements will be influenced by the spacer layers ability to conduct protons and electrons and these parameters depend on the state and structure of the complete layer. Table 4.1 shows the measured peak positions of selected core level electrons for a number of evaporated metals used in **papers I, III, and VIII**, as-prepared. Table 4.1 also shows reference values for the peak positions of the corresponding metal and oxide states of the materials together with the most probable oxide forms for each material.

The TiO₂ samples used in **paper I** were also analyzed by X-ray diffraction (XRD) and although the very thin layers (3–18 nm) made it difficult to get good signal, indications of crystalline TiO₂ in the anatase polymorph was observed. Anatase should also be the energetically favored phase for such thin layers of TiO₂ [140], while rutile is the most stable form for bulk materials [141].

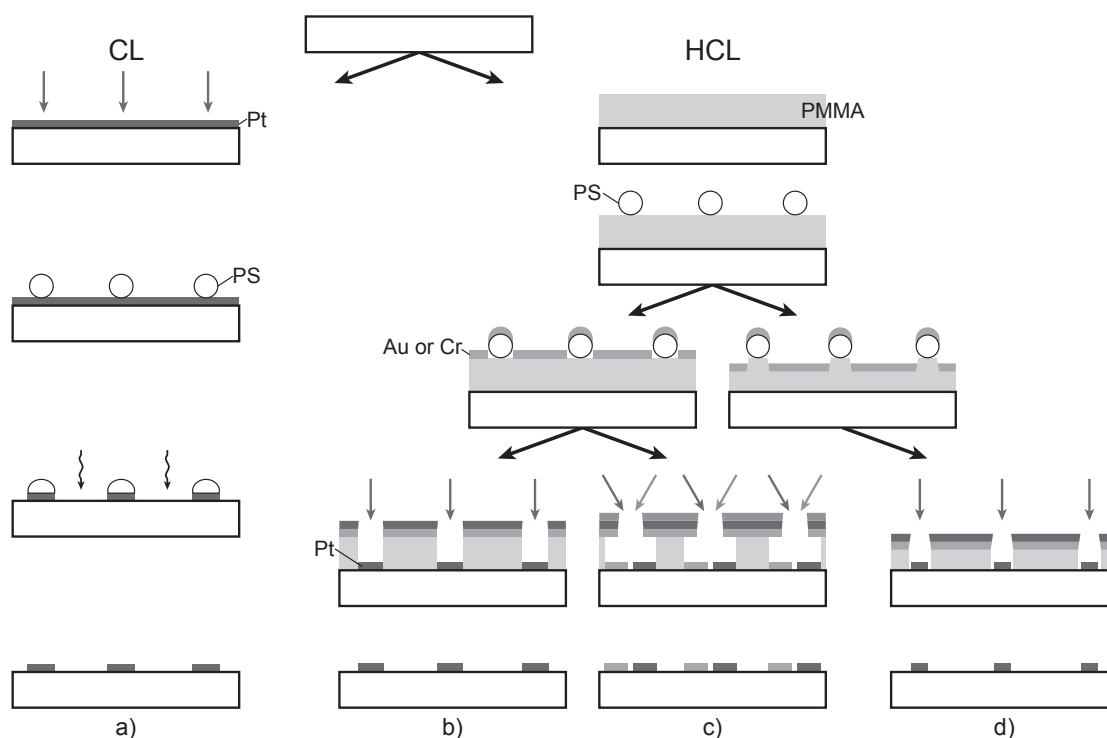


Figure 4.5: Schematic illustration of CL pathways. Route a) represents the standard CL method. b), c) and d) are versions of HCL, described in [117].

4.2 Nanostructured Electrodes

Nanostructured model electrodes were prepared on GC substrates by CL and HCL, and on Au or carbon covered Si-wafers by HCL. GC disks were first polished and chemically cleaned. Before catalyst deposition, all substrates were treated in O_2 plasma and, in some cases, Ar plasma [142]. The different methods used to fabricate nanostructured electrodes are schematically outlined in figure 4.5.

4.2.1 Colloidal Lithography

Route a) in figure 4.5 schematically illustrates the basic steps in the CL that was used in this work. First, a fully covering Pt film (typically 10–20 nm) was sputtered on a GC substrate. The surface of the Pt film was given a positive charge by adsorbing a triple layer precursor film, consisting of: *i*) 2 % poly(diallyldimethylammonium chloride) (PDDA, MW 200000–350000), *ii*) 2 % poly(sodium 4-styrenesulfonate) (PSS, MW 70000), and *iii*) 5 % aluminium chloride hydroxide (ACH). Each layer was pipetted on to the surface and adsorbed for 30 s before the sample was rinsed in Milli-Q water and blow-dried in N_2 . The thickness of the triple layer has been estimated to be around 1 nm [143]. Negatively charged polystyrene (PS) colloids diluted to less than 0.5 % in Milli-Q water was adsorbed on the surface for 1 min, followed by rinsing and drying as above. The negatively charged PS beads are attracted to the positively charged surface but repel other PS beads, creating a

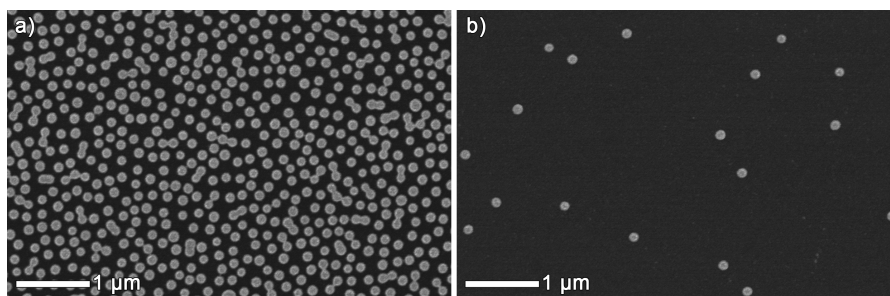


Figure 4.6: Pt nanodisks prepared by CL, a) high loaded and fairly regularly positioned disks (small variations in interparticle distance) while the, b) low loaded samples have a wide spread in interparticle distances.

sparse (i.e. far from close packed) colloidal layer. The separation of the colloids can be reduced by addition of salt, which screens the surface charges [144]. To avoid cup-shaped particles in the subsequent etching process (by redeposition of sputtered material), the PS spheres were partially melted on a hot-plate to relax them to hemispherical shape [145]. The particles were then used as etch masks during ion etching by directed Ar^+ ion sputtering. As this type of etching is selective to Pt over PS, the Pt situated under the PS beads is protected and the exposed Pt is etched away. The PS particles were then removed by UV-ozone etching, leaving only the Pt nanodisks on the surface.

Figure 4.6 shows SEM images of a) high loaded and b) low loaded ~ 140 nm Pt disks used in **paper II**. In the fabrication, PS beads of 110 nm were used and the reason for the prepared nanodisks having a larger size than this is due to the partial melting of the PS beads. The high loading was achieved by adding NaCl to 0.2 mM in a 0.5 % PS particle solution. The very low loading was achieved by using 0.001 % PS particle solutions. The adsorption time for the PS beads was held constant at 1 min. For the dilute PS solution, this implies that the PS spheres are not given enough time to form a steady state self-assembled pattern, i.e. the process was kinetically controlled. The minimum particle-particle distances are determined by the electrostatic interactions between the beads, but when the adsorption was aborted before saturation, a large spread in separations was obtained. In retrospect, it would have been preferred to use the fabrication scheme developed in **paper VI** (shown in route d) in figure 4.5) to fabricate these very low loaded samples.

An important fact, discussed in **paper II** and treated in more detail in **paper X**, is the presence of Pt contaminations around the nanostructures. In the Pt etching process, Ar^+ ions are accelerated and bombarding the surface. Most of the Pt that is hit by the Ar plasma is expelled out in the vacuum and away from the sample. However, a substantial amount of the metal is also pushed laterally along the surface or further into the material, so-called forward sputtering. Even if the samples were over-etched by about 10 nm into the GC substrate, there were still traces of Pt left between the nanodisks. This unwanted Pt was present at a rather small concentration and should not cause any major problems for the high loaded samples, but for the very low loaded samples (as those in figure 4.6b) the relative

amount was significant and likely to interfere with the electrochemical results. An effective way to overcome contaminations of unwanted Pt is to employ the HCL routine to fabricate the Pt nanodisks, instead of the CL.

4.2.2 Hole-Mask Colloidal Lithography

The main difference between CL and HCL is that a sacrificial masking layer (the hole-mask) is employed in the latter case and the material constituting the nanoparticles is only deposited on the unmasked areas of the substrate. Route b) in figure 4.5 schematically illustrates the basic steps in HCL to create nanodisks. The pathway to create nanodisk pairs of different (or the same) material is outlined in route c) in figure 4.5. Both routes b) and c) are examples of pathways outlined in [117]. In the initial step, a sacrificial polymer film, poly(methyl methacrylate) (PMMA), 2–4 %, diluted in anisole, was spincoated onto the surfaces for 1 min at 2000–6000 rpm. The thickness of the resulting film is governed by the PMMA concentration and the rotation rate of the spinner, typically between 50–250 nm. The PMMA was cured on a hot plate at 170 °C for 10 min to evaporate the solvent and subsequently treated in an O₂ plasma (5 s, 50 W, 250 mTorr) to increase the hydrophilicity. The activated PMMA was given a positive charge by adsorbing a single layer of 0.2 % PDDA before adsorption of PS beads in the same manner as for the CL process. An O₂ plasma resistant film of Au and/or Cr (about 20 nm), which later functioned as the hole-mask, was evaporated onto the nanospheres + polymer film. The PS beads were then lifted off using tape stripping, leaving the PMMA film covered by a hole-mask with holes where the nanospheres were situated. O₂ plasma was used to etch the exposed polymer (i.e. the PMMA in the holes) down to the substrate. For the fabrication of nanodisk samples of a single material (Pt, figure 4.5b), the next step was evaporation of Pt through the hole-mask. In order to create the particle pairs (figure 4.5c), a large undercut is needed in the PMMA film. This is usually created by a longer O₂ plasma step [117], but as carbon was used as substrates in this work, that method could not be used. Instead, the samples were immersed in 100 % acetic acid to create an under-etch, approximately three times larger than the holes in the overlaying Au film. The materials were then deposited from opposite angles from the substrate surface normal (i.e. 180° difference in azimuthal angle but same polar angle). The separation (or overlap) of the paired disks is determined by the thickness of the PMMA film and the polar angle of evaporation. Finally, the hole-mask was lifted off in acetone, which dissolves the PMMA and removes the hole-mask, leaving only the nanodisks on the surface.

The HCL fabrication routine presents several advantages as compared to the standard CL method. The problem with forward sputtering is eliminated and the PS beads are always adsorbed on the same material. The fact that a single layer of PDDA was sufficient to create a good surface charge before PS adsorption rendered the ASH solution redundant, which is beneficial as it contains Al that can contaminate the samples. Furthermore, the HCL method enables fabrication of a variety of structures, which cannot be produced with standard CL [117].

Figure 4.7 shows three different samples of Pt–Ru particle pairs used in **paper**

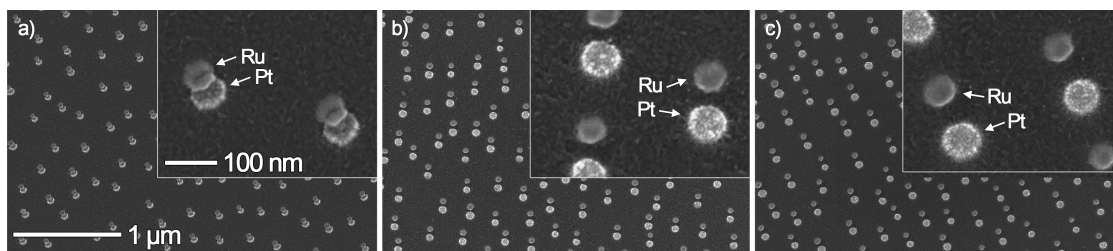


Figure 4.7: Pt–Ru particle pair arrays of a) overlapping by about 25 nm, b) separated by 25 or c) 50 nm.

VII. The separation of the disks within the pairs was changed from a) overlapping by about 25 nm, to b) fully separated by 25 or c) 50 nm. The Pt and Ru disks were fabricated by deposition at an angle of $\pm 15^\circ$ from the substrate surface normal and the separation or overlap was governed by the height of the PMMA hole-mask. The PMMA thickness was approximately 70, 180, and 240 nm for the samples shown in figures 4.7a–c, respectively. The Pt disks are slightly larger than the Ru disks, which is a consequence of the fact that Pt was evaporated first and during evaporation, some Pt deposited on the sides of the holes and decreased their diameter. The relative Pt:Ru surface area or atomic fractions were estimated from SEM images and from spectroscopic analysis with XPS and EDX. The results from the three methods were in good agreement and showed that overlapping pairs had about 55 % Pt (and 45 % Ru), while the separated samples had about 60 % Pt.

4.2.3 Modified HCL

Although HCL holds a number of advantages over conventional methods to fabricate nanostructured model electrodes, modifications may extend its application range even further. In **paper VI** it was shown that Pt could be electroplated through a polymer hole-mask, replacing the evaporation step that is used traditionally (second to last step in figure 4.5b). This offers several advantages, including reduced cost, material utilization close 100 % (as compared to less than 0.1 % for typical evaporation), as well as the ability to deposit materials that cannot readily be produced by evaporation [146]. Since there is no deposition on the mask in this case, it is possible to create particles with higher aspect ratio (height/diameter). Furthermore, the electric control in the electroplating offers both control over and ability to monitor the amount of material deposited, which can be difficult with some PVD techniques. Figure 4.8 shows Pt disks electroplated through a PMMA mask onto Au covered Si-wafers. A constant current density of 0.55 mA cm^{-2} was used for three different durations, a) 8, b) 30, and c) 180 s. Based on the charges passed during the experiment, the (average) thicknesses of the deposited Pt were estimated to be 7, 26, and 155 nm, respectively.

The difficulty of producing well ordered arrays of very low loadings was encountered in **paper II** and described above. In **paper VI**, a method to overcome this, and also to produce nanoparticles with very small sizes (much smaller than

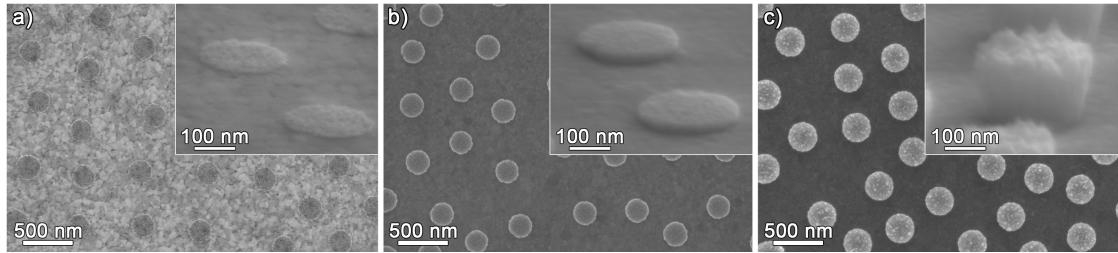


Figure 4.8: Pt nanodisks electroplated through a HCL mask onto Au support with approximate nanodisk heights of a) 7, b) 26, and c) 155 nm.

the colloid particles used to define the mask) was presented. It was achieved by treating the sample with O_2 plasma after the adsorption of PS beads. This shrinks the PS spheres and causes an under-etch in the PMMA film so that the PS beads are supported on PMMA pillars. The subsequent evaporation of the Au hole-mask was performed at two opposite angles of 45° from the surface normal so that the holes in the Au film were defined by the smaller PMMA pillars, rather than by the PS beads. The rest of the fabrication followed the standard HCL procedure. Figure 4.9 shows a TEM image of Pt nanoparticles fabricated using this method to shrink the holes in the mask. Nanospheres with a diameter of 110 nm were used in the fabrication (their size is outlined in the figure) and the diameter of the Pt nanoparticles was found to be about 45 nm. As a consequence, the particle coverage was reduced to about 1.5 %, compared to about 10 % for the original nanospheres, but with preserved spatial order, i.e. without changing center of gravity particle positions.

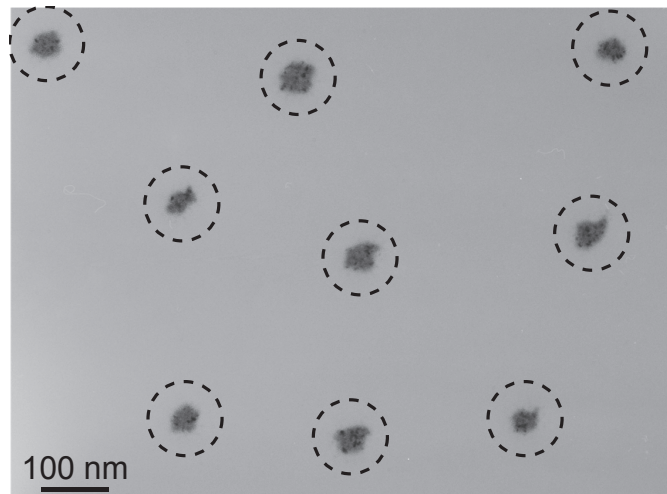


Figure 4.9: TEM image of Pt nanoparticles prepared by shrinking of the holes in the HCL mask. Outlines of the PS particle diameter are added as dashed circles.

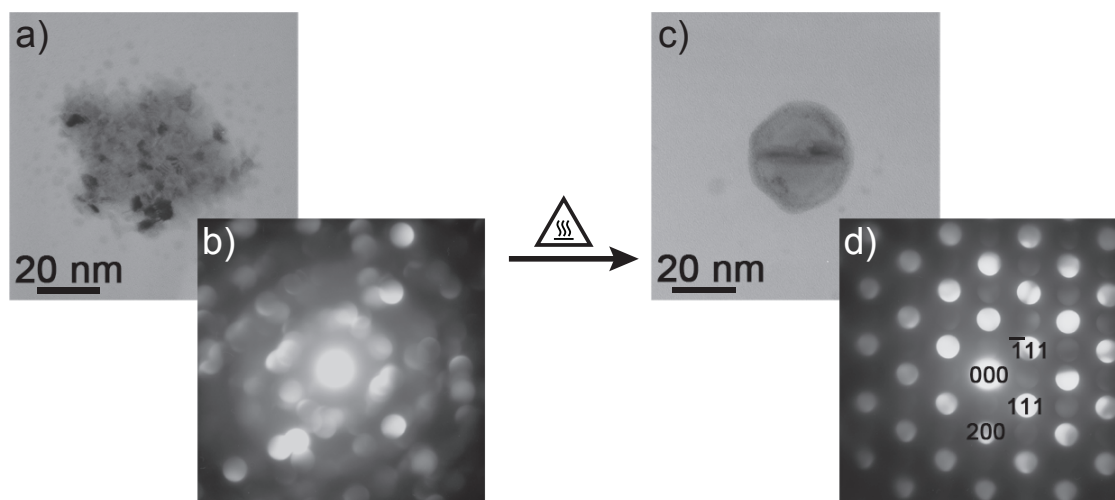


Figure 4.10: Pt nanoparticles prepared by shrinking the holes in the HCL mask. a) and b) shows TEM image and CBED pattern, respectively, from a single particle, as-prepared. c) and d) shows corresponding images after annealing.

4.2.4 Annealing of Pt Nanostructures

Depositing Pt with non-equilibrium processes, such as evaporation or electrodeposition produces polycrystalline Pt, which exhibit lattice compression, microstrains, and intergrain boundaries. The amounts of these depend on the process and operating conditions and affect the crystallite sizes and the roughness. These differences will affect the catalytic behavior of the material and can complicate comparisons between differently prepared samples [147, 148]. By annealing of the nanostructures, these differences and defects can be reduced or eliminated, as single crystal nanoparticles are formed. The Pt nanoparticles showed in figure 4.9 were annealed in Ar atmosphere at 1023 K for 3 min. Figure 4.10 shows high magnification TEM images together with convergent beam electron diffraction (CBED) patterns from individual Pt particles before (a and b) and after the annealing (c and d). The polycrystallinity of the as-prepared nanoparticles is easily seen from the CBED pattern and agrees with the contrast image, which also shows that the particles had a somewhat irregular periphery (due to the shrinking of the mask as described above). During annealing, the diameter of the nanoparticles was reduced from about 45 to 30 nm and visible crystal facets/edges were formed. The particle shown in figure 4.10c has, what seems to be one stacking fault running through the particle. The CBED pattern obtained after annealing could be indexed and shows that the Pt nanoparticles were successfully transformed to single crystal particles.

A similar treatment was also applied to slightly larger Pt particles prepared by electroplating through a hole-mask on evaporated carbon support. In this case, the annealing was carried out in a flow reactor at 1023 K with 4 % H_2 in Ar flowing over the sample. The H_2 was added in order to react any O_2 impurities that could otherwise oxidize the carbon support. The result from the annealing is shown in

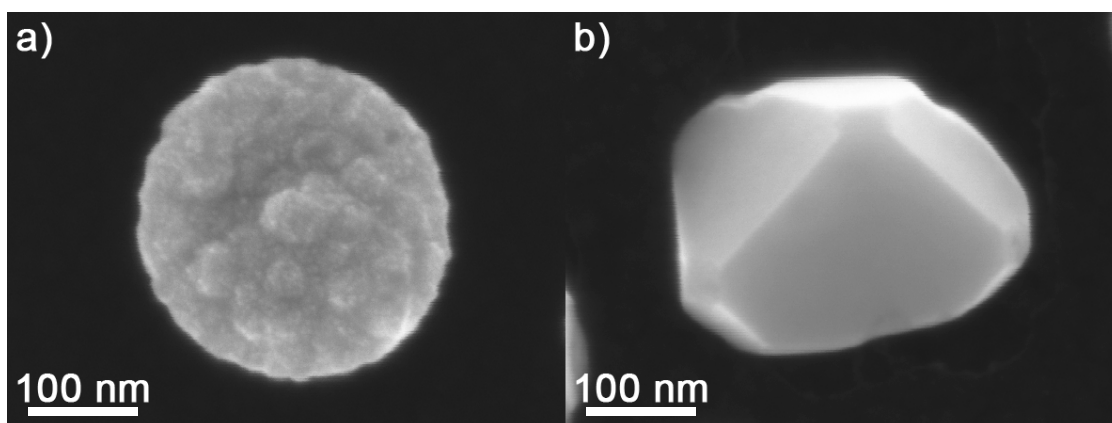


Figure 4.11: Pt nanoparticles prepared by electroplating through a HCL mask onto carbon support. a) as-prepared and b) after annealing.

figure 4.11 with SEM images a) before and b) after. Also in this setup, more or less perfect single crystals were obtained. The crystal facets are clearly visible and shows that the crystals were predominantly terminated by $\{111\}$ facets and a small amount of $\{100\}$ planes. On a few particles, a small fraction of the $\{110\}$ plane was also exposed. This is likely to be close to the Wulff shape of these particles.

By changing the atmosphere during annealing, it might even be possible to control which facets are formed and their relative amount, since adsorbates change the relative surface energies of different facets [149]. It has also been shown that the annealing rate towards the Wulff shape can be accelerated by running a catalytic reaction on the Pt particles [150]. Being able to control the crystallinity of the nanoparticles is of great importance in preparation of well characterized nanostructured model systems; it increases the reproducibility of the sample fabrication and it enables mechanistic studies, where effects related to different crystal facets and edges can be studied/accounted for.

PEM Fuel Cell Reactions

In this chapter, the measurement setups used to evaluate model electrodes are described and the results from the electrochemical experiments are presented and discussed in terms of the specific reactions that were studied.

5.1 Electrochemical Measurement Setups

The electrochemical measurements were mainly performed at KTH and the University of Ulm. The specific features of the setups and the measurements employed there will be addressed below. In addition, two electrochemical measurement setups (a flow cell for EQCM measurements and an automated single cell fuel cell setup) were assembled at Chalmers and will be described in more detail.

5.1.1 Liquid Half-Cells

Standard three-electrode glass half-cells were used as a compliment to fuel cell studies at KTH in **papers V and VIII** as well as in the electroplating and electrochemical characterization at Chalmers in **paper VI**. Pt wire or mesh was used as CE and in most cases a Hg/Hg₂SO₄ as RE. The electrolyte used was 0.5 M H₂SO₄, bubbled with N₂ to remove dissolved O₂ from the air.

For the measurements presented in **paper IV**, a flow-cell with the ability to perform simultaneous electrochemical and QCM-D measurements was developed. (D is in this context, dissipation, which measures the damping of the QCM-D sensor oscillation and is a measure of the viscoelastic properties of the sample–electrolyte interface [151, 152].) The cell was designed in collaboration with Q-Sense AB and was able to work with the hardware and software of Q-Sense’s commercial QCM-D measurement platform. Figure 5.1 shows photographs of the cell and a sample. A Pt-black covered Pt foil positioned in the ceiling of the chamber and a Hg/Hg₂SO₄ electrode in contact with the electrolyte inlet served as CE and RE, respectively. The samples were supported on AT-cut quartz crystals and functioned both as the top electrode for the QCM-D and as WE for the electrochemical measurements. The QCM-D measurement was running in parallel with the electrochemical measurements, constantly monitoring the frequency and dissipation changes on the electrode caused, mainly, by changes induced by electrochemical experiments. A

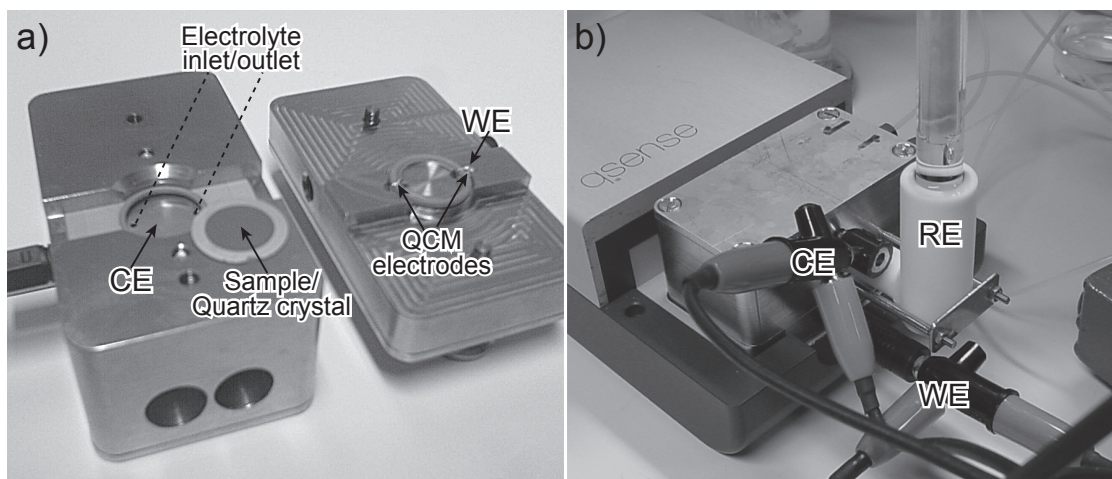


Figure 5.1: Photographs of the EQCM-D cell developed at Chalmers. a) shows the cell when opened, with a quartz crystal placed on top. b) shows the cell and the connections when in operation.

crucial point in analyzing the results was to couple the timescales for the individual measurements. For example, CV was performed at a scan rate of 50 mV s^{-1} and in order to plot the frequency (or mass) change of the QCM-D measurement vs. electrode potential, an accuracy better than $\pm 50 \text{ ms}$ was reckoned as required. This was realized by generating a timestamp and sending a digital trigger from the QCM software (courtesy of Q-Sense), which could be detected by the potentiostat (Gamry REF-600). The open source software controlling the potentiostat (Gamry Framework) allowed for programming of the potentiostat to start measuring when the trigger was received. This synchronization was estimated to be accurate within 8 ms.

Two different flow cells (but of similar structure) were used for the electrochemical evaluation at the University of Ulm. Circular GC disks were mounted upside down in a small compartment with the electrolyte inlet positioned below the center of the sample. The electrolyte flowed radially to four outlet channels and into a second compartment. In the first setup, this second compartment had a porous membrane behind which, a vacuum system with a MS was situated. This dual thin-layer cell for DEMS measurements has been described in detail previously [124] and was used for a few of the measurements in **paper VII**. In the other setup, the second compartment held an additional WE which was used for detection of electrochemically active species in the electrolyte [125]. This setup was used in **paper II** for detection of H_2O_2 . By dissolving reactive molecules in the electrolyte, these setups were used to analyze a number of different reactions, including ORR, HOR, and CO oxidation.

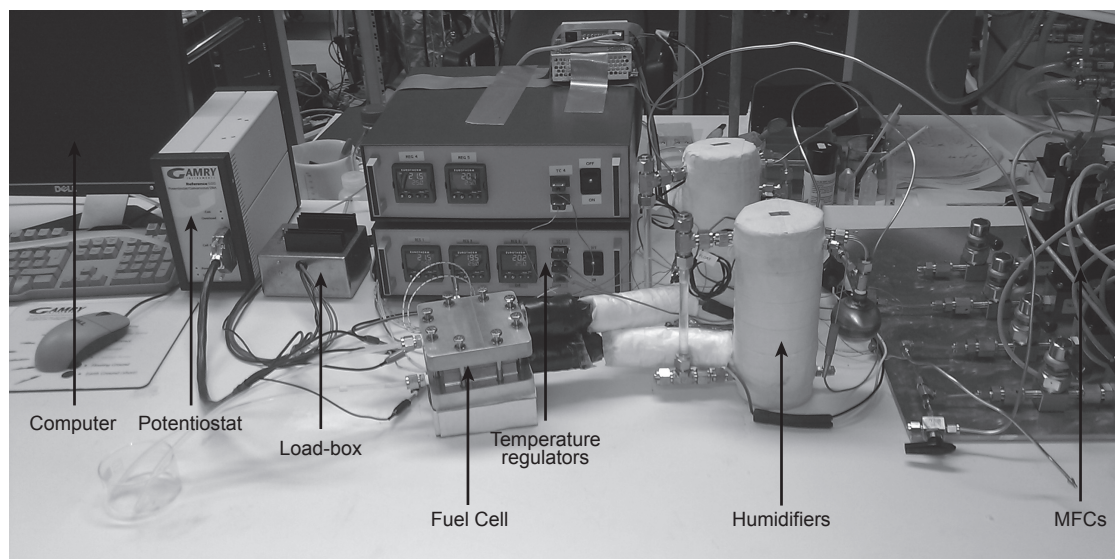


Figure 5.2: Photograph of the single cell fuel cell setup assembled at Chalmers.

5.1.2 Single Cell Fuel Cell

A complete single cell fuel cell test station including, a 5 cm² active area fuel cell (Fuel Cell Technologies), gas humidifiers (Fuel Cell Technologies), mass flow controllers (MFCs, Brooks), temperature regulators (Eurotherm), a potentiostat (Gamry REF-600), and a home-built passive load-box was assembled at Chalmers. The setup is shown in figure 5.2. The components were connected to a computer and everything except the potentiostat was directly controlled via a LabVIEW interface. The scripting possibilities of the potentiostat software (Gamry Framework) gave the ability to communicate with the LabVIEW program and allowed for fully automated measurement sequences, including a range of different electrochemical experiments, switching of gases and flow rates, and changing of temperatures and relative humidity. Also, the load-box could be activated via the software, which made it possible to measure currents up to 10 A (the potentiostat used here can only measure below 0.6 A). This setup was used in a study on fuel cell degradation, which is in progress.

The single cell fuel cell at KTH, used in **papers I, III, V, and VIII** is an in-house constructed cell, which has been described in detail elsewhere [153]. A special feature of this cell is that the clamping pressure over the electrodes is controlled separately from the compression of the fuel cell body which seals to the membrane. It has a circular active area of 6 cm².

5.2 Fundamental Electrochemical Reactions

The detailed structural and compositional characterization described in chapter 4 enabled the subsequent electrochemical results to be evaluated in respect to the model electrode structure. As the different model electrodes have diverse properties

and the systems used to evaluate them are suited for specific studies, the questions that could be answered were different in the different systems, even when evaluating the same reaction. However, the ability to study multiple aspects of a reaction gives synergetic answers and increases the understanding of the system. The potentials referred to in the following sections are quoted vs. that of the RHE.

5.2.1 Oxygen Reduction Reaction

The ORR is the most critical fuel cell reaction to improve, as most of the efficiency losses in the fuel cell is related to this reaction. With the use of nanostructured electrodes it is possible to examine the role of nanoscale mass transport and re-deposition processes which can give information about the reaction mechanism. The electrodes used in **paper II** ranged from large Pt nanodisks with high loading to small disks with a very low loading (two of these are shown in figure 4.6). The ORR was evaluated in O₂ saturated H₂SO₄ by scanning the potential from open circuit potential (OCP) to the onset of HER at a rate of 10 mV s⁻¹. Figure 5.3 shows a) the ORR activity for the different nanostructured electrodes and a polycrystalline reference sample and b) the calculated H₂O₂ yield (calculated from the currents generated on the second WE biased at 1.2 V). The legend gives the total Pt coverages for the samples. There are only minor differences in ORR current between the electrodes, which can be explained by the rather slow mass transport of O₂ in the electrolyte. At roughly the same potential as the ORR starts to increase (~0.8 V), the H₂O₂ yield increases. Interestingly, the sample with the lowest Pt coverage shows the highest H₂O₂ yield. In fact, the H₂O₂ yield follows the same order as the Pt coverage. The reason for this effect is that the formed H₂O₂ can desorb from the Pt surface and diffuse in the near surface region before it is transported out in the flowing electrolyte. For the high loaded samples, the probability for a H₂O₂ molecule diffusing close to the surface to hit another Pt particle and be further reduced to H₂O is higher than on the low loaded samples. These results prove that the ORR, at least to some extent, proceeds via the formation of H₂O₂ and that H₂O₂ can desorb from Pt. This is essential for fuel cell performance as there is an ambition to reduce the Pt loading in the electrodes, which then can lead to a more incomplete ORR and, thus, a lower efficiency. Moreover, the formation of H₂O₂ in the electrode can induce an increased degradation of the carbon support, ionomer, and/or membrane since H₂O₂ is very reactive [154].

The ORR was also studied in fuel cell setup on thin-film electrodes deposited on both Nafion and GDL. In many of these studies, Pt was combined with metal oxides in order to examine possible Pt-support interactions. From the samples on Nafion in **paper I**, it was seen that adding a spacer layer of TiO₂ between the Nafion and Pt increased the ORR activity per geometric area and amount of Pt. However, this effect could be explained simply from the fact that the Pt on TiO₂ sample had a higher ECSA of Pt. This could in turn be related to a higher dispersion of Pt when it was deposited on TiO₂ as opposed to directly on the Nafion membrane. Even though this result was an effect of the model system and not related to the intrinsic ORR activity, it may be possible to use these findings to improve the Pt

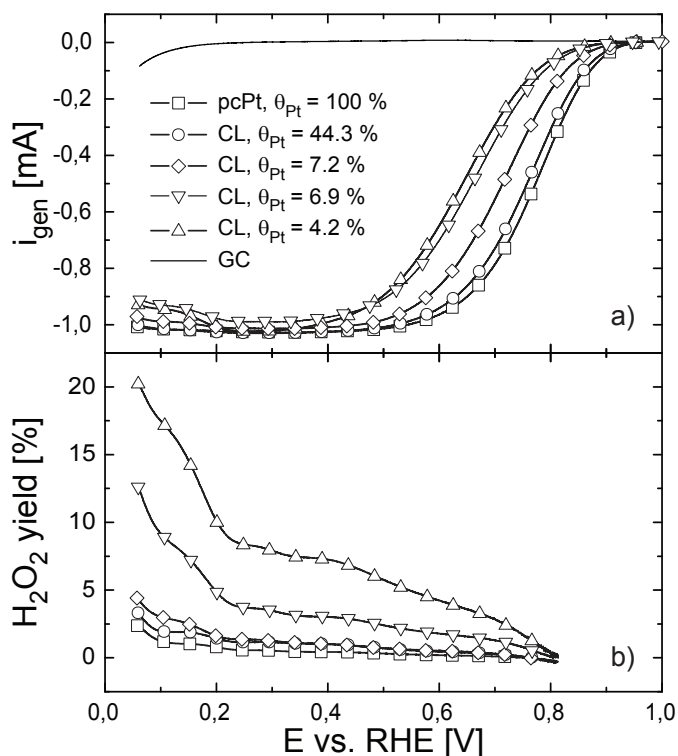


Figure 5.3: ORR on nanostructured electrodes of varying Pt coverage, Θ_{Pt} , prepared by CL. a) shows the ORR currents and b) shows the calculated H_2O_2 yield.

utilization in fuel cell electrodes.

For samples deposited on GDL, one combination of Pt and metal oxide showed higher ORR currents than sole Pt, namely Pt on SnO_x . Also here, most of the effect could be explained by an increased Pt surface area when Pt was deposited on SnO_x as opposed to on GDL. For samples of Pt on TiO_x , WO_x , ZrO_x , and TaO_x , the ORR activity was lower than that of Pt. These results were presented in **paper III** where also the durability of the electrodes was investigated by applying an accelerated aging consisting of 1000 cycles between 0.6–1.2 V. This scheme simulates start/stop cycling and was employed to, mainly, degrade Pt. The ORR activity and the ECSA of the samples were measured before and after. An interesting observation was seen by comparing the loss of surface area with the decrease in ORR activity. For the sole Pt electrode, the ECSA decreased by 72 %, while the ORR current at 0.85 V only decreased by 50 %. This indicates that the Pt left in the electrode after the degradation had a higher specific ORR activity than the initial value. Possible explanations for this can be that during degradation, Pt was dissolved and redistributed within the electrode to more favorable positions, that structural changes in the electrode increased the transport of reactants, or that larger Pt particles were formed as a result of Ostwald ripening. Larger Pt particles exhibit higher specific ORR activity [88]. Unfortunately, these model electrodes could not be characterized after the fuel cell measurements as the electrodes had been hot-pressed onto Nafion membranes and were not possible to detach.

5.2.2 Hydrogen Oxidation Reaction

Since HOR on Pt is an extremely fast reaction, it is difficult to study the intrinsic kinetics and the measured currents are often influenced by mass transport limitations. Although this reaction gives rise to far less problems in the fuel cell than the ORR, it would be of great value to decrease the Pt loading also on the anode side. An increased understanding of the kinetics and the mechanism of HOR can enable this. Model electrodes with small amounts of Pt evaporated on GDL has several advantages for studying HOR. This electrode can be measured in a fuel cell where H₂ gas is fed directly to the catalyst, i.e. not dissolved in liquid. The low loading of the electrode implies low currents and consequently, low H₂ consumption, which decreases concentration gradients and minimizes mass transport losses. In addition, these electrodes does not contain any ionomer, which otherwise may induce additional mass transport limitations. In **paper V**, three model electrodes with 1.5, 3 and 6 nm of evaporated Pt were prepared. The ECSA determined from CV in both liquid electrolyte and in fuel cell increased with amount of Pt. For the half-cell measurements, the values agreed well with the SEM images shown in figure 4.2, whereas the values were significantly smaller for the fuel cell measurements since only a fraction of the Pt was active here, as described in section 4.1. Although the excess Pt in the electrode imposes an uncertainty regarding the amount of Pt available for the HOR, it is unlikely that Pt not active in the CV would be active in the HOR. Moreover, the ECSA was constant during the measurements and reproducible, as determined from double samples. The measured HOR currents per unit area (geometric) measured from the three electrodes are shown in figure 5.4a. The electrodes reach different limiting currents, highest for the highest loaded electrode and vice versa. Since the Pt is situated on the same exposed area on all electrodes, this fact further supports the claim that the currents are not diffusion controlled. By assuming Fick diffusion and literature values for H₂ diffusion in GDL material [155], the concentration profile in the GDL could be estimated. Using the limiting current density for the 6 nm Pt electrode and the operational parameters during the measurements, it was concluded that the H₂ concentration at the MPL–Nafion interface, where the Pt was situated, should differ by less than 1 % from that in the gas channel.

The HOR currents shown in figure 5.4b were iR corrected with values from impedance spectroscopy to remove charge transfer resistance effects and they are normalized to the ECSA of Pt (determined from CV). The curves from the three electrodes has almost identical shape and they reach the same limiting current density, about 1.6 A cm⁻², which is significantly higher than what has previously been presented [72]. With the reasons given above, it is likely that this is the current for the kinetically limited situation. The origin of the current dip, at about 0.15 V on all samples, has not been clarified but it might be related to small variations in the interactions between Pt, Nafion, and water. The lack of increase in the current density at higher potentials rules out the possibility of the Heyrovsky–Volmer mechanism being active at higher potentials, which has been suggested [71]. Instead, it is proposed that the Tafel–Volmer mechanism is the only

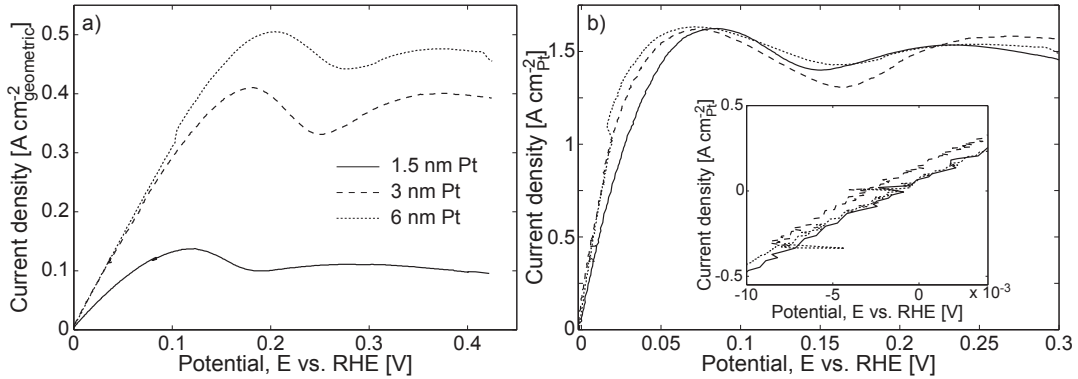


Figure 5.4: HOR measured on evaporated Pt on GDL. a) current density per geometric area and b) *iR*-corrected current density per ECSA of Pt. The inset in b) shows the linear region around *E*⁰.

operational pathway for HOR in these measurements, with the Tafel step as rate determining when the limiting current is reached. The limiting current is interesting from a fundamental point of view and can be compared to the sticking probability and turn over frequency, often referred to in gas phase catalysis [156]. From a practical fuel cell perspective, however, it is desirable to polarize the electrode as little as possible, which implies that the limiting current is usually not reached. For this purpose, it is more relevant to derive the exchange current density, *i*₀. An expression for *i*₀ was obtained from the rate expressions for the Tafel–Volmer mechanism, assuming negligible mass transport limitations and the Volmer step being at equilibrium

$$i = \frac{i_0 \frac{2F\eta}{RT}}{1 + \frac{i_0}{i_{diff}}} \quad (5.1)$$

where *i*_{diff} is the diffusion limiting current density and was assumed to be much larger than *i*₀ (agreeing with the diffusivity calculation mentioned above, causing the denominator to approach one). This equation is essentially the same as what has been derived before [68,69] and it was used to estimate *i*₀ from the slopes of the curves shown in figure 5.4b, close to the equilibrium potential, as indicated in the inset. An *i*₀ of around 770 mA cm⁻² was determined for all electrodes, which is higher, but on the same order as previously presented values [73]. It is important to realize that this value is highly dependent on the assumed mechanism and the assumptions made when deriving the expressions, which means that it is difficult to compare the actual numbers of *i*₀ from the literature. However, the results imply that it should be possible to decrease the Pt loading in anode catalysts even further without imposing too high voltage losses.

The HOR was also used to illustrate the ideas about diffusion above arrays of low coverage nanostructures in half-cell. On a flat Pt surface, the diffusion profile perpendicular to the surface is uniform over the sample (i.e. planar diffusion), reaching zero concentration at the surface. On low loaded samples, there is instead

a hemispherical diffusion zone around each nanodisk (i.e. hemispherical diffusion) and thus the mass transport to an isolated disk is higher than the corresponding transport to a similar sized area on an extended surface. This was shown in **paper VII** where a polycrystalline Pt surface obtained a mass transport limited HOR current that was 1.3 times higher than that of a nanostructured Pt electrode with a Pt coverage of merely 7.5 % at the highest flow rate used. This is an important property of nanostructured samples, which can be utilized to decouple mass transport effects in electrochemical reactions.

5.2.3 Carbon Monoxide Oxidation

Anode catalysts fed with H_2 from reformat must be able withstand poisoning from traces of CO present in these fuels. This is often achieved by incorporating Ru in the electrode. However, the mechanism of the enhanced CO tolerance is not completely known, which hinders optimization of Pt–Ru catalysts. The samples shown in figure 4.7 were designed for this purpose and their CO_{ad} oxidation behavior was analyzed in **paper VII**. CO was first adsorbed at a potential of 60 mV in CO saturated H_2SO_4 . Then the cell was rinsed with CO-free electrolyte before the potential was scanned positive and the adsorbed CO was oxidized. Surprisingly, a considerable and almost identical CO oxidation activity was observed between 0.5 and 0.7 V for all Pt–Ru samples, where reference samples of single metallic Pt and Ru showed little activity. This increased activity must stem from Pt–Ru interactions. If the phases are truly separated (which they were before the electrochemical measurements), the results can be explained by the bifunctional mechanism only if the oxygenated species produced on Ru are extremely mobile and can spill over to the substrate and move to the Pt disks. Such an explanation seems unlikely and should have a clear dependence on the separation between the disks, which was not observed. A more probable explanation is that dissolved Ru, created during exposure to high potentials might have deposited on the Pt, resulting in partly Ru decorated Pt disks. It has been shown that deposition of small amounts of Ru, in the range of fractions of a monolayer, on a Pt surface can shift the onset of CO oxidation to lower potentials, similar to that of Pt–Ru alloys [157, 158]. Although this study could not produce explicit results regarding the mechanism of CO oxidation in Pt–Ru systems, the applied methodology showed great promise and it is likely that this type of model electrodes will be able to answer some of these questions. However, the likely explanation that dissolved Ru can deposit on Pt, might explain some of the previous results on this matter [159].

CO_{ad} oxidation was also performed in fuel cell setup on WO_x supported Pt deposited on GDL. The results were presented in **paper VIII** and showed that the onset potential for CO oxidation was shifted to lower potentials than for Pt, indicating that also WO_x can increase the CO tolerance of an anode electrode. Compared to Ru, WO_x is both cheaper and more stable in the fuel cell environment. The mechanism for the reduced stability of the adsorbed CO was not investigated in this work, but it has been suggested that, similar to Ru, WO_x can provide oxygenated surface species at lower potentials which can spill over to the Pt [160, 161].

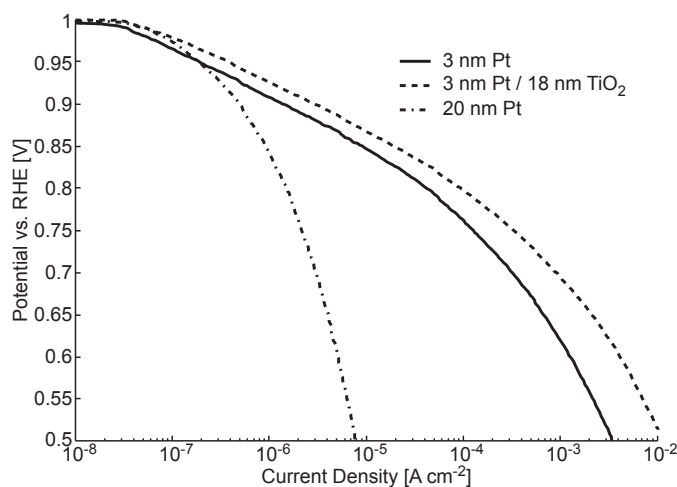


Figure 5.5: Polarization plot in O_2 for 3 nm Pt, 3 nm Pt on 18 nm of TiO_2 , and 20 nm Pt, all deposited on Nafion.

5.2.4 Proton Conduction

Proton conduction is an important process both in the membrane and in the electrode of fuel cells. It is also a key parameter for evaluation of the model electrodes in fuel cell setups. For the samples where Pt was deposited on Nafion membranes, with a metal oxide spacer layer, protons must be able to move through the metal oxide to reach the Pt. In **paper I**, it was shown that for Pt on TiO_2 , this was not an issue and no change in cell resistance was observed as compared to samples without the spacer layer. This was in contrast to ZrO_2 and Ta_2O_5 where only 1.5 nm of the oxides was sufficient to increase the cell resistance and effectively diminish the ORR activity. This was despite the fact that all metal oxide films had a similar structure, as determined by TEM. Figure 5.5 shows a comparison between the ORR activity of 3 nm Pt on 18 nm TiO_2 , a 20 nm Pt film, and a 3 nm Pt reference sample. The thick Pt film effectively blocked the proton transport and rendered a very low activity whereas both the Pt and Pt on TiO_2 showed high activity. This indicates that proton conduction is not limiting. The observed proton conductivity cannot be explained by protons moving in the cracks formed in the TiO_2 layer as a consequence of membrane swelling. This conclusion is based on the fact that SEM images revealed a very similar morphology of the thick TiO_2 and Pt films after the fuel cell measurements. Protons have been suggested to move through the TiO_2 bulk [162], but most likely, the high conductivities stem from the Grotthuss mechanism, where protons form H_3O^+ ions and jump between neighboring water molecules [163]. The latter mechanism requires hydrated pores in the TiO_2 [164]. As TiO_2 is a cheap and abundant material that is stable in the fuel cell environment, these results open up for a number of possible usages of TiO_2 in fuel cell MEAs.

Proton conduction of metal oxides was also found to play an important role in the model electrodes deposited on GDL. In **papers III and VIII**, it was seen that a 3 nm layer of TiO_x or WO_x between the GDL and Pt did not change the ECSA

compared to having Pt directly on the GDL. This indicates that Pt forms a similar structure on the metal oxides and GDL, which was also confirmed by SEM images. However, when using thicker films of metal oxides, 10 nm and more, a significant increase in ECSA was observed. Mainly, two discrete levels of ECSA was seen, one for thinner films of 3 nm and below, and one for thicker films of 10 nm and above. From SEM analysis, no indications were found for a changed Pt structure for the thicker films. A likely explanation is that TiO_x and WO_x , which are known to be able to conduct protons [165], can enable a larger fraction of the Pt particles to have proton contact. For the thin metal oxide films, it is likely that the layers were not continuous (as the GDL is porous) and, thus, lateral proton conduction was not possible.

5.3 Degradation

Dissolution of Pt and corrosion of the carbon support are the main reasons for the performance decrease observed for PEMFCs. An increased understanding of these processes can enable the development of more stable electrodes and be used to design fuel cell operating parameters which minimize degradation.

5.3.1 Pt Dissolution

Unfortunately, Pt is not as stable in the fuel cell environment as desired and dissolution of Pt causes a loss of ECSA. By using the EQCM-D setup, described in section 5.1.1, Pt dissolution was studied in **paper IV** by observing the frequency change of a Pt covered quartz crystal upon cyclic degradation experiments between 0.02–1.4 V at 50 mV s⁻¹ in 0.5 M H₂SO₄. The frequency shifts were converted to mass changes of the electrode and figure 5.6 shows the mass change of a 20 nm Pt film deposited on carbon during 10 cycles measured at 70 °C, with 5 min at OCP before and after the cycles. During the cycles, the mass increases and decreases reversibly due to Pt oxide formation and reduction [166]. However, there is also a small irreversible mass loss for each cycle that is difficult to observe for only one cycle, but during 10 cycles it is clearly seen and it is more or less linear with the number of cycles. The mass loss per cycle was calculated to be 2.8 ng cm⁻² cycle⁻¹ based on the ECSA of Pt, which corresponds to about 0.6 % of a monolayer of Pt{111}. This value is in the lower region of previously presented values [45] which can, in part, be explained by the method used to determine the ECSA of Pt. In this case it was done by integrating the Pt-H_{UPD} region from CV. There are uncertainties in this method arising from the somewhat arbitrary integration limits, the corresponding H saturation coverage and the adsorption charge per surface area [167]. In the method used in **paper IV**, a H coverage of 0.77 was assumed at the onset of HER and 210 μC cm⁻² was used for a H_{UPD} monolayer [36]. These assumptions yield slightly higher ECSA than some of those employed by others. Another reason for the measured lower corrosion rate can be that the evaporated Pt films had a rather rough surface. The roughness factor

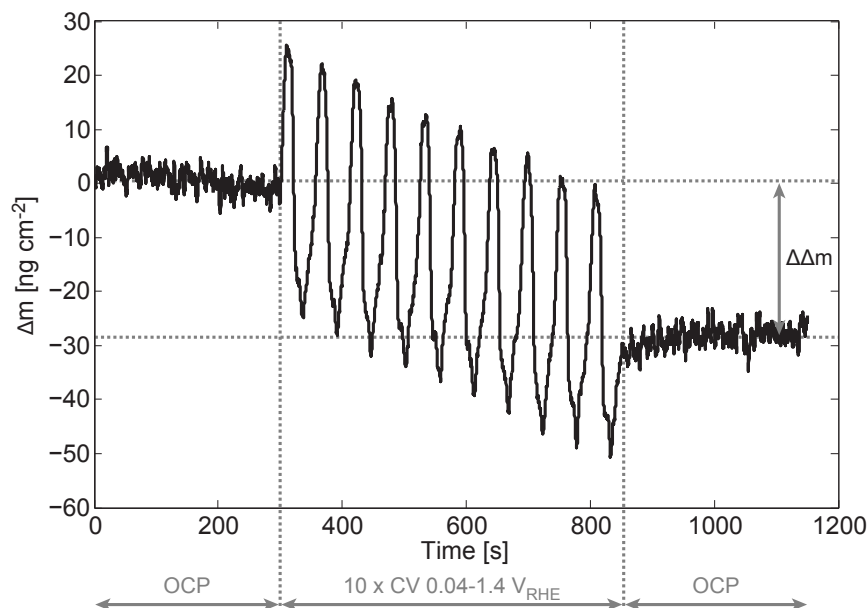


Figure 5.6: Cyclic corrosion experiment on a fully covering Pt film measured in an EQCM-D setup. During the first 5 min, the system was at OCP, thereafter 10 cycles up to 1.4 V at 50 mV s^{-1} was performed before the system was returned to OCP.

(ECSA divided by geometric area) was 3.3 and it is likely that a rough film (in this context, a nanoscale roughness, or even a semi-porous structure) will lose less mass (per ECSA) than a flat, due to a larger probability of re-deposition. An indication of this was seen for evaporated films of different thicknesses, which also differed in roughness. The mass loss rate for fully covering Pt films was found not to change with temperature in the range between 22–70 °C. This implies that the process for mass loss is governed by electrochemical processes under these experimental conditions. The exact mechanism for the Pt dissolution was not arrived at in this study, but it was seen that cycling above or under Pt oxidation/oxide reduction did not render significant mass loss, whereas cycling through this potential regime yielded a much higher mass loss. Thus, it is likely that the transition between Pt and Pt oxide is important in the dissolution process.

Pt dissolution was not measured directly during the degradation measurements in fuel cell, but the accelerated aging scheme applied in **paper III** was chosen such that it would cause Pt dissolution. The loss of ECSA and ORR activity observed after the experiments was likely to originate from Pt dissolution. It was seen that Pt deposited on WO_x only lost about 16 % of its ORR current at 0.85 V, while all other samples lost more than 50 %. Although the ECSA of Pt could not be measured for the Pt on WO_x sample due to H– WO_x bronze formation, the results suggest that WO_x might be able to stabilize Pt.

5.3.2 Carbon Corrosion

Carbon corrosion in fuel cell electrodes leads to a loss of electrode area, which changes the transport conditions in the cell and it induces Pt particle sintering and detachment. To investigate the carbon corrosion and, in particular, the effects of having Pt on carbon, films of evaporated carbon, with and without a non-continuous Pt film on top, was deposited on quartz crystals. These model electrodes were measured in the same EQCM-D setup used for the Pt dissolution experiments mentioned above and presented in **paper IV**. During cyclic degradation, the mass change for the non-catalyzed carbon showed no temperature dependence in the range between 22–70 °C and the absolute mass change was close to the detection limit. Although uncertain, a small mass loss was observed and corresponded to about 0.7 % of a monolayer of graphite oxidized per cycle, assuming a perfectly flat surface. As the surface had a small roughness, this corrosion rate is probably a slight overestimation. Nonetheless, it is on the same order as previously presented values for uncatalyzed carbon black [107].

For the samples with Pt on top of the carbon, a clear temperature dependence was seen for the mass loss. The most likely explanation for this behavior is that Pt catalyzed carbon corrosion was occurring and that this process is thermally activated. To examine the Pt catalyzed carbon corrosion, the mass loss from Pt dissolution and carbon corrosion needed to be decoupled. It was assumed that the Pt dissolution was similar to that derived for the fully covering Pt samples. When the expected Pt dissolution was subtracted, it was seen that the mass loss of the non-fully covering Pt on carbon was just slightly higher than zero, at room temperature. There are two possible reasons for this effect, either that the non-fully covering Pt film had a higher Pt dissolution rate (perhaps associated with a lower roughness, as discussed above) or that Pt catalyzed carbon corrosion was occurring also at room temperature. As there was no means to discriminate between the two effects in this study, the subsequent analysis of the temperature dependence was carried out assuming the latter possibility. After correcting for the expected Pt dissolution, the temperature dependent mass loss could be fitted to a first order rate expression with an activation energy (E_a) of 0.33 eV. Previously presented values of E_a for catalyzed carbon blacks have been around or above 0.4 eV [107]. This small discrepancy may originate from differences in the degradation scheme used, the microstructure of the carbon, as well as the electrode history [107]. As shown in figure 4.4, the crystallite sizes of the evaporated carbon films were probably smaller than that of carbon blacks. Since carbon corrosion has been suggested to proceed via the edges of carbon crystallites [168], the difference in crystallite size may be responsible for the somewhat lower activation energy in this work.

Summary of Appended Papers

Paper I

Thin-films of Pt and Pt supported on metal oxides of Ti, Zr, and Ta deposited on Nafion membranes were evaluated in a single cell fuel cell. Electrochemical characterization of the films was performed by means of ORR activity, high frequency impedance, and CV at 80 °C and full humidification. The chemical state of the metal oxides was analyzed with XPS prior to the electrochemical measurements and the results suggested that native oxides of TiO_2 , ZrO_2 and Ta_2O_5 had formed during exposure to air. TEM analysis of the film morphology showed that all metal oxide supported Pt samples had similar structures. However, their behaviors in the fuel cell were significantly different. An increased cell resistivity of at least one order of magnitude was seen with 1.5 nm ZrO_2 and Ta_2O_5 as spacer layers whereas TiO_2 spacers of up to 18 nm showed the same resistivity as the system without spacer layer. Thick Pt films (20 nm) also rendered a high resistivity although they had a morphology similar to that of the 18 nm TiO_2 films. The results indicated that the proton conduction through fully covering TiO_2 films in the PEM fuel cell is considerable. The Grotthuss mechanism of proton transport in hydrated nanopores in TiO_2 appears as the most likely origin, but was not examined closer. An increased ORR activity was observed for Pt supported on TiO_2 and was attributed to an increased ECSA of Pt. The origin of the increase in surface area is likely caused by a better dispersion when Pt is deposited on TiO_2 as compared to Nafion. The results presented in this paper open up for a number of usages of TiO_2 as electrolyte material in PEMFC.

Paper II

Nanostructured electrodes consisting of Pt nanodisks with different Pt coverage were prepared on GC substrates by CL. The ORR was studied in a double compartment thin-layer flow-cell where H_2O_2 produced from the samples could be detected in the second compartment. This setup in combination with the nanostructured samples allowed quantification of the H_2O_2 yield as a function of Pt surface coverage. The results showed a significantly higher H_2O_2 yield on the samples with low Pt

coverage and prove that the ORR proceeds, at least partly via a serial pathway and that the formed H_2O_2 can desorb from the Pt surface. On the low loaded samples, a H_2O_2 yield of between 5 and 10 % was seen in the potential window of 0.6–0.2 V and below 0.2 V it reached up to 20 %. At the low potentials, the carbon support was also producing H_2O_2 , but at a relatively low amount. On the high loaded samples, the chance for the desorbed H_2O_2 to re-adsorb and be further reduced to H_2O is higher and, consequently, the H_2O_2 yield was lower on these electrodes. The results presented are of both fundamental and practical importance, as they offer new insights into the reaction mechanism of the ORR and show that the use of low loaded electrodes may result in an increased H_2O_2 formation, which in turn can cause degradation in the fuel cell.

Paper III

Model electrodes of metal oxide supported Pt deposited on GDL was electrochemically evaluated in a single cell fuel cell to investigate Pt–support interactions. The metal oxides were produced by evaporation of Ti, Zr, W, Ta, and Sn which oxidized in air and XPS analysis revealed that the materials likely formed TiO_2 , ZrO_2 , WO_3 , Ta_2O_5 , and either SnO or SnO_2 , respectively. Since the thickness of the metal oxide films ranged from 3–20 nm it could not be established whether the films had the same oxidation state through the whole thickness and thus they were termed MeO_x . For samples with 3 nm Pt on 3 nm MeO_x , an increased ECSA was observed for Pt on SnO_x and a poor stability was found for Pt on TaO_x . Consequently, the initial ORR activity was the highest for Pt on SnO_x . After accelerated degradation consisting of 1000 cycles between 0.6–1.2 V, the Pt on SnO_x sample had lost more ECSA and showed a lower ORR activity than the other samples, indicating an increased degradation rate. Pt on WO_x , on the other hand, showed the highest ORR activity after the degradation experiments, indicating a reduced degradation compared to the other samples. This suggests that it may be beneficial to incorporate WO_x in fuel cell electrodes. For TiO_x and WO_x it was seen that increasing the metal oxide thickness to 10 nm and above, resulted in an increased ECSA of Pt, i.e. a higher Pt utilization.

Paper IV

A combined electrochemical and quartz crystal microbalance setup (EQCM-D) was used in a flow-through half-cell to measure mass change caused by Pt dissolution and carbon corrosion. The samples consisted of flat model electrodes with a base film of evaporated carbon, which had a structure that resembled that of carbon black. These films were used as reference samples for uncatalyzed carbon. By evaporating a fully covering Pt film on top of the carbon, reference samples for Pt was obtained. To model a Pt/C electrode, non-fully covering Pt films was deposited on the carbon. Corrosion experiments were performed on all samples

by cycling the potential between 0.02–1.4 V at temperatures between 22 and 70 °C. For the C-only and Pt-only samples, the mass loss showed no temperature dependence and the measured corrosion rates agreed with previously presented values. A Pt dissolution rate of $2.8 \text{ nm cm}^{-2} \text{ cycle}^{-1}$ was determined for the fully covering Pt films, corresponding to a loss of about 0.6 % of a monolayer of Pt{111} per cycle. A temperature dependant corrosion process was observed for the non-fully covering Pt on carbon samples which was attributed to Pt catalyzed carbon corrosion. This process showed an Arrhenius type behavior with an apparent activation energy of 0.33 eV. All samples with exposed carbon showed small, but reproducible variations in dissipation during the potential cycles. The origin of this effect was not determined but it may be connected to oxygenated surface groups on carbon, interacting with the surrounding electrolyte.

Paper V

Films with nominal thicknesses of 1.5, 3, and 6 nm Pt deposited on GDL was used as electrodes to study the HOR in a single cell fuel cell. The cell was operated with pure H₂ humidified to 90 % relative humidity over both the sample and the CE, which was a commercial, high loaded Pt electrode. The very low Pt loading on the samples and the absence of ionomer in the GDL should, theoretically, reduce the risk of mass transport limitations affecting the measurements. The three different thicknesses of Pt rendered different ECSA of Pt in the fuel cell and in liquid electrolyte, which agreed well with the structure observed in SEM analysis, although in the fuel cell the Pt utilization was lower. The fact that the HOR currents were more or less identical for the three samples when normalized to ECSA, supports the assumption that mass transport was not affecting the measurements. The results showed that the HOR reached a limiting current of about 1.6 A cm^{-2} at around 0.07 V. This value is significantly higher than what has been presented previously. As it is believed that the limiting current is not a result of mass transport limitations, it must mean that a chemical step (i.e. not electrochemical) is rate-limiting when the limiting current is reached. The only chemical step in the proposed mechanism for HOR is the dissociative adsorption of H₂, i.e. the Tafel step. The exchange current density was derived from iR corrected HOR plots close to the equilibrium potential using an expression derived from the suggested Tafel–Volmer mechanism assuming negligible concentration polarization. An exchange current density of about 770 mA cm^{-2} was found. This value is higher, but on the same order as previously presented data. The presented results are important as they show that the HOR is presumable faster than what has been known, which mean that it should be possible to create anode electrodes with a lower Pt loading without imposing too high voltage losses.

Paper VI

Several modifications to the HCL fabrication scheme were developed and the results expand the application range of the technique. It was shown that electrodeposition could be used as the method to produce the nanostructures rather than evaporation. The advantages of this include an increased material utilization, simpler and cheaper equipment requirements, and the ability to create nanoparticles with a higher aspect ratio. Electrodeposited nanodisks of Pt were prepared on both Au and evaporated carbon supports and electrochemical evaluation showed no sign of impurities and a high electrochemical stability of the nanostructures upon voltage cycling was established. A routine to create nanoparticles with a much smaller size than the colloidal spheres used to define the mask was also presented. This enables fabrication of samples with very low nanostructure coverage while preserving the high order induced by the electrostatic repulsion between the colloidal spheres. Furthermore, it was shown that by heat treating (annealing) arrays of polycrystalline Pt nanoparticles, they could be transformed into arrays of almost perfect single crystals. This enables mechanistic studies where crystal facets and edges can be studied and/or accounted for.

Paper VII

Arrays of Pt–Ru nanodisk pairs with controlled separation between the Pt and Ru was fabricated on GC substrates using HCL. The distance between the disks within the pairs was varied from overlapping by about 25 nm, to fully separated pairs with 25 or 50 nm separations. By including reference samples of the single materials with a similar structure, it was possible to identify processes related to interactions between Pt–Ru. From CO stripping experiments it was observed that all three Pt/Ru samples showed an increased activity for CO oxidation in the potential range of 0.5–0.7 V, where Pt nanodisks and Ru nanodisks showed a low activity. The fact that an interaction effect was seen even when Pt and Ru phases were separated by 50 nm was surprising but might be a result of Ru dissolution, resulting from cycling to higher potentials, followed by Ru deposition on the Pt disks. Although the electrochemical results are somewhat difficult to interpret in this study, this type of model system shows great promise for further studies. The possibility to precisely control the separation of two kinds of catalytically active materials, at the nanoscale, will make it possible to study proximity and transport effects between materials in bi-metallic as well as multi-metallic systems.

Paper VIII

Thin-films of WO_x , with and without a top layer of 3 nm Pt deposited on GDL were used as model electrodes elucidate the role of WO_x in fuel cell electrodes based on several reactions. WO_x thicknesses between 10 and 40 nm were used and the electrodes were evaluated both as anode and cathode electrodes by analyzing

HOR, CO stripping, ORR, as well as CV. The samples were measured in liquid electrolyte and in fuel cell with and without Nafion sprayed on top of the Pt/WO_x layer. In particular, the ability of WO_x to form hydrogen tungsten bronzes in fuel cell environment was analyzed. The results showed that the kinetics of the bronze formation was influenced by the presence of Pt. Both the hydrogen intercalation and deintercalation was shifted to lower potentials when Pt was deposited on the WO_x, but the total amount of bronzes formed was not dependent on Pt being present. No beneficial effects of WO_x were seen for the ORR. However, indications that WO_x could increase the Pt utilization and reduce the CO oxidation potential was observed, which could indicate that the electrodes are more CO tolerant. Several interesting effects were seen comparing electrodes with and without Nafion sprayed on top, as well as comparing results from liquid electrolyte and fuel cell.

Conclusions and Outlook

Nanostructured model electrodes are valuable tools for studies of fuel cell reactions. Different aspects of PEMFC reactions can be addressed by designing different types of model systems. The ability to work on different complexity; from well-characterized to less defined but more realistic, gives additional synergies. The obtained results are of fundamental interest and add important understanding to the investigated processes. Some of the results can be applied more or less directly to the development of improved fuel cells.

Thin-film electrodes deposited on Nafion or GDL can be evaluated in single cell fuel cells under conditions that are similar to the real application. Compared to conventional fuel cell electrodes, these models are well-defined and have the ability to include multiple materials with minimal structural changes. Another benefit is the fast fabrication, in general the time requirement for producing up to 50 cm² of one type of model electrode is less than two hours, where around 15–20 min is active work (the rest is pump time of the employed vacuum system). The low loadings and high mass transport characteristics of thin films deposited on GDL have provided new insights to the HOR reaction and allowed, for the first time, determination of kinetic parameters in fuel cell environment. This method shows great promise and continued work can include determination of activation energies by varying the operational temperature.

It has been demonstrated that the EQCM-D technique can be used to measure electrochemically induced mass changes and, in particular, it was used to address corrosion of fuel cell electrodes. An interesting follow-up study would be to use lithographically produced Pt particles on carbon together with microscopy characterization, to answer fundamental questions related to the Pt catalyzed carbon corrosion. Questions that could be targeted are whether it is only carbon in direct contact with Pt that is catalytically oxidized, if activated oxygen species can spill over and move on the carbon, or if (partially oxidized) carbon can migrate to Pt.

Model electrodes prepared by CL and especially HCL on flat supports are very well-defined and are able to provide new insights to several fuel cell related reactions. These electrodes allow studies of the special diffusion situation that occur around isolated catalyst nanoparticles (hemispherical diffusion) and with additional analysis techniques, such as MS, these systems can shine light on intrinsic kinetics and mechanisms. An obvious continuation or add-on to this methodology would be

to include mathematical modeling in order to gain further understanding of the fundamental, kinetic, transport and other processes. Furthermore, the promising results on nanodisk pair arrays indicates that these model electrodes can be of use to examine many bi- or multi-metallic systems.

The conclusions drawn for the investigated electrochemical reactions were enabled by the use of nanofabricated model electrodes and the range of characterization techniques employed. For future refined experiments, the fabrication procedures can be modified to achieve new structures that can be used to answer additional questions. One example is the annealing of arrays of polycrystalline nanodisks to create single crystal particles with certain crystal facets exposed. Such electrodes have all the advantages of the CL and HCL produced samples, but with additional information about crystal facets and edges. This opens up a number of possibilities within electrochemistry and can be used to further bridge the gap between extended single crystal surfaces and polycrystalline nanoparticles. Thus, optimization and development of new model systems is another interesting path that pledge further success for understanding of electrochemical processes.

With respect to the electrochemical evaluation, the approach of combining multiple real-time measurement techniques is especially valuable. This includes combining electrochemistry with QCM, MS, IR, and STM to gain synergies and probe features that are not accessible with either of the techniques alone. This combinatory approach was applied in a few of the studies in this work and follows a current trend in many areas of science. This trend will certainly continue and influence the forthcoming research on fuel cells.

Although this thesis has covered PEMFC and issues related to this application, many of the methods can be applied to other fields. Most obvious is perhaps conventional heterogeneous catalysis, batteries, and solar cells.

It has been an exciting journey to work with and follow the fuel cell development during the course of this thesis. In the beginning, the visions were grand but little of what had been shown could convincingly portray fuel cells as an important technology in global energy systems. To the general public, fuel cells were mainly associated with science fiction and few people even knew what types of applications were possible. Although the situation to some extent is similar today, there is a broader and more realistic awareness. The fuel cell community has gone from presenting what was believed could be achieved, to demonstrating that fuel cells are compatible or even superior to competing technology in some areas. During this time, fuel cells have gone from vision and promise to commercially available products. I have no doubt that this trend will continue and that we will see fuel cells out rival or compliment traditional technology in many fields and I hope to be able to contribute to and follow this development also in the future.

Acknowledgements

This work was performed within the EU integrated project Autobrane, the Swedish foundation for strategic environmental research (MISTRA) fuel cell program, and the Competence Centre for Catalysis (KCK). The Competence Centre for Catalysis is hosted by Chalmers University of Technology and financially supported by the Swedish Energy Agency and the member companies: AB Volvo, Volvo Car Corporation, Scania CV AB, Saab Automobile Powertrain AB, Haldor Topsøe A/S, and The Swedish Space Corporation. Additional support from the EU coordination action CARISMA is also acknowledged.

In addition, I want to thank Professors Bengt Kasemo and Magnus Skoglundh for giving me the opportunity to perform this work at Chemical Physics and KCK. Bengt deserves additional gratitude for inspiring and motivating discussions throughout this process.

Assoc. Prof. Henrik Grönbeck, my main supervisor deserves special credit for always finding time and capturing the essence of problems. Your experience and enthusiasm is a great source of motivation.

Dr. Per Hanarp, my assistant supervisor during the beginning of this work must be noticed for teaching me most of the practical tips and tricks in nanofabrication.

The practical help from Dr. Lars Ilver (XPS), Dr. Anders Kvist (SEM), and Dr. Stefan Gustafsson (TEM) has been of great value.

A key element in this work has been the fruitful collaborations, without which this work would not have been possible. Thank you all for patiently awaiting samples, thorough analysis and interesting discussions.

From the KTH-group, Prof. Göran Lindbergh, Assoc. Prof. Carina Lagergren, Dr. Henrik Ekström and especially (soon to be Dr.) Maria Wesselmark, I have really appreciated working with you all and the insights I have gained in the field of electrochemistry.

From the University of Ulm, Prof. Jürgen Behm and (soon to be Dr.) Yvonne Seidel, your devotion and vast knowledge is truly a source of inspiration.

My friends and colleagues at Chemical Physics and KCK are all warmly acknowledged for creating a great atmosphere to work in. Andreas Lundström and Dr Hans Fredriksson for all the intriguing debates and practical help, deserves extra credit.

My friends and family, especially Mamma, Pappa, Karin, and foremost, Moa, thank you for your support and encouragement. It means the world to me.

Bibliography

- [1] *Key World Energy Statistics 2009*. International Energy Agency, (2009).
- [2] Pike, R. and Earis, P. *Energy and Environmental Science* **3**(2), 173 (2010).
- [3] Hegerl, G. C., Zwiers, F. W., Braconnot, P., Gillett, N. P., Luo, Y., Marengo Orsini, J. A., Nicholls, N., Penner, J. E., and Stott, P. A. In *Climate Change 2007: The Physical Science Basis. Contribution of Working Group I to the Fourth Assessment Report of the Intergovernmental Panel on Climate Change*, Solomon, S., Qin, D., Manning, M., Chen, Z., Marquis, M., Averyt, K., Tignor, M., and Miller, H., editors. Cambridge University Press, Cambridge (2007).
- [4] Ferguson, C. R. and Kirkpatrick, A. T. *Internal Combustion Engines*. John Wiley & Sons, New York, 2nd edition, (2001).
- [5] Mock, P. and Schmid, S. A. *Journal of Power Sources* **190**(1), 133–140 (2009).
- [6] *Hydrogen and Fuel Cell Activities, Progress, and Plans: Report to Congress*. U.S. Department of Energy, (2009).
- [7] Yang, C. J. *Energy Policy* **37**(5), 1805–1808 (2009).
- [8] Somorjai, G. A., York, R. L., Butcher, D., and Park, J. Y. *Physical Chemistry Chemical Physics* **9**(27), 3500–3513 (2007).
- [9] Chen, E. In *Fuel Cell Technology Handbook*, Hoogers, G., editor. CRC Press, Boca Raton (2003).
- [10] Grove, W. R. *London and Edinburgh Philosophical Magazine and Journal of Science* **14**, 127–130 (1839).
- [11] Grove, W. R. *London, Edinburgh and Dublin Philosophical Magazine and Journal of Science* **21**, 417–420 (1842).
- [12] Barbir, F. *PEM Fuel Cells: Theory and Practice*. Elsevier Academic Press, London, (2005).
- [13] Larminie, J. and Dicks, A. *Fuel Cell Systems Explained*. John Wiley & Sons, West Sussex, 2 edition, (2006).
- [14] O’Hayre, R. P., Cha, S.-W., Colella, W., and Prinz, F. B. *Fuel cell fundamentals*. John Wiley & Sons, New York, (2006).
- [15] Hoogers, G. In *Fuel Cell Technology Handbook*, Hoogers, G., editor. CRC Press, Boca Raton (2003).
- [16] Steele, B. C. H. *Journal of Materials Science* **36**(5), 1053–1068 (2001).
- [17] Sammes, N., Bove, R., and Stahl, K. *Current Opinion in Solid State and Materials Science* **8**(5), 372–378 (2004).

- [18] McLean, G. F., Niet, T., Prince-Richard, S., and Djilali, N. *International Journal of Hydrogen Energy* **27**(5), 507–526 (2002).
- [19] Bullen, R. A., Arnot, T. C., Lakeman, J. B., and Walsh, F. C. *Biosensors & Bioelectronics* **21**(11), 2015–2045 (2006).
- [20] Smitha, B., Sridhar, S., and Khan, A. A. *Journal of Membrane Science* **259**(1-2), 10–26 (2005).
- [21] Schmidt-Rohr, K. and Chen, Q. *Nature Materials* **7**(1), 75–83 (2008).
- [22] Kreuer, K. D. *Journal of Membrane Science* **185**(1), 29–39 (2001).
- [23] Jannasch, P. *Current Opinion in Colloid & Interface Science* **8**(1), 96–102 (2003).
- [24] Roziere, J. and Jones, D. J. *Annual Review of Materials Research* **33**, 503–555 (2003).
- [25] Jones, D. J. and Rozière, J. In *Advances in Polymer Science*, volume 215, 219–264. Springer, Berlin (2008).
- [26] Litster, S. and McLean, G. *Journal of Power Sources* **130**(1-2), 61–76 (2004).
- [27] Dicks, A. L. *Journal of Power Sources* **156**(2), 128–141 (2006).
- [28] Gasteiger, H. A., Kocha, S. S., Sompalli, B., and Wagner, F. T. *Applied Catalysis B-Environmental* **56**(1-2), 9–35 (2005).
- [29] Hermann, A., Chaudhuri, T., and Spagnol, P. *International Journal of Hydrogen Energy* **30**(12), 1297–1302 (2005).
- [30] Li, X. G. and Sabir, M. *International Journal of Hydrogen Energy* **30**(4), 359–371 (2005).
- [31] Tawfik, H., Hung, Y., and Mahajan, D. *Journal of Power Sources* **163**(2), 755–767 (2007).
- [32] Tan, J. Z., Chao, Y. J., Van Zee, J. W., and Lee, W. K. *Materials Science and Engineering a-Structural Materials Properties Microstructure and Processing* **445**, 669–675 (2007).
- [33] Santos, E. and Schmickler, W. In *Fuel Cell Catalysis: A Surface Science Approach*, Koper, M. T. M., editor, 31–55. John Wiley & Sons, New Jersey (2009).
- [34] Pletcher, D. *A first course in electrode processes*. The Electrochemical Consultancy, Hants, (1991).
- [35] Hamann, C. H., Hamnett, A., and Vielstich, W. *Electrochemistry*. Wiley-VCH, Weinheim, (2004).
- [36] Biegler, T., Rand, D. A. J., and Woods, R. *Journal of Electroanalytical Chemistry* **29**(2), 269–277 (1971).
- [37] Tremiliosifilho, G., Jerkiewicz, G., and Conway, B. E. *Langmuir* **8**(2), 658–667 (1992).
- [38] Markovic, N. M. and Ross, P. N. *Surface Science Reports* **45**(4-6), 121–229 (2002).
- [39] Markovic, N. M., Adzic, R. R., Cahan, B. D., and Yeager, E. B. *Journal of Electroanalytical Chemistry* **377**(1-2), 249–259 (1994).

- [40] Markovic, N. M., Grgur, B. N., and Ross, P. N. *Journal of Physical Chemistry B* **101**(27), 5405–5413 (1997).
- [41] Chorkendorff, I. and Niemantsverdriet, J. W. *Concepts of Modern Catalysis and Kinetics*. Wiley-VCH, Weinheim, (2003).
- [42] Hammer, B. and Nørskov, J. K. *Surface Science* **343**(3), 211–220 (1995).
- [43] Conner, W. C. and Falconer, J. L. *Chemical Reviews* **95**(3), 759–788 (1995).
- [44] Cahan, B. D. and Wainright, J. S. *Journal of the Electrochemical Society* **140**(12), L185–L186 (1993).
- [45] Borup, R., Meyers, J., Pivovar, B., Kim, Y. S., Mukundan, R., Garland, N., Myers, D., Wilson, M., Garzon, F., Wood, D., Zelenay, P., More, K., Stroh, K., Zawodzinski, T., Boncella, J., McGrath, J. E., Inaba, M., Miyatake, K., Hori, M., Ota, K., Ogumi, Z., Miyata, S., Nishikata, A., Siroma, Z., Uchimoto, Y., Yasuda, K., Kimijima, K.-i., and Iwashita, N. *Chemical Reviews* **107**(10), 3904–3951 (2007).
- [46] de Bruijn, F. A., Dam, V. A. T., and Janssen, G. J. M. *Fuel Cells* **8**(1), 3–22 (2008).
- [47] Healy, J., Hayden, C., Xie, T., Olson, K., Waldo, R., Brundage, A., Gasteiger, H., and Abbott, J. *Fuel Cells* **5**(2), 302–308 (2005).
- [48] Tang, H. L., Shen, P. K., Jiang, S. P., Fang, W., and Mu, P. *Journal of Power Sources* **170**(1), 85–92 (2007).
- [49] Peron, J., Nedellec, Y., Jones, D. J., and Roziere, J. *Journal of Power Sources* **185**(2), 1209–1217 (2008).
- [50] Lin, G. Y., He, W. S., and Van Nguyen, T. *Journal of the Electrochemical Society* **151**(12), A1999–A2006 (2004).
- [51] Makkus, R. C., Janssen, A. H. H., de Bruijn, F. A., and Mallant, R. *Journal of Power Sources* **86**(1-2), 274–282 (2000).
- [52] Cleghorn, S. J. C., Mayfield, D. K., Moore, D. A., Moore, J. C., Rusch, G., Sherman, T. W., Sisofo, N. T., and Beuscher, U. *Journal of Power Sources* **158**(1), 446–454 (2006).
- [53] Koper, M. T. M., editor. *Fuel Cell Catalysis: A Surface Science Approach*. Wiley Series on Electrocatalysis and Electrochemistry. John Wiley & Sons, New Jersey, (2009).
- [54] Gottesfeld, S. In *Fuel Cell Catalysis: A Surface Science Approach*, Koper, M. T. M., editor, 1–30. John Wiley & Sons, New Jersey (2009).
- [55] Wroblowa, H. S., Pan, Y. C., and Razumney, G. *Journal of Electroanalytical Chemistry* **69**(2), 195–201 (1976).
- [56] Paulus, U. A., Schmidt, T. J., Gasteiger, H. A., and Behm, R. J. *Journal of Electroanalytical Chemistry* **495**(2), 134–145 (2001).
- [57] Karlberg, G. S., Rossmeisl, J., and Nørskov, J. K. *Physical Chemistry Chemical Physics* **9**(37), 5158–5161 (2007).
- [58] Zhang, J., Lima, F. H. B., Shao, M. H., Sasaki, K., Wang, J. X., Hanson, J., and Adzic, R. R. *Journal of Physical Chemistry B* **109**(48), 22701–22704 (2005).

- [59] Neyerlin, K. C., Gu, W. B., Jorne, J., and Gasteiger, H. A. *Journal of the Electrochemical Society* **153**(10), A1955–A1963 (2006).
- [60] Paulus, U. A., Wokaun, A., Scherer, G. G., Schmidt, T. J., Stamenkovic, V., Radmilovic, V., Markovic, N. M., and Ross, P. N. *Journal of Physical Chemistry B* **106**(16), 4181–4191 (2002).
- [61] Mukerjee, S. and Srinivasan, S. *Journal of Electroanalytical Chemistry* **357**(1-2), 201–224 (1993).
- [62] Mukerjee, S., Srinivasan, S., Soriaga, M. P., and McBreen, J. *Journal of the Electrochemical Society* **142**(5), 1409–1422 (1995).
- [63] Shao, Y. Y., Liu, J., Wang, Y., and Lin, Y. H. *Journal of Materials Chemistry* **19**(1), 46–59 (2009).
- [64] Shim, J., Lee, C. R., Lee, H. K., Lee, J. S., and Cairns, E. J. *Journal of Power Sources* **102**(1-2), 172–177 (2001).
- [65] Bashyam, R. and Zelenay, P. *Nature* **443**(7107), 63–66 (2006).
- [66] Gasteiger, H. A. and Markovic, N. M. *Science* **324**(5923), 48–49 (2009).
- [67] Wang, B. *Journal of Power Sources* **152**(1), 1–15 (2005).
- [68] Vogel, W., Lundquist, J., Ross, P., and Stonehart, P. *Electrochimica Acta* **20**(1), 79–93 (1975).
- [69] Chen, S. L. and Kucernak, A. *Journal of Physical Chemistry B* **108**(37), 13984–13994 (2004).
- [70] Quaino, P. M., Fernandez, J. L., de Chialvo, M. R. G., and Chialvo, A. C. *Journal of Molecular Catalysis a-Chemical* **252**(1-2), 156–162 (2006).
- [71] Wang, J. X., Springer, T. E., and Adzic, R. R. *Journal of the Electrochemical Society* **153**(9), A1732–A1740 (2006).
- [72] Kucernak, A. R. and Toyoda, E. *Electrochemistry Communications* **10**(11), 1728–1731 (2008).
- [73] Neyerlin, K. C., Gu, W. B., Jorne, J., and Gasteiger, H. A. *Journal of the Electrochemical Society* **154**(7), B631–B635 (2007).
- [74] Koper, M. T. M., Lai, S. C. S., and Herrero, E. In *Fuel Cell Catalysis: A Surface Science Approach*, Koper, M. T. M., editor, 159–207. John Wiley & Sons, New Jersey (2009).
- [75] Petrii, O. A. *Journal of Solid State Electrochemistry* **12**(5), 609–642 (2008).
- [76] Diemant, T., Hager, T., Hoster, H. E., Rauscher, H., and Behm, R. J. *Surface Science* **541**(1-3), 137–146 (2003).
- [77] Liu, P., Logadottir, A., and Nørskov, J. K. *Electrochimica Acta* **48**(25-26), 3731–3742 (2003).
- [78] Roth, C., Benker, N., Theissmann, R., Nichols, R. J., and Schiffrin, D. J. *Langmuir* **24**(5), 2191–2199 (2008).
- [79] Gasteiger, H. A., Markovic, N., Ross, P. N., and Cairns, E. J. *Journal of Physical Chemistry* **98**(2), 617–625 (1994).

- [80] Watanabe, M. and Motoo, S. *Journal of Electroanalytical Chemistry* **60**(3), 275–283 (1975).
- [81] Koper, M. T. M. *Surface Science* **548**(1-3), 1–3 (2004).
- [82] He, W. S., Lin, G. Y., and Van Nguyen, T. *Aiche Journal* **49**(12), 3221–3228 (2003).
- [83] Kong, C. S., Kim, D.-Y., Lee, H.-K., Shul, Y.-G., and Lee, T.-H. *Journal of Power Sources* **108**(1-2), 185–191 (2002).
- [84] Lee, K., Zhang, J. J., Wang, H. J., and Wilkinson, D. P. *Journal of Applied Electrochemistry* **36**(5), 507–522 (2006).
- [85] Wang, C., Waje, M., Wang, X., Tang, J. M., Haddon, R. C., and Yan, Y. S. *Nano Letters* **4**(2), 345–348 (2004).
- [86] Debe, M. K., Schmoekel, A. K., Vernstrorn, G. D., and Atanasoski, R. *Journal of Power Sources* **161**(2), 1002–1011 (2006).
- [87] Arico, A. S., Bruce, P., Scrosati, B., Tarascon, J. M., and Van Schalkwijk, W. *Nature Materials* **4**(5), 366–377 (2005).
- [88] Kinoshita, K. *Journal of the Electrochemical Society* **137**(3), 845–848 (1990).
- [89] Büchi, F. N., Inaba, M., and Schmidt, T. J., editors. *Polymer Electrolyte Fuel Cell Durability*. Springer, New York, (2009).
- [90] Mitsushima, S., Kawahara, S., Ota, K. I., and Kamiya, N. *Journal of The Electrochemical Society* **154**(2), B153–B158 (2007).
- [91] Ferreira, P. J., la O, G. J., Shao-Horn, Y., Morgan, D., Makharia, R., Kocho, S., and Gasteiger, H. A. *Journal of The Electrochemical Society* **152**(11), A2256–A2271 (2005).
- [92] Wang, X., Kumar, R., and Myers, D. J. *Electrochemical and Solid State Letters* **9**(5), A225–A227 (2006).
- [93] Yadav, A. P., Nishikata, A., and Tsuru, T. *Electrochimica Acta* **52**(26), 7444–7452 (2007).
- [94] Ofstad, A. B., Thomassen, M. S., de la Fuente, J. L. G., Seland, F., Moller-Holst, S., and Sunde, S. *Journal of The Electrochemical Society* **157**(5), B621–B627 (2010).
- [95] Dam, V. A. T. and de Bruijn, F. A. *Journal of The Electrochemical Society* **154**(5), B494–B499 (2007).
- [96] Lukaszewski, M. and Czerwinski, A. *Journal of Electroanalytical Chemistry* **589**(1), 38–45 (2006).
- [97] Zhang, J., Sasaki, K., Sutter, E., and Adzic, R. R. *Science* **315**(5809), 220–222 (2007).
- [98] Koh, S., Leisch, J., Toney, M. F., and Strasser, P. *Journal of Physical Chemistry C* **111**(9), 3744–3752 (2007).
- [99] Yu, P., Pemberton, M., and Plasse, P. *Journal of Power Sources* **144**(1), 11–20 (2005).
- [100] Colon-Mercado, H. R. and Popov, B. N. *Journal of Power Sources* **155**(2), 253–263 (2006).

- [101] Antolini, E., Salgado, J. R. C., and Gonzalez, E. R. *Journal of Power Sources* **160**(2), 957–968 (2006).
- [102] Kinoshita, K. *Carbon, Electrochemical and Physicochemical Properties*. John Wiley & Sons, New York, (1988).
- [103] Kangasniemi, K. H., Condit, D. A., and Jarvi, T. D. *Journal of The Electrochemical Society* **151**(4), E125–E132 (2004).
- [104] Willsau, J. and Heitbaum, J. *Journal of Electroanalytical Chemistry* **161**(1), 93–101 (1984).
- [105] Colmenares, L. C., Wurth, A., Jusys, Z., and Behm, R. J. *Journal of Power Sources* **190**(1), 14–24 (2009).
- [106] Gallagher, K. G., Wong, D. T., and Fuller, T. F. *Journal of The Electrochemical Society* **155**(5), B488–B493 (2008).
- [107] Maass, S., Finsterwalder, F., Frank, G., Hartmann, R., and Merten, C. *Journal of Power Sources* **176**(2), 444–451 (2008).
- [108] Roen, L. M., Paik, C. H., and Jarvic, T. D. *Electrochemical and Solid State Letters* **7**(1), A19–A22 (2004).
- [109] Chaparro, A. M., Mueller, N., Atienza, C., and Daza, L. *Journal of Electroanalytical Chemistry* **591**(1), 69–73 (2006).
- [110] Ball, S. C., Hudson, S. L., Thompsett, D., and Theobald, B. *Journal of Power Sources* **171**(1), 18–25 (2007).
- [111] Garsany, Y., Baturina, O. A., and Swider-Lyons, K. E. *Journal of the Electrochemical Society* **154**(7), B670–B675 (2007).
- [112] Roduner, E. *Chemical Society Reviews* **35**(7), 583–592 (2006).
- [113] Geissler, M. and Xia, Y. N. *Advanced Materials* **16**(15), 1249–1269 (2004).
- [114] Deckman, H. W. and Dunsmuir, J. H. *Applied Physics Letters* **41**(4), 377–379 (1982).
- [115] Hulteen, J. C., Treichel, D. A., Smith, M. T., Duval, M. L., Jensen, T. R., and Van Duyne, R. P. *Journal of Physical Chemistry B* **103**(19), 3854–3863 (1999).
- [116] Yang, S. M., Jang, S. G., Choi, D. G., Kim, S., and Yu, H. K. *Small* **2**(4), 458–475 (2006).
- [117] Fredriksson, H., Alaverdyan, Y., Dmitriev, A., Langhammer, C., Sutherland, D. S., Zäch, M., and Kasemo, B. *Advanced Materials* **19**(23), 4297–4302 (2007).
- [118] Hanarp, P., Sutherland, D. S., Gold, J., and Kasemo, B. *Colloids and Surfaces A* **214**(1-3), 23–36 (2003).
- [119] Kosiorek, A., Kandulski, W., Glaczynska, H., and Giersig, M. *Small* **1**(4), 439 (2005).
- [120] Lu, Y., Liu, G. L., Kim, J., Mejla, Y. X., and Lee, L. P. *Nano Letters* **5**(1), 119 (2005).
- [121] Venables, J. A. *Surface Science* **299**(1-3), 798–817 (1994).
- [122] Simonsen, S. B., Chorkendorff, I., Dahl, S., Skoglundh, M., Sehested, J., and Helveg, S. *Journal of the American Chemical Society* **132**(23), 7968–7975 (2010).

- [123] Larsson, E. M., Langhammer, C., Zoric, I., and Kasemo, B. *Science* **326**(5956), 1091–1094 (2009).
- [124] Baltruschat, H. *Journal of the American Society for Mass Spectrometry* **15**(12), 1693–1706 (2004).
- [125] Jusys, Z., Kaiser, J., and Behm, R. J. *Electrochimica Acta* **49**(8), 1297–1305 (2004).
- [126] Billy, E., Maillard, F., Morin, A., Guetaz, L., Emieux, F., Thurier, C., Doppelt, P., Donet, S., and Mailley, S. *Journal of Power Sources* **195**(9), 2737–2746 (2010).
- [127] Gruber, D., Ponath, N., Muller, J., and Lindstaedt, F. *Journal of Power Sources* **150**, 67–72 (2005).
- [128] Cha, S. Y. and Lee, W. M. *Journal of the Electrochemical Society* **146**(11), 4055–4060 (1999).
- [129] O’Hayre, R., Lee, S. J., Cha, S. W., and Prinz, F. B. *Journal of Power Sources* **109**(2), 483–493 (2002).
- [130] Brault, P., Caillard, A., Thomann, A. L., Mathias, J., Charles, C., Boswell, R. W., Escribano, S., Durand, J., and Sauvage, T. *Journal of Physics D-Applied Physics* **37**(24), 3419–3423 (2004).
- [131] Rabat, H. and Brault, P. *Fuel Cells* **8**(2), 81–86 (2008).
- [132] Gustavsson, M., Ekström, H., Hanarp, R., Eurenus, L., Lindbergh, G., Olsson, E., and Kasemo, B. *Journal of Power Sources* **163**(2), 671–678 (2007).
- [133] Ekström, H., Hanarp, P., Gustavsson, M., Fridell, E., Lundblad, A., and Lindbergh, G. *Journal of the Electrochemical Society* **153**(4), A724–A730 (2006).
- [134] Basura, V., Beattie, P., and Holdcroft, S. *Journal of Electroanalytical Chemistry* **458**(1-2), 1–5 (1998).
- [135] Grant, A. W., Hu, Q.-H., and Kasemo, B. *Nanotechnology* **15**, 1175–1181 (2004).
- [136] Moulder, J. F., Stickle, W. F., Sobol, P. E., and Bomben, K. D. *Handbook of X-ray Photoelectron Spectroscopy*. PerkinElmer Corporation, Minneapolis, (1992).
- [137] Marcus, P. and Hinnen, C. *Surface Science* **392**(1-3), 134–142 (1997).
- [138] Schelz, S., Richmond, T., Kania, P., Oelhafen, P., and Guntherodt, H. J. *Surface Science* **359**(1-3), 227–236 (1996).
- [139] Ferrari, A. C. and Robertson, J. *Physical Review B* **61**(20), 14095–14107 (2000).
- [140] Ranade, M. R., Navrotsky, A., Zhang, H. Z., Banfield, J. F., Elder, S. H., Zaban, A., Borse, P. H., Kulkarni, S. K., Doran, G. S., and Whitfield, H. J. *Proceedings of the National Academy of Sciences of the United States of America* **99**, 6476–6481 (2002).
- [141] Diebold, U. *Surface Science Reports* **48**(5-8), 53–229 (2003).
- [142] Seidel, Y. E., Lindström, R. W., Jusys, Z., Gustavsson, M., Hanarp, P., Kasemo, B., Minkow, A., Fecht, H. J., and Behm, R. J. *Journal of the Electrochemical Society* **155**(3), K50–K58 (2008).
- [143] Dubas, S. T. and Schlenoff, J. B. *Macromolecules* **32**(24), 8153–8160 (1999).
- [144] Hanarp, P., Sutherland, D. S., Gold, J., and Kasemo, B. *Journal of Colloid and Interface Science* **241**(1), 26–31 (2001).

- [145] Werdinius, C., Österlund, L., and Kasemo, B. *Langmuir* **19**(2), 458–468 (2003).
- [146] Despic, A. R. and Jovic, V. D. In *Modern Aspects of Electrochemistry*, White, R. E., editor, volume 27, 143–232. Plenum Press, New York (1995).
- [147] Lundquist, J. T. and Stonehart, P. *Electrochimica Acta* **18**(5), 349–354 (1973).
- [148] Markovic, N., Gasteiger, H., and Ross, P. N. *Journal of the Electrochemical Society* **144**(5), 1591–1597 (1997).
- [149] Zhdanov, V. P. and Kasemo, B. *Physical Review Letters* **81**(12), 2482–2485 (1998).
- [150] Wong, K., Johansson, S., and Kasemo, B. *Faraday Discussions* **105**, 237–246 (1996).
- [151] Johannsmann, D. *Physical Chemistry Chemical Physics* **10**(31), 4516–4534 (2008).
- [152] Rodahl, M., Höök, F., Krozer, A., Brzezinski, P., and Kasemo, B. *Review of Scientific Instruments* **66**(7), 3924–3930 (1995).
- [153] Ihonen, J., Jaouen, F., Lindbergh, G., and Sundholm, G. *Electrochimica Acta* **46**(19), 2899–2911 (2001).
- [154] Kinumoto, T., Inaba, M., Nakayama, Y., Ogata, K., Umebayashi, R., Tasaka, A., Iriyama, Y., Abe, T., and Ogumi, Z. *Journal of Power Sources* **158**(2), 1222–1228 (2006).
- [155] Shi, Y., Xiao, J. S., Quan, S. H., Pan, M., and Zhang, L. Y. *International Journal of Hydrogen Energy* **35**(7), 2863–2867 (2010).
- [156] Johansson, M., Lytken, O., and Chorkendorff, I. *Topics in Catalysis* **46**(1-2), 175–187 (2007).
- [157] Davies, J. C., Hayden, B. E., Pegg, D. J., and Rendall, M. E. *Surface Science* **496**(1-2), 110–120 (2002).
- [158] Spendelow, J. S., Babu, P. K., and Wieckowski, A. *Current Opinion in Solid State and Materials Science* **9**(1-2), 37–48 (2005).
- [159] Kaiser, J., Colmenares, L., Jusys, Z., Mörtel, R., Bönnemann, H., Köhl, G., Modrow, H., Hormes, J., and Behm, R. J. *Fuel Cells* **6**(3-4), 190–202 (2006).
- [160] Saha, M. S., Banis, M. N., Zhang, Y., Li, R. Y., Sun, X. L., Cai, M., and Wagner, F. T. *Journal of Power Sources* **192**(2), 330–335 (2009).
- [161] Maillard, F., Peyrelade, E., Soldo-Olivier, Y., Chatenet, M., Chainet, E., and Faure, R. *Electrochimica Acta* **52**(5), 1958–1967 (2007).
- [162] Lunell, S., Stashans, A., Ojamae, L., Lindstrom, H., and Hagfeldt, A. *Journal of the American Chemical Society* **119**(31), 7374–7380 (1997).
- [163] Colomer, M. T. *Journal of the European Ceramic Society* **26**(7), 1231–1236 (2006).
- [164] Tejedor-Tejedor, M. I., Vichi, F. M., and Anderson, M. A. *Journal of Porous Materials* **12**(3), 201–214 (2005).
- [165] Li, Y. M., Hibino, M., Miyayama, M., and Kudo, T. *Solid State Ionics* **134**(3-4), 271–279 (2000).
- [166] Jerkiewicz, G., Vatankhah, G., Lessard, J., Soriaga, M. P., and Park, Y. S. *Electrochimica Acta* **49**(9-10), 1451–1459 (2004).
- [167] Trasatti, S. and Petrii, O. A. *Pure and Applied Chemistry* **63**(5), 711–734 (1991).
- [168] Kamp, C. J. and Andersson, B. *Topics in Catalysis* **52**(13-20), 1951–1956 (2009).